IEEE spectrum

features

World Radio History

World Radio History

Spectral lines

The IEEE Convention. The year 1968 saw a marked change in orientation of the technical program at the March Convention. Instead of contributed papers to deepen and update a man's knowledge of his specialty, it comprised thoughtfully organized groups of invited papers, with the goal of communicating across the fences of specialties. A number of the sessions reflected the mounting awareness of engineers that they now are closely coupled to, and greatly influence, nearly every aspect of the society in which they are embedded. This year's Convention is continuing in the same direction, with added momentum.

One extension of the trend seems to me a highly significant one. When planning a purchase of cigars or beer, or even a stove or refrigerator, and seeking information on which to base a choice, one is not likely to look to the advertising in the periodicals. In electronics, the expectation is different; we want more in advertising than a picture of a sailboat or of a lively girl. And we get it. Through gossip or experience, we have learned to take the advertisements of some companies at face value, and those of others at varying discounts, but there is no question that in electronics, advertising is a useful and very important channel of technical communication. As evidence, one need only note that the Russian translations of PROCEEDINGS OF THE IEEE included all the pages of advertising.

In view of the importance of this way of communicating, and with the hope that calling attention to superiority will induce a rise in the general level, the IEEE is inaugurating a set of Awards for Excellence in Advertising. There will be recognition in each of four categories: product, system, corporate capability, and recruitment. Eligible is any series of at least four ads that has appeared during 1968 in *any* electronics publications. Because the IEEE has income from advertisers, the judges in so far as possible have been empanelled from outside the Institute; only a minority are members, and none holds any office. Increasing the usefulness of advertising may be a novel step for an engineering society to attempt. Now that somebody has thought of it, it seems like a natural thing to do, because any success will benefit us all.

Social historians looking back on our century will certainly take one of the chief advances in its first half to be the unriddling of the structures of atoms, and the consequent development not only of nuclear power, but of the engineering of molecules and crystals, including man-made semiconductors. For the second half, it is likely that they will classify as a major intellectual event our recognition and development of the technology of systems. Generated by the study of military problems, the systems approach seems applicable to other broad areas. One of the sessions at the Convention will survey the probable impact of system technology on education, transportation, communication, health care, and urban development. Another exceptional session will be "Lunar Exploration in the 1970s"; it will be held at the Hayden Planetarium.

We are near the point where the bandwidths of information channels into the home, and out from it, will increase by orders of magnitude. Round numbers for the near future are 1 MHz coming out and 100 MHz going in. At the Highlight Session on the Tuesday evening, a panel of ranking executives will examine how such capability can affect the home life of the citizen who employs it.

The whole Convention, of course, is a program of continuing education for engineers. However, the special tutorial innovations introduced last year are being resumed and expanded. There are early-morning courses in reliability engineering, effective writing and speech, and integrated circuits; registrants receive material to study before the Convention. On the Monday and Tuesday, there will be an early-morning workshop on how to write a technical paper. Your editor fervently hopes that the attendance there will be large. On Thursday and Friday, there will be a short course on computer programming and another on the use of time-shared computers, with stress on conversation with the machine.

For registrants who apply early enough to obtain tickets, there will be tours that show electronics impinging on the life of the city. One will cover the computer as a tool in urban management; others will take in an FAA control tower, an electronic control of traffic lights, and a sewage-treatment plant, as well as medical electronics in human and animal hospitals.

To these plus the exhibits, add a few dozen sessions on engineering *per se,* and it looks like it will be a busy week.

J. J. G. McCue

Multielement self-scanned mosaic sensors

*The development of a practical solid-state image
sensor is expected to introduce a whole new class of devices,
with applications extending considerably beyond those
of present-day camera tubes*

**P. K. Weimer, W. S. Pike, G. Sadasiv, F. V. Shallcross,
L. Meray-Horvath**   RCA Laboratories

**Self-scanned image sensors are making possible
new types of television cameras and imaging de-
vices based entirely upon solid-state components.
Research on integrated image sensors has fol-
lowed two experimental approaches: monolithic
silicon and thin-film photoconductors. This article
reviews the operation of the most common types
of self-scanned sensors, indicating their relative
advantages and disadvantages. Two new develop-
ments are a 256 × 256 element photoconductive
sensor with integrated thin-film scanning decoders
and a novel silicon photodiode sensor that may
permit considerable reduction in element spacings.**

Advances in the fabrication of photosensitive ele-
ments and integrated circuits have led to significant
progress in the development of self-scanned image sen-
sors,[1] which produce a video signal without the help
of an electron beam. Figure 1 shows the principal parts
of a common form of solid-state image sensor. It con-
sists of an array of photosensitive elements, each lo-
cated at the intersection of mutually perpendicular
address strips, which are connected to scan generators
and video coupling circuits. The application of sequen-
tial scan pulses to the address strips permits an image
to be scanned, and a video signal to be produced simi-
lar to that generated by a television camera tube. To
obtain image detail comparable to broadcast television,
however, it is apparent that the array must contain
hundreds of thousands of picture elements. Although
these objectives have not yet been reached, recent
progress indicates that self-scanned arrays must be
considered as an eventual replacement for camera
tubes in some applications. A more immediate and

less demanding use for such sensors is in character-
recognition [2] devices, or in optical readers [3] for com-
puters or as aids for the blind.[4]

Solid-state sensors, though still far behind camera
tubes in performance and cost, offer significant ad-
vantages of interest to potential users. Digital scanning
provides a geometric accuracy of scan and a versatil-
ity of addressing not possible with electron beams.
Moreover, the much greater compactness of a self-
scanned sensor can be important in certain applica-
tions. Finally, the expected reduction in cost and
power consumption possible with solid-state devices
should introduce many new applications that have not
been feasible for existing camera tubes.

Fabrication of experimental image sensors has fol-
lowed two approaches. A major portion of the work
carried out in some half a dozen laboratories [5] has
utilized silicon technologies that are highly refined.
This approach can be justified by the enormous ver-
satility of silicon, which provides, in addition to its
integrated circuits, at least four different types of pho-
tosensitive elements. These include p-n junction pho-
todiodes,[6, 7] phototransistors,[8-10] photoconductors,[11]
and photovoltaic cells. The intrinsic spectral response
of silicon ranges from the visible to the near infrared,
and it can be extended into the far infrared by im-
purity photoconduction. Even more important to the
sensor application is the fact that silicon junctions can
be made with sufficiently high resistance to allow in-
tegration of light [6] by charge storage for periods ex-
ceeding the normal television scanning periods.

In spite of the natural advantages of silicon for
image sensors, the technical requirements for a self-
scanned sensor are sufficiently difficult that no pres-
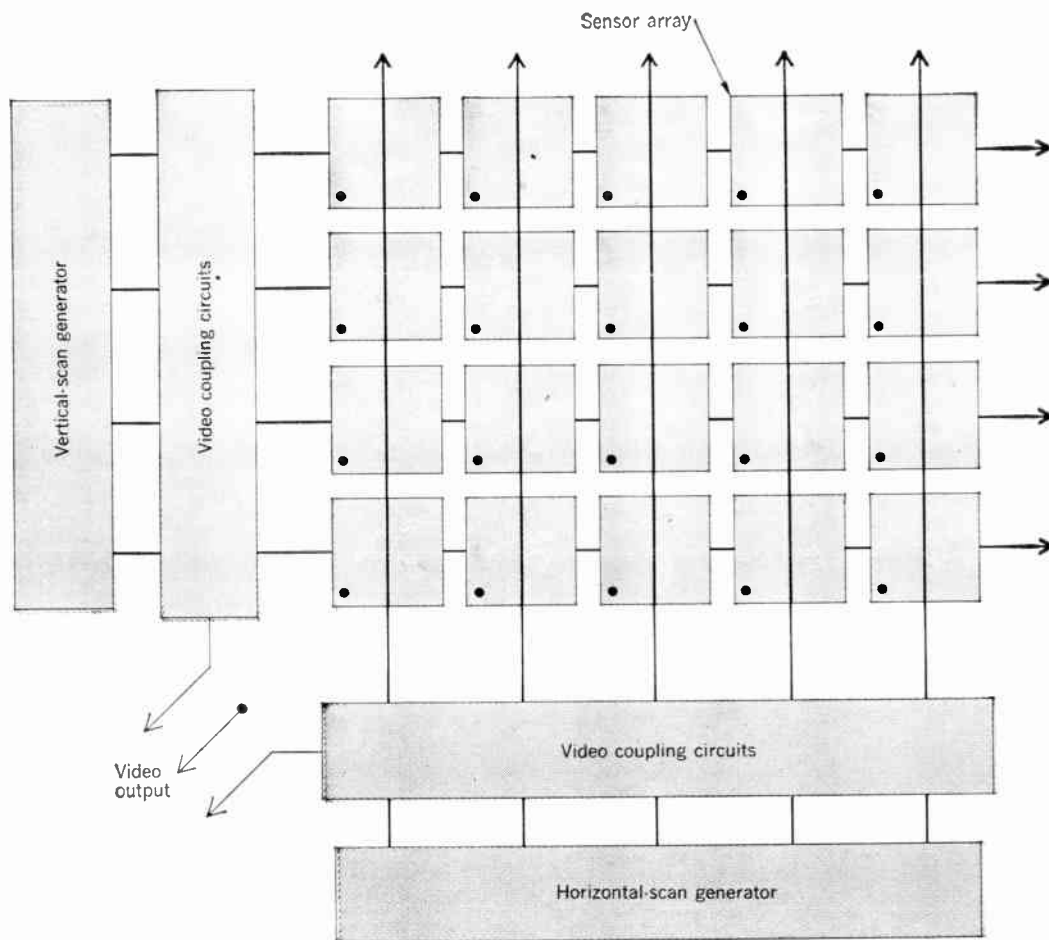
FIGURE 1. Block diagram of self-scanned image sensor, showing three alternative methods of coupling out the video signal.

ently available silicon sensors surpass the competing thin-film approach [1] in total number of picture elements or in degree of integration of the scanning circuits. Even though an integrated sensor (including its scanning circuits) could fit very nicely upon a single silicon slice,[7] the yields of integrated devices now obtained in silicon may make it difficult to produce an integrated self-scanned sensor having hundreds of thousands of elements. The very nature of the imaging process, and the close spacing of elements required, make it hard to use discretionary wiring or redundancy to cover up the defective elements, which produce spurious signals clearly visible in the transmitted picture. Although highly encouraging results have been obtained in the fabrication of silicon photodiode arrays for use in camera tubes,[12] such beam-scanned arrays are much less complex than self-scanned arrays.

The second approach to solid-state sensors that has been explored extensively by the authors makes use of thin-film techniques.[13-16] During the course of this work two experimental cameras incorporating thin-film image sensors have been built. The first uses a 180×180 element photoconductor-diode array[1] scanned by two 180-stage shift registers.[17] The entire circuits, including transistors,[18] diodes, capacitors, resistors and photoconductors were produced by vacuum deposition.[19] The second camera utilizes a 256×256 element thin-film array, which will be described in this article. Photoconductor-diode arrays having up to 360×360 elements spaced upon 25-μm (1-mil) centers have been produced by thin-film techniques.

Principles of digital scanning of sensor arrays

Element design and operation. The operation of an image sensor with solid-state scanning can be com-
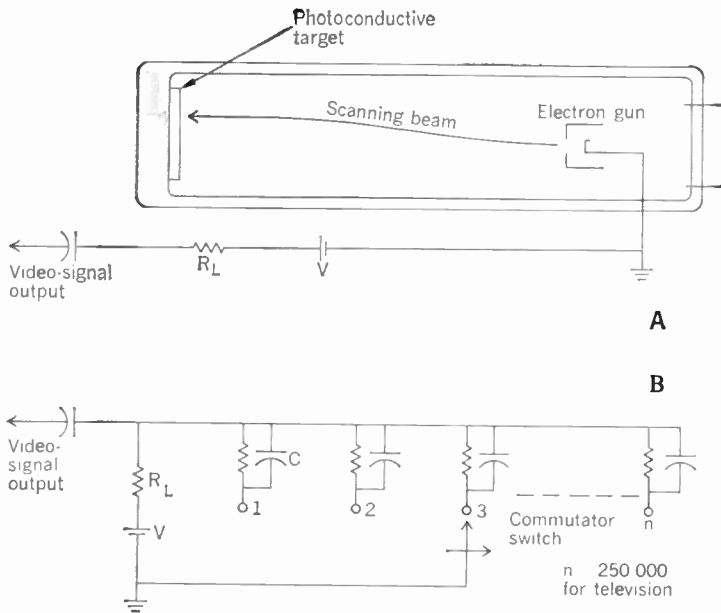
FIGURE 2. Comparison of (A) a typical vidicon photoconductive camera tube with (B) an array of discrete photosensitive elements.
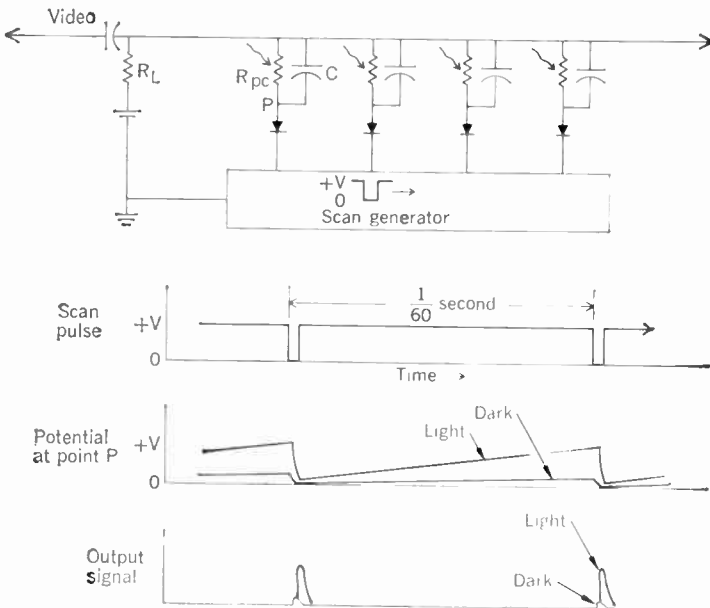
FIGURE 3. Charge-storage operation of a row of photoconductive elements, where the elements are connected in series with diode switches.

FIGURE 4. Sensor-element circuits for three types of self-scanned photodiode arrays. (Two additional photodiode circuits are shown in Fig. 20.)
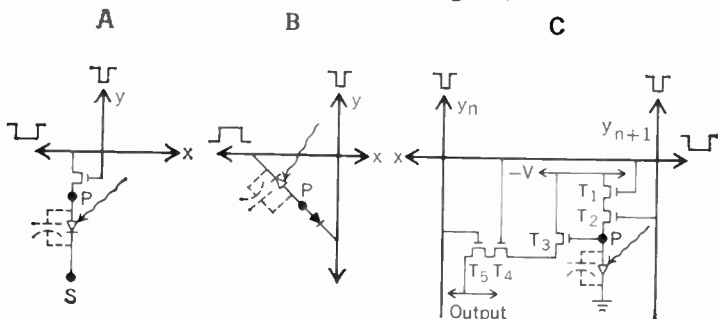
pared to that of a vidicon television camera tube.[20] In such a tube the light from the scene is imaged onto a photoconductive layer, which is scanned with an electron beam. Figure 2 shows how the continuous photoconductive target can be represented as a discrete array of photoconductive elements, which are contacted in sequence by the electron beam. In the solid-state sensor the beam is replaced by a set of sequentially operated switches permanently connected to each photosensitive element. These switches usually consist of a diode or a transistor located at the picture element. They are normally turned off but are activated in sequence by means of pulses that are supplied by the scan generators located at the periphery of the array.

The operation of a single row of photoconductive elements connected to diode switches is shown in Fig. 3. This type of drawing is also helpful in understanding arrays having other combinations of switch and sensor. The operating cycle illustrates the use of charge storage in an elemental capacitor in order to permit integration of light for the entire period between scans.

The capacitance may be that of a discrete capacitor built into each element, or it may arise from the internal shunt capacitance of the photosensitive element. Charge-storage operation is possible only if the RC time constant of the elemental capacitor in series with its switch exceeds the integration period T_i. The dark resistance of the photosensor and the "off" resistance of the switch must therefore be very high. Also, the shunt capacitance across the switch should be small compared with that across the photosensor. As shown in Fig. 3, the effect of the scanning pulse is to reduce the potential quickly at the point P to ground, thereby charging the capacitor C. When light falls on the photoconductor, the capacitor is gradually discharged and point P, which corresponds to the scanned surface of the photoconductor in the vidicon, rises in potential. The charge pulse that flows in the external load resistor R_L during the sampling period T_s is equal to the total charge that had leaked off the capacitor during the light integration period. The effective signal current gain introduced by storage is given by the ratio of T_i to T_s, which, for continuous sequential scanning, is approximately equal to the total number of picture elements in the array.

The foregoing conditions for charge storage have been met in various types of self-scanned arrays. Silicon photodiode arrays having very low dark currents can be fabricated and can provide a sensitivity of very nearly unity quantum yield for visible and near-infrared light. Figure 4 shows the sensor-element circuit for three silicon photodiode sensors employing different types of elemental switches. In each, the photodiode is held in reverse bias at all times and the depletion layer capacitance provides the storage. Photocurrent generated in the depletion layer by light causes this capacitor to be discharged between scans, following an operating cycle similar to the one discussed previously. In each circuit of Fig. 4 the point P joining the sensor to its switch is again analogous to the scanned surface of a camera tube. A photodiode in series with a metal-oxide-semiconductor (MOS) transistor,[9] as shown in Fig. 4(A), would appear to

54

be an attractive combination for a single-line sensor. The photodiode can be combined with the MOS transistor by utilizing the photosensitivity of the depletion layer under the reverse-biased source electrode. However, a charge pumping effect in a p-channel MOS formed on an n-type substrate, which introduces dark current and limits low-light-level performance of the sensor, has been reported.[21] A single MOS transistor in series with a photodiode would not be expected to be useful for charge storage in a *two-dimensional* array because of the bilateral conductivity of the transistor and the photosensitivity of the drain junction. A diode in series with the transistor would be a more useful switch.

Figure 4(B) shows one element of a two-dimensional photodiode array in which a second diode is used as the element switch. The operating cycle of this structure is the same as the one discussed in connection with Fig. 3. The structure is sometimes deprecated in comparison[21] with the phototransistor structure that it resembles. However, it would appear to be potentially superior to the phototransistor in applications in which the relation between light in and signal out needs to be linear.

Figure 4(C) shows a more complex photodiode circuit[7] for a two-dimensional array, in which two MOS transistors, T_1 and T_2, in series serve as the element switch. An additional voltage-sampling circuit at each element provides a sizable current gain in a separate output circuit. The voltage at point P just prior to recharge of the photodiode controls the magnitude of the current pulse through the output circuit $T_3 T_4 T_5$. The switching transistors T_4 and T_5 are connected to column n, which is turned on one element time ahead of the column $n + 1$. An improvement in sensitivity would be obtained at the expense of element spacing and complexity. For a line sensor, where vertical scanning is not required, transistors T_1 and T_4 can be omitted. The resulting circuit, comprising three transistors and a photodiode, has been used in a 72×5 element array[22] in which a video signal is taken simultaneously from each of the five rows.

The phototransistor, by virtue of its current gain, offers the possibility for higher sensitivity than does a simple photodiode. Its reverse-biased collector junction acts as the photosensor and the emitter junction provides the switching function. The collector junction must have a much larger area than the emitter to provide adequate storage capacitance with a small switch capacitance. When this type of element is connected directly across the row and column address strips,[23] as shown in Fig. 5(A), the charge–discharge cycle for the floating base is the same as for point P in the circuits of Figs. 3 and 4(B). To a first approximation, the total charge that flows through the emitter–collector circuit during the sampling pulse is proportional to the accumulated charge on the base multiplied by the current gain of the transistor. This relationship, however, does not hold at all light levels or conditions of operation. Nonlinear transfer characteristics and sluggish transient response may limit low-light performance. Variation in gain from one element to the next introduces an additional uniformity problem that does not exist with photodiode arrays. Although the phototransistor array remains of con-

siderable interest, it is not yet clear whether its gain feature outweighs the additional problems it introduces. Small phototransistor arrays are under consideration for use in a reader for the blind,[21] and larger arrays (up to 200×256) have been built for television purposes.[24] In the last-mentioned arrays the phototransistors[24] were connected as shown in Fig. 5(A), and video signal was derived from the columns.

An alternative method[9] of constructing a phototransistor array is shown in Fig. 5(B). In this case all phototransistors are formed upon a common substrate, with an MOS transistor at each element for addressing purposes. The advantage of this system over the phototransistor array of Fig. 5(A) is not clear. Although it is true that the peripheral video circuits might be somewhat simpler because the video output can be taken from the common substrate, this signal would be expected to contain more spurious switching transients than if the signal were derived from a single row or column. Such transients can seriously limit the performance of large arrays operating at fast switching speeds. The operating cycle for the phototransistor itself is the same as discussed earlier. The elemental switch for charging the base–collector capacitance is still the emitter junction and not the MOS transistor. The same problems of nonlinearity and sluggish response at low signal levels would apply. These prob-
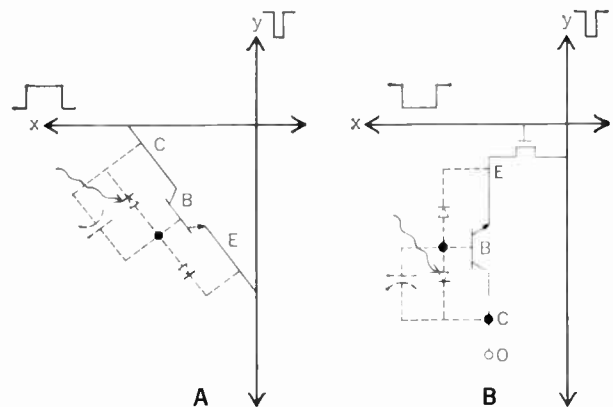
FIGURE 5. Sensor-element circuits for two types of self-scanned phototransistor arrays.

FIGURE 6. Sensor-element circuits for three types of self-scanned photoconductor arrays. Operation in (A) and (B) is by charge storage; in (C) it can be by "excitation storage" if a high-gain photoconductor is used.
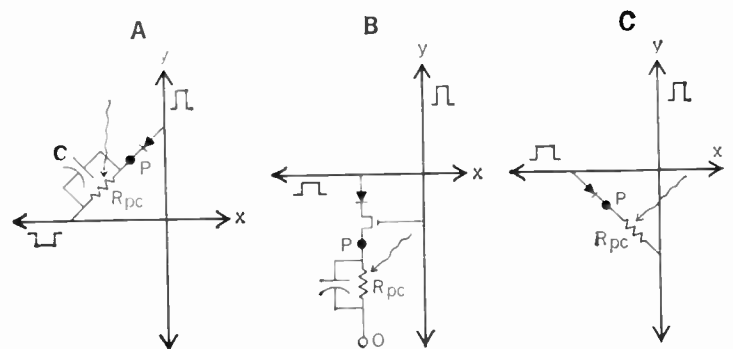
lems and the unwanted switching transients are considerably reduced if very slow scanning speeds can be used. The operation of a 10 000-element array of this type at slow scan rates at very low light levels has been reported.[25]

Figure 6 shows three types of photoconductive arrays. Charge storage in a capacitor shunting the photoconductor is used in 6(A) and 6(B). The operating cycle is the same as that discussed in connection with Fig. 3. In Fig. 6(B) all photoconductive elements are connected to a common lead and to a thin-film transistor switch. The diode in series with the transistor is required in a two-dimensional array to isolate each storage point P for full frame storage.

Figure 6(C) differs from all the preceding elemental circuits in that the capacitor is omitted and no charge storage is provided at each element. In this case, light integration for an appreciable fraction of a television frame time is obtained by use of a high-gain photoconductor.[1] This method of operation has been termed "excitation storage" since, in effect, the light energy is stored in the form of excited carriers whose lifetime ideally approximates the scanning period. Although the effective duty cycle for current flow through each photoconductive element is only N^{-1} times that of an element with full charge storage, where N is the total number of elements, this loss in signal can be compensated by using a photoconductor with an internal gain of N electrons per photon. The effective quantum yield of the sensor thus approaches $N \cdot 1/N = 1$, a value equal to the maximum quantum yield normally expected with full charge storage. In practice the total photoconductive gain obtained in the photoconductive arrays reported to date is approximately 2000 (including losses due to unused area). Since the total

number of elements in the latest 256 × 256 element camera is approximately 65 000, the total output signal with no charge storage would fall short of a full-storage unity-gain sensor by about 30 times. This loss can be more than compensated for by the use of line storage, which gives a signal gain equal to the number of elements in a row. The line storage mode of addressing is discussed in the following section.

An advantage of not using charge storage at each element is the simplification of the structure permitting a higher density of elements. Figure 7 shows a portion of a 360 × 360 array in which each element consists of a photoconductor in series with a diode, with the elements spaced upon 26.5-μm (1.04-mil) centers. The output signal from an array of this kind can be made arbitrarily large by increasing the light intensity since the output signal is not limited by the size of the charge-storage capacitor that can be built into each element. For applications requiring higher sensitivity, line storage in external capacitors provides a very large increase in output signal.

Extraction of the video signal from the sensor array. Three methods of coupling the video output of an image sensor to the input of the camera amplifier are illustrated in Figs. 8, 9, and 10. These circuits assume conventional television scanning from one element to the next along successive horizontal rows. The horizontal-scan generator (connected to the columns) accordingly operates at a much higher clock rate than the vertical-scan generators. Although a photoconductor sensor element is illustrated in each figure, the video coupling circuits are equally applicable for various types of silicon arrays.

In the system shown in Fig. 8, the amplifier is attached to an output terminal that is permanently connected within the array to each element. The arrays illustrated in Figs. 4(C), 5(B), and 6(B) provide such a terminal, connected through a conducting substrate or conducting strips to the point O at each element. Although this method of coupling is feasible for low-

FIGURE 7. Photomicrograph of a portion of a 360 × 360 element photoconductor-diode array having elements spaced on 26.5-μm centers.

26.5 μm
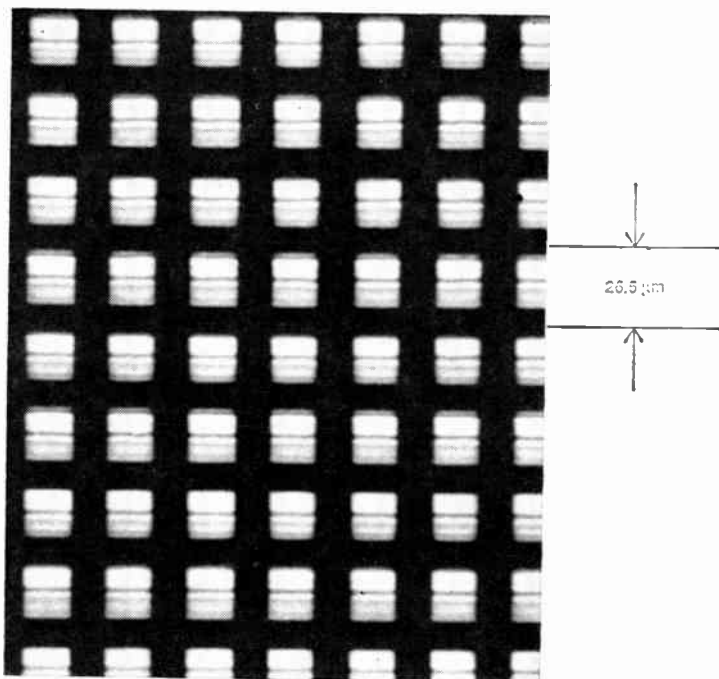
FIGURE 8. Extraction of video signal from a common lead connected to all elements of the sensor.
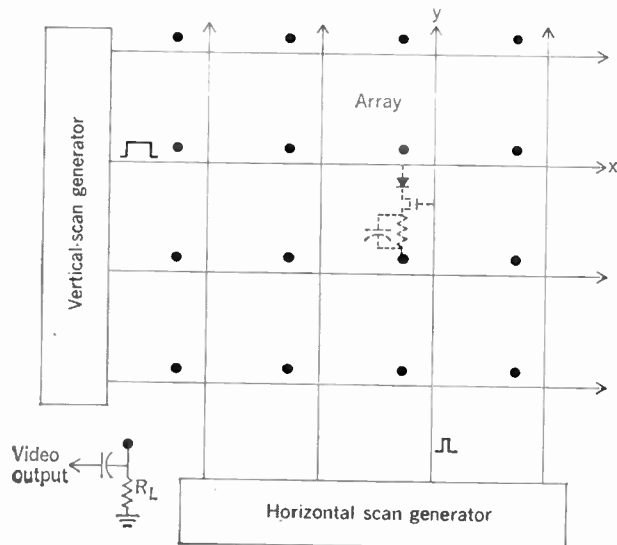
speed scanning. the large internal capacitance existing between the column address strips and the common output may introduce unusually large switching transients at normal television scan rates.

Figure 9 shows how the video signal can be extracted from the row address strips. In this circuit a pair of external transistor gates (T_1 and T_2) attached to each row couples the row being scanned to the amplifier while reverse-biasing all the remaining rows. High-frequency switching transients from the columns into the output signal are therefore much less than if all rows were simultaneously connected to the amplifier. Low-frequency switching transients from the vertical-scan generator do not cause trouble because they can be arranged to occur during the period between lines normally concealed by blanking. This circuit should be particularly suitable for frame-storage operation because all rows not being scanned are reverse-biased. In case the array is not to be operated with frame storage the T_2 transistors can be omitted, and the circuit reduces to a single transistor (T_1) connected to each row. The latter circuit was used for the 180 × 180 element photoconductive-sensor camera described in Ref. 1.

Extraction of the video signal from the columns instead of the rows offers a very simple method of greatly increasing the sensitivity of some types of sensors. Figure 10 shows the circuit used in the 256 × 256 element photoconductive sensor described in the next section. By utilizing the column capacitance of the array itself supplemented by a row of external capacitors, the video-signal current can be increased by line storage 256 times over that obtained from the rows. Current is drawn simultaneously from all elements along a given row and stored in the capacitors prior to discharge into the video output lead. The video coupling transistors that are turned on by the horizontal-scan generator must have a sufficiently low "off" conductance for line-storage operation. Although the simple circuit of Fig. 10 may introduce some loss in vertical resolution through the mixing of charge between successive rows, this effect can be avoided with slightly more complex circuits.

A disadvantage of deriving the video signal from the columns is that precautions must be taken to minimize direct pickup of switching transients from the horizontal-scan generator into the video output. This method of coupling would not appear to offer any signal gain by added line storage for an array that already incorporates charge-storage capacitors at each element. It would be particularly inappropriate with an array whose column strips were themselves photosensitive.

Digital scan generators. The design and fabrication of integrated scan generators is of comparable difficulty to that of the sensor and video coupling circuits. The scan generator must provide up to 500 parallel outputs in a form suitable for easy connection to the array, and it must be capable of operation at pulse rates ranging from 15 kHz or less for the vertical scanner up to 10 MHz for the horizontal-scan generator. Both analog and digital scan generators are of interest, but only the latter presently appear to be capable of meeting conventional television standards.

Digital scan generators can of course be assembled

from commercially available components if size and cost of the camera are not of prime consideration. Connections to the array are still a problem, however, if the array is a large one with closely spaced elements. A more attractive solution, if manufacturing yields are sufficiently high, is to fabricate the scan generators and video coupling circuits simultaneously with the array on a common substrate. A 72 × 5 element silicon-photodiode array has been built with a 72-stage parallel-output shift register [22] for scanning in one direction located on the same silicon chip. Alternatively, one can
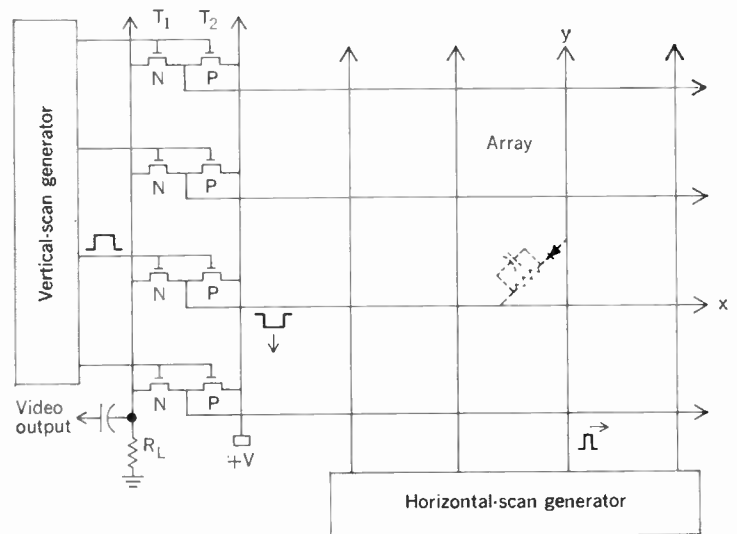
FIGURE 9. Extraction of video signal by use of video coupling circuits connected to the row address strips of the sensor.

FIGURE 10. Extraction of video signal by use of video coupling circuits connected to the column address strips of the sensor.

Weimer, Pike, Sadasiv, Shallcross, Meray-Horvath—Self-scanned sensors
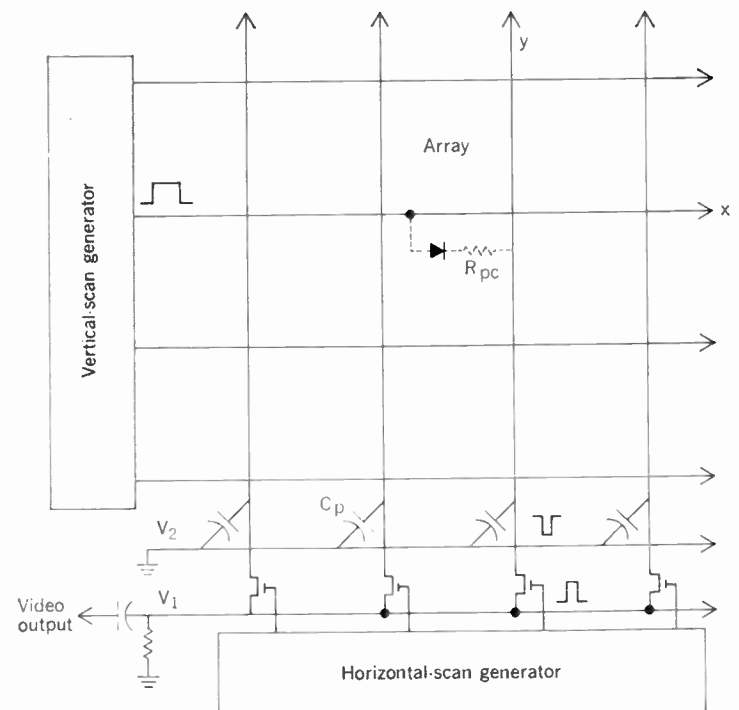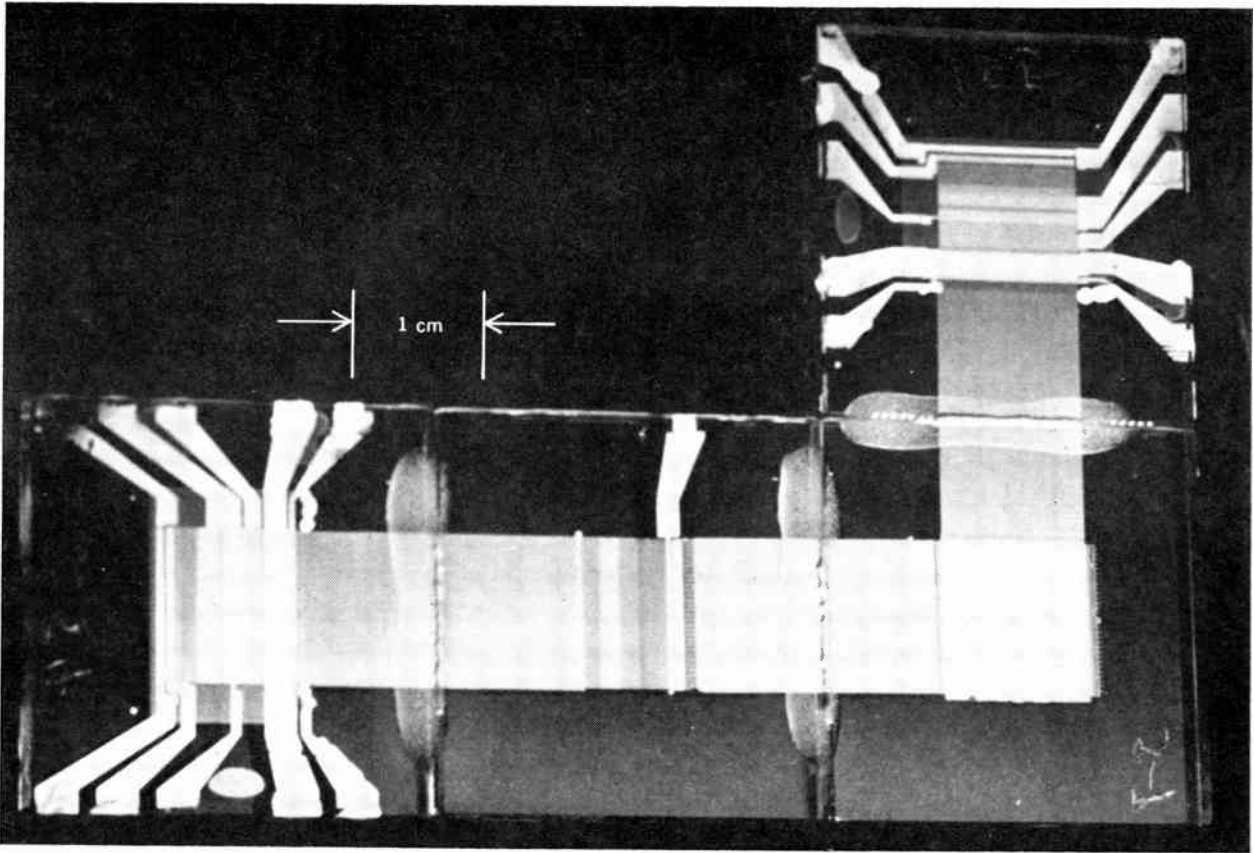
FIGURE 11. Completely integrated 180 × 180 image sensor, including photosensitive array, horizontal-scan generator, vertical-scan generator, and video coupling circuit.
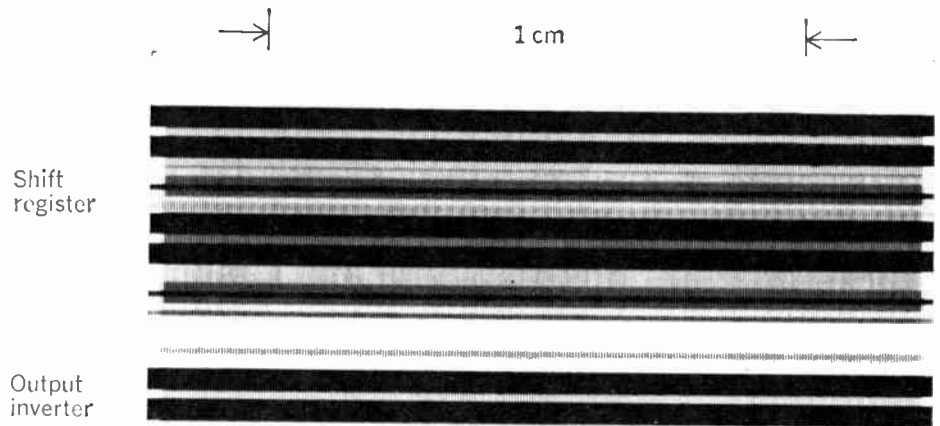
FIGURE 12. Photomicrograph of a 264-stage complementary shift register with an output inverter driver at each stage. The circuit contains 1320 CdSe and 792 Te thin-film transistors.

fabricate integrated scan generators on a separate substrate in a pattern permitting easy connection to the array. The 180 × 180 element thin-film sensor [1] referred to earlier had two 180-stage thin-film shift registers [17] with outputs spaced on 53-μm (2.08-mil) centers deposited on separate substrates, which were subsequently attached to the array. Figure 11 shows the integrated sensor, comprising the 180 × 180 array, the 180 video coupling transistors, and two 180-stage shift registers deposited upon four 2.54- by 2.54-cm (one-inch-square) glass substrates. The four substrates were fastened together with epoxy after the subcircuits were formed, and 180 metal strips were evaporated

across each joint to connect each row and column.

The 180-stage parallel-output shift registers [17] employing CdSe thin-film transistors were fabricated reproducibly by vacuum deposition in one pumpdown of the vacuum system. These units would operate at clock speeds up to 2 MHz and were life-tested for periods up to 10 000 hours. Even larger parallel-output shifts registers were built using complementary CdSe and Te thin-film transistors. Figure 12 shows a 264-stage complementary register [26] with the video coupling circuits included. These experimental units operated at vertical-scan rates but not at a sufficiently high clock rate to serve as the horizontal-scan genera-

tor for sensors operating at broadcast rates.

An alternative to the use of multistage shift registers is to build multistage decoders [26] on the same substrate as the array or attached to it. The decoder itself is driven by counters or shift registers having far fewer stages. For example, each scan generator in the 256 × 256 element sensor described in the next section consisted of a 256-stage decoder, driven by two external 16-stage shift registers. The two decoders thus served to reduce the total number of scanning connections to the array from 512 closely spaced connections to 64 comfortably spaced connections. The 16-stage parallel-output register required for driving the decoder can be produced on a single chip, whereas a 256-stage parallel-output register would be considerably more difficult.

A 256 × 256 element thin-film image sensor with integrated decoders

An experimental solid-state television camera incorporating a 256 × 256 element image sensor scanned by integrated thin-film decoders was recently completed.[27] The array contains 65 536 photoconductor-diode elements connected to perpendicular address strips spaced upon 53-μm (2.08-mil) centers. The entire array is scanned in 1/60 second at an elemental scan rate of 4.8 MHz. The detailed design and construction of the photoconductive array is similar to that used in the 180 × 180 self-scanned sensor shown in Fig. 11.

Figure 13 is a photomicrograph of a portion of the array. Metal address strips and insulator strips were deposited by evaporation through a wire grill mask, but the CdS–CdSe photoconductor strips were defined by photoresist techniques. Diode action at each element was obtained by the use of dissimilar contacts to the photoconductor from the rows and columns. Figure 14 shows the forward and reverse characteristics measured by connecting all rows and all columns in parallel.

An advantage of photoconductive sensors over monolithic silicon lies in the ease of fabrication of operable arrays with high element densities. Many 256 × 256 element arrays have been built having high rectification ratios (10⁴ or greater), and have been entirely free of short circuits. Photoconductors also offer the advantages of high quantum yield (more than 2000 electrons per photon) and sensitivity at long wavelengths. Disadvantages of photoconductors are their greater response times, as well as their more unstable characteristics when they are not encapsulated.

Figure 15 shows the equivalent circuit of the 256 × 256 element thin-film array and its integrated address circuits. The major differences from the earlier 180 × 180 sensor are

1. Extraction of the video signal from the columns to obtain an output signal of 256.
2. The use of integrated decoders instead of multistage shift registers for addressing the array.
3. The larger number of elements.

The significance of these modifications was discussed in the preceding section.

Figure 16 shows the integrated sensor, including the thin-film decoders and video coupling circuits. The diode–resistor decoder used for vertical scanning was deposited on the same 2.54-cm-square glass substrate as the sensor. The transistor-resistor decoder for horizontal scanning and the video coupling circuits were deposited upon a separate 2.54-cm-square glass substrate, which was subsequently joined to the sensor substrate and mounted upon a printed circuit plug-in card. The 256 connections between the video coupling circuits and the sensor were made by evaporating metal strips across the epoxy joint between the substrates.

The construction of the thin-film transistor decoder and video coupling circuits has been discussed in an earlier paper.[26] The video output signal is fed into a dual-input preamplifier to minimize pickup of switching transients in the output signal. The major portion of the video signal is obtained from the transistor bus labeled V_1 in Fig. 15. The video-signal current from the capacitor bus V_2 would be equal and opposite to that flowing in the V_1 lead if the entire charge were stored in the external capacitors C_p. In practice, a portion of the charge is stored in the column crossovers in the array itself, so that the video signal from V_2 is somewhat smaller than from V_1. However, the
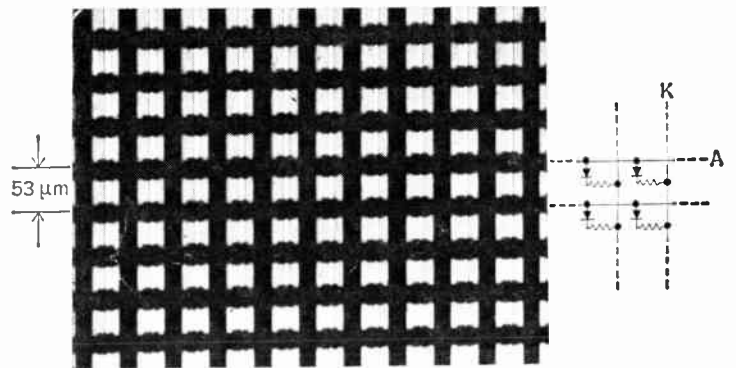
FIGURE 13. Photomicrograph of a portion of the 256 × 256 element photoconductor-diode array having elements spaced on 53-μm centers.

FIGURE 14. Forward and reverse current vs. voltage for the 256 × 256 element CdS–CdSe array having all anode and cathode strips connected in parallel.
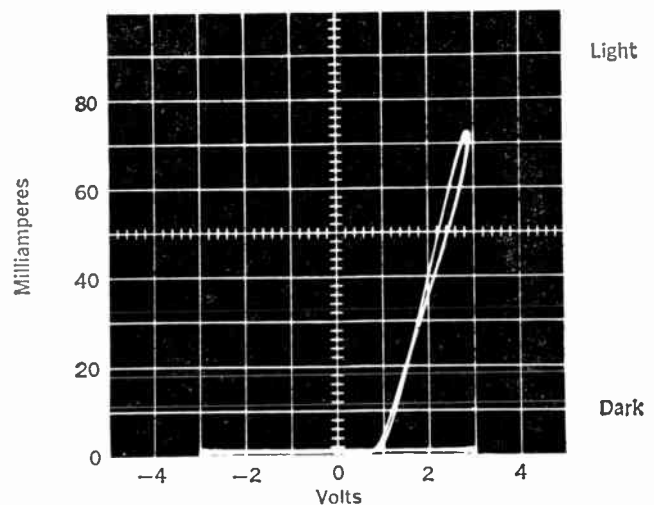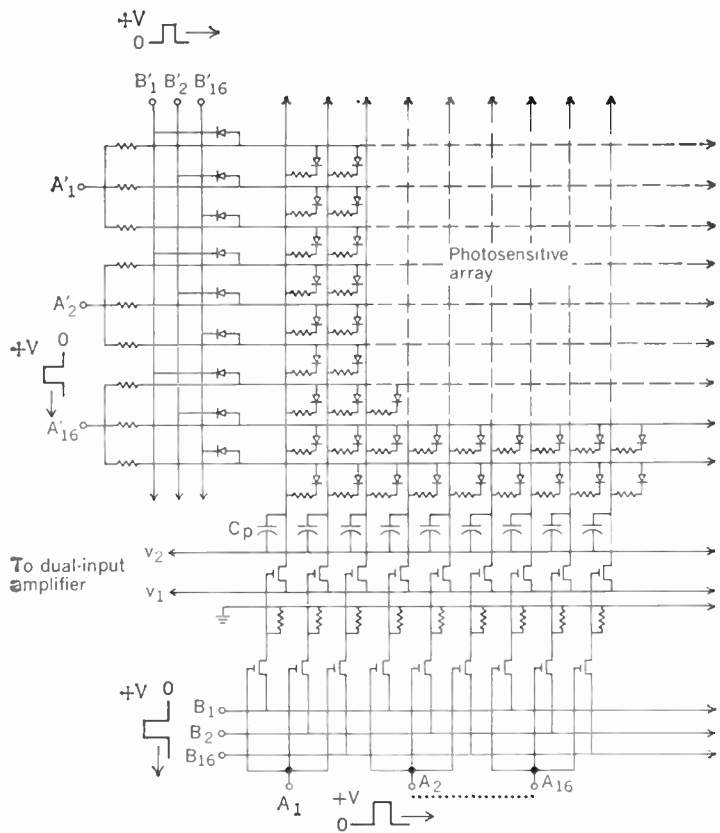
FIGURE 15. Equivalent circuit for the 256 × 256 element integrated sensor, including a transistor decoder for horizontal scanning, a diode decoder for vertical scanning, and video coupling circuit for signal enhancement by line storage.

switching transients from the horizontal-scan generator picked up in V_1 and V_2 are comparable in size and polarity. The composite signal formed by subtracting V_2 from V_1 is accordingly larger in amplitude and has considerably reduced transients than would be obtained from either channel alone. The suppression of switching transients by this method is less than perfect, however, and transient pickup constitutes one of the major problems in the operation of large arrays at fast scanning rates. Other methods, such as filtering and sample-and-hold techniques, are under investigation.

The Schottky-barrier diode used for the vertical decoder is formed by evaporation of successive layers of gold, indium, cadmium sulfide, tellurium, and gold. Although more power is consumed by the diode decoder than by the transistor decoder, only 16 out of 256 resistors are passing current at any one time. The vertical decoder must be able to supply each row of the sensor with a current equal to the maximum video signal at the highest illumination level and with negligible voltage drop.

An experimental television camera incorporating the 256 × 256 integrated sensor was built and delivered to the U.S. Air Force. Figure 17 shows the integrated sensor being plugged into the camera head. Also included in the camera head are four 16-stage shift registers, a dual-input preamplifier, and the horizontal and vertical clock supplies. The shift registers were built up from commercially available logic modules. In a commercial camera one would expect to use integrated 16-stage silicon registers for driving the decoder.

Figure 18 shows two pictures transmitted by the 256 × 256 element integrated sensor operating at the 4.8-MHz element rate. The resolution indicated by the test pattern is approximately 200 television lines in both the horizontal and vertical directions. Although deterioration of vertical resolution can result from mixing of stored charge between successive rows, this was not particularly apparent in the picture. Horizontal resolution loss can be caused by unwanted broadening of the horizontal scanning pulse. The vertical streaks arise from nonuniformities in the sensor, in the horizontal decoder, or in the connections between the two. The spurious signals introduced by minor defects tend to be repeated 16 times because of the decoder interconnections. Recent work indicates that these nonuniformities in signal can be greatly reduced.

The operating sensitivity of the 256 × 256 element sensor was sufficient for transmission of pictures under
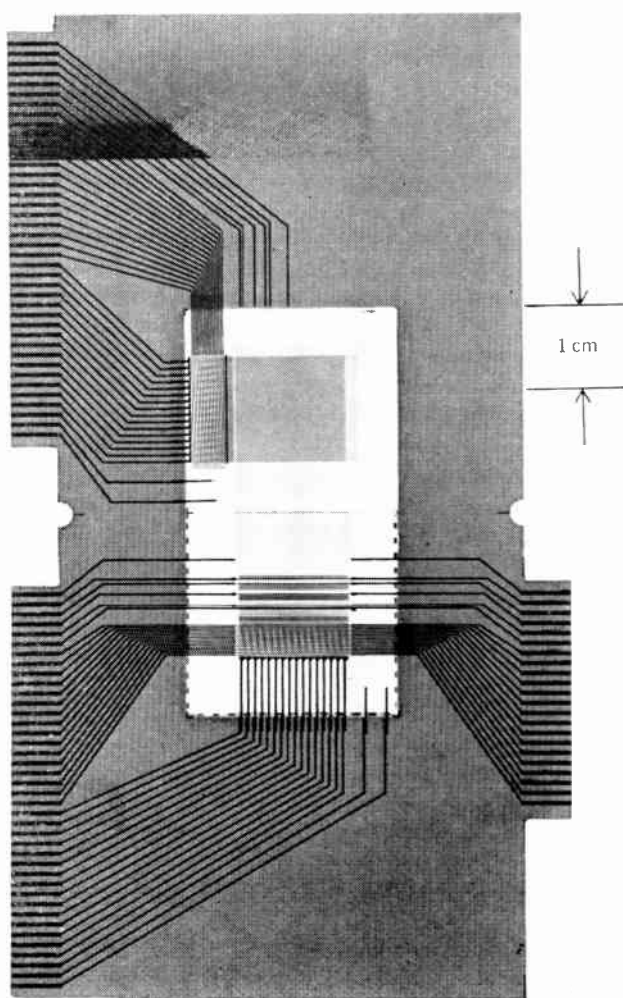
FIGURE 16. Complete 256 × 256 element integrated thin-film image sensor deposited upon two glass substrates mounted on a printed-circuit board.

60

normal laboratory illumination. Although the video-signal output current was increased by a factor of 256 by the use of line storage, the overall sensitivity increase was less than this factor because of greater switching transients. A more effective control of switching transients should permit operation with an illumination on the sensor of less than a footcandle (about 10.8 lumens per square meter).

Although further refinements in the 256 × 256 element sensor would certainly lead to improved picture quality, it is evident that for performance comparable

to that of television camera tubes the total number of picture elements and the number of elements per unit area must be increased. Higher clock frequencies and more effective suppression of switching transients will be required to maintain standard scan rates. The photoconductive approach using evaporated thin-film techniques appears to be capable of extension to at least 500 × 500 elements spaced upon 25-μm centers.

A novel self-scanned photodiode array

The requirements for reduction in picture-element size and increase in total number of elements has led to a search for new sensor designs that may permit considerable simplification in fabrication procedures. In each of the self-scanned arrays illustrated in Figs. 3–6 the basic circuit for each element consists of a photosensor in series with a switch. Even a phototransistor, when operated in the pulsed mode, behaves like a photodiode sensor (collector junction) in series with a switching diode (emitter junction). A novel method has been developed for operating a photodiode with charge storage in which the same diode serves alternately as a reverse-biased photodiode sensor and as a forward-biased discharge switch.[28] The basic circuit element consists of a photodiode in series with a capacitor. Figure 19 shows the idealized operating cycle of a single-line sensor in which a row of photodiode-capacitor elements is employed.[*] Each photodiode is equivalent to a switching diode in parallel with a photoconductor R_{pc} and a shunt capacitor C_x. Sampling pulses having the proper polarity to forward-bias the diodes are applied to the series capacitors by a scan generator. The series capacitor C is made large compared with the internal shunt capacitance C_x of the photodiode. The latter capacitance may therefore be neglected, since it plays a role in the operation that is only secondary—comparable to that of the switch capacitance in the earlier systems. During the sampling period a positive pulse V applied to the capacitor causes the potential of point P to be driven to a

FIGURE 17. Integrated 256 × 256 element sensor card being plugged into experimental camera.

* The effect of minority-carrier storage in the photodiode has not been included in the present discussion.

FIGURE 18. Pictures transmitted by the 256 × 256 element integrated sensor.
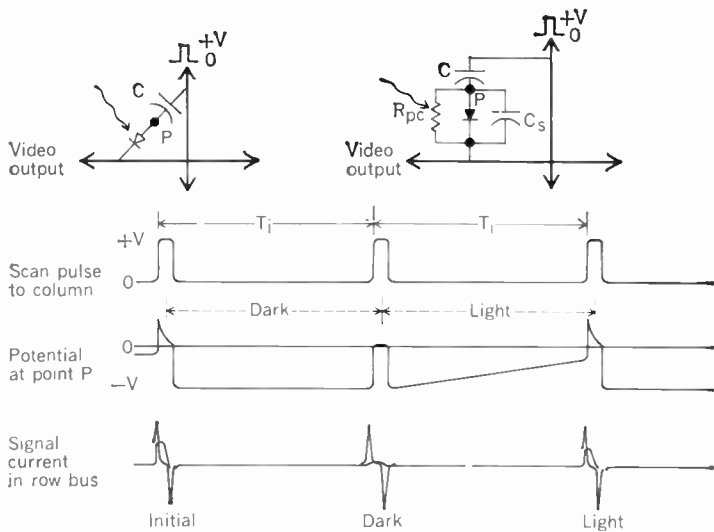
FIGURE 19. Charge-storage operation of a single row of photodiode–capacitor elements.

FIGURE 20. Sensor-element circuits for two novel photodiode–capacitor arrays.

A   **B**
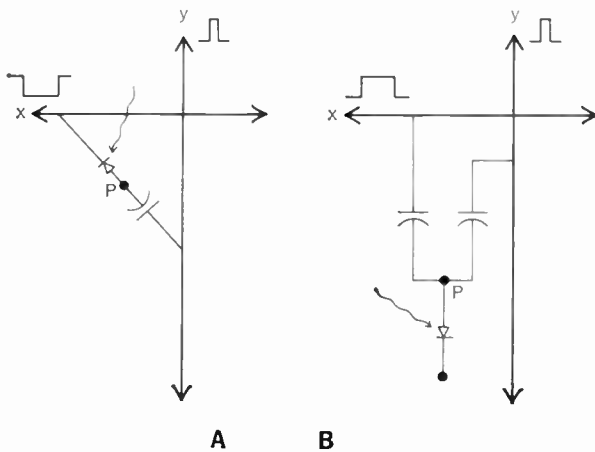
FIGURE 21. Charge-storage operation of the photodiode–capacitor array shown in Fig. 20(A).
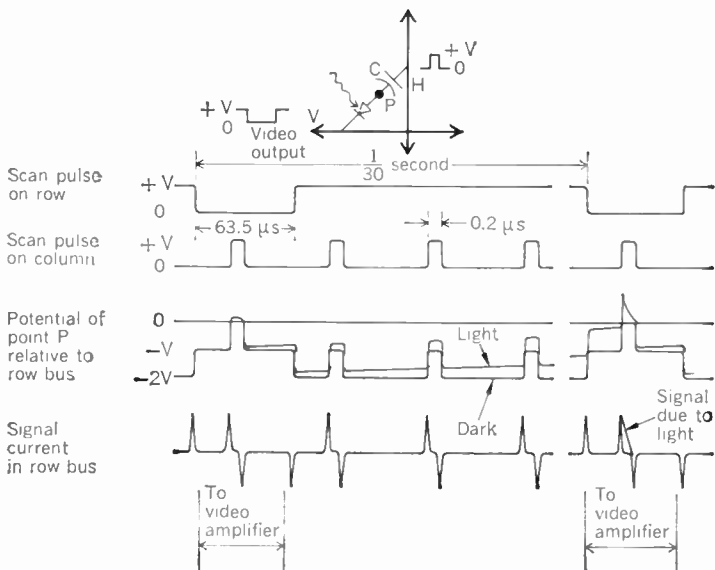
reference potential slightly positive with respect to ground by an amount determined by the offset voltage and forward conductance of the diode. At the end of the sampling period, the fall of the scan pulse causes point P to be driven negative by V volts, thereby establishing a reverse bias on the photodiode. The photodiode remains reverse-biased through the succeeding integration period, provided that the RC time constant set by the series capacitor and the dark resistance of the photodiode greatly exceeds T_i.

If the photodiode is not illuminated during the integration period, the current pulse flowing through the photodiode–capacitor circuit during the next sampling period will be a minimum. If the photodiode is illuminated during the integration period the potential of point P will gradually rise as the series capacitor C is discharged. A much larger current pulse will then flow during the sampling pulse, since more current is required to recharge the capacitor C. The fluctuating current flowing in the external load resistor R_L, as successive elements are sampled, comprises the video signal. Although no *direct* current flows through the external load resistor because of the capacitive coupling at each element, the dc level of the video signal can be established at the beginning of each row by "clamping" on the signal from an unilluminated element. The differentiated signals, shown in color in Fig. 19, at the beginning and end of each output pulse are the unwanted switching transients introduced through the shunt capacitance of the photodiodes and through other stray paths. As discussed earlier, such transients can be suppressed from the video signal by such external circuit techniques as bucking, phase sampling, or filtering.

Figure 20 shows two types of photodiode–capacitor elements suitable for a two-dimensional array. Although the operation of each is basically the same as described for the single-line sensor of Fig. 19, the use of both vertical and horizontal scanning pulses modifies the charge–discharge voltage sequence for the circuit of Fig. 20(A), as shown in Fig. 21. If the scanning pulses are applied only to the columns the integration time T_i is one line-time (63.5 μs) for each element, but if the slower pulses are also applied to the rows the integration time is increased to 1/60 second.

The foregoing features of operation have been demonstrated with a single row of 256 p$^+$ photodiodes formed on 51-μm centers on a chip of n-type silicon. A silicon oxide–aluminum capacitor was formed on top of each photodiode and was connected to a 256-stage thin-film decoder deposited on a supporting glass plate. The silicon chip was attached with epoxy to a groove in the glass plate, as shown in Fig. 22.

By using the 4.8-MHz clock drive on the decoder, line-storage operation was obtained, but this could be increased to 1/60-second storage by pulsing the silicon substrate at 60-Hz intervals, as indicated in Fig. 21. A television picture obtained by moving a light image across the line sensor is shown in Fig. 23.

The two-capacitor array of Fig. 20(B) is of interest because it will permit self-scanning operation of a simple array of photodiode elements formed upon a common substrate. As shown in Fig. 24, the coincidence of positive pulses applied to the two capacitors causes
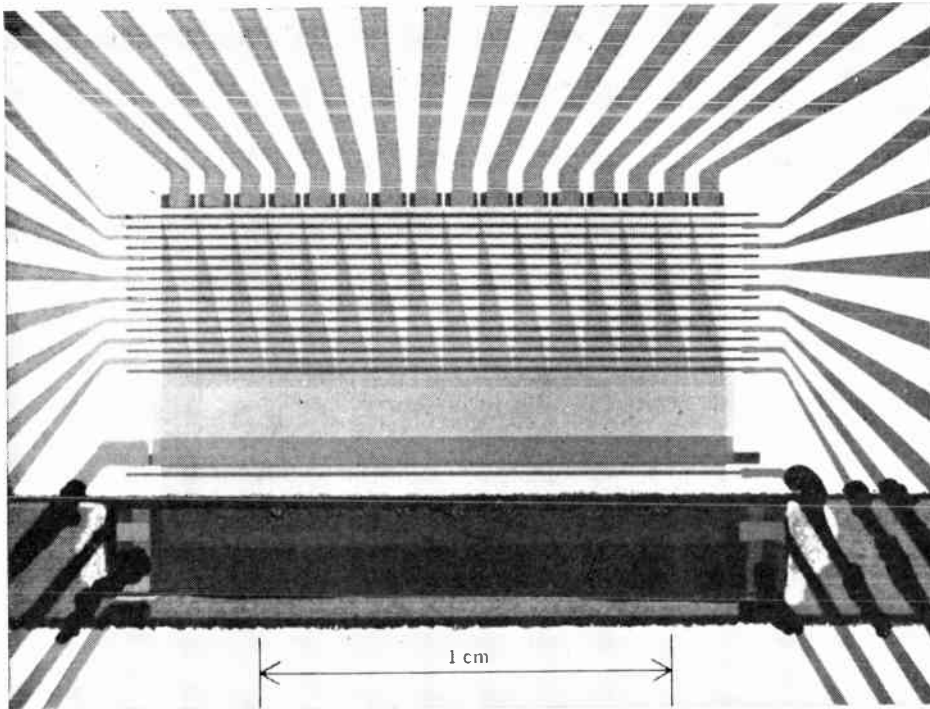
FIGURE 22. A 256-element silicon photodiode–capacitor line sensor connected to a thin-film decoder for scanning tests.

the element to be scanned. The video signal can be derived from the common substrate, as in Fig. 8, or from the row strips using a video coupling circuit of the type shown in Fig. 9. Extraction of the signal from the rows is expected to yield higher sensitivity than from the substrate because of the reduced switching transients from a single line.

Figure 25 shows a simple method of constructing a self-scanned two-capacitor photodiode array by depositing the address strips across the top of each photodiode. This structure should permit reduction of element sizes to less than 25 μm. This photodiode array by itself, excluding the address strips, is similar in construction to the beam-scanned photodiode arrays used in the silicon vidicon.[12] The extension of the single-line photodiode–capacitor sensor to two-dimensional arrays is now under investigation. Optimization of the design parameters and the control of switching transients at high scan rates are the major problems.

FIGURE 23. Television picture transmitted by a single row of photodiode–capacitor elements operated at an element rate of 4.8 MHz.

Summary and conclusions

Recent progress in the fabrication of self-scanned image sensors by thin-film and silicon techniques indicates that such devices will play an increasingly important role in image transmission. Their potential improvements over beam-scanned sensors lie in a greater versatility and accuracy in addressing; in reduced size, weight, and power requirements; and in improved life and ease of operation. Although image sensors are still inferior to camera tubes in performance and cost, these factors are steadily being improved.

The present approaches to fabrication of self-scanned sensors are based upon thin-film technology, silicon technology, and combinations of the two. Thin-film sensors have been produced with a larger total number of elements, with higher element densities,

and with more extensive integration of scan generators and video coupling circuits than has been reported for silicon. These arrays have been incorporated into experimental cameras and scanned at higher frequencies than with silicon. The relatively higher yields obtained with thin-film techniques suggest that integrated arrays having at least 500×500 elements on 25-μm centers can be produced at reasonable cost. A disadvantage of the thin-film approach, however, is that the fabrication techniques have not yet been developed beyond the research stage, and the devices produced tend to lack ruggedness and stability in operation. Silicon offers the resources of an established technology that is continuing to advance through the efforts of an entire industry. The weakness of the silicon approach at the
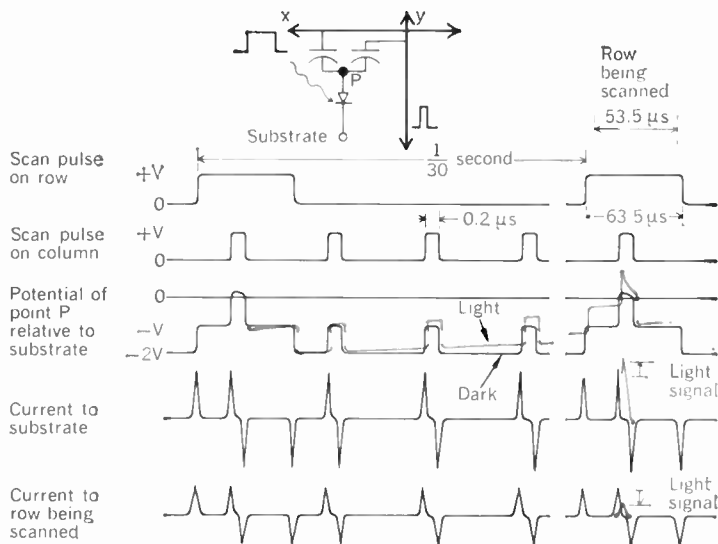
FIGURE 24. Charge-storage operation of the two-capacitor photodiode array shown in Fig. 20(B).

FIGURE 25. A proposed method for fabricating a simple two-capacitor photodiode array.
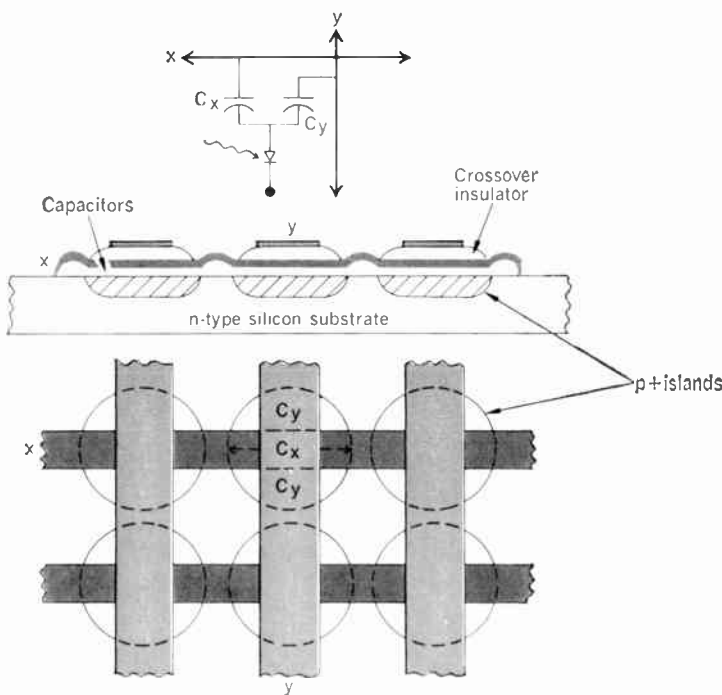
present time lies in the difficulty of achieving the required number of elements and the required degree of integration at reasonable cost. Novel approaches in which the advantages of silicon and thin films are combined may offer a solution to this problem.

The relative merits of photoconductors, photodiodes, and phototransistors cannot be completely evaluated on the basis of available information. The present review has attempted to point out the common properties as well as the particular advantages of each type of sensor. For example, photoconductors offer high quantum gain in very simple structures, but their re-

sponse time for changes in light level at low lights may exceed 1/30 second. Silicon photodiodes have only unity gain but can operate at very low light levels using charge storage. Silicon phototransistors have the attractive feature of providing both charge storage and transistor gain. However, variations in transistor gain from element to element will produce grainy pictures, and capacitive lag can limit speed of response at low light levels.

Each of the three types of sensors should be capable of an operating sensitivity equal to or exceeding that of the vidicon, particularly if additional gain mechanisms are incorporated into the element. It is evident that any meaningful comparison of the expected operating sensitivities of the various types of arrays for television purposes would have to be made with equivalent large-size arrays operating at the required scan rates.

The large number of image sensor designs discussed here represent only a fraction of the possible ways of building image sensors. New designs and methods of fabrication that are particularly suited to the required application will certainly evolve. Much research and development remain to be done before solid-state sensors can compete with beam-scanned tubes for routine television purposes.

REFERENCES

1. Weimer, P. K., Sadasiv, G., Meyer, J. E., Jr., Meray-Horvath, L., and Pike, W. S., "A self-scanned solid-state image sensor," *Proc. IEEE*, vol. 55, pp. 1591–1602, Sept. 1967.

2. Noble, P. J. W., "Development and potential of optoelectronic techniques," *Component Technol.*, vol. 2, pp. 23–28, Dec. 1967.

3. Horton, J. W., Mazza, R. V., and Dym, H., "The scanistor —a solid-state image scanner," *Proc. IEEE*, vol. 52, pp. 1513–1528, Dec. 1964.

4. Linvill, J. G., and Bliss, J. C., "A direct translation reading aid for the blind," *Proc. IEEE*, vol. 54, pp. 40–51, Jan. 1966.

5. Special Issue on Solid-State Imaging, *IEEE Trans. Electron Devices*, vol. ED-15, Apr. 1968.

6. Weckler, G. P., "Operation of p-n junction photodetectors in a photon flux integrating mode," *IEEE J. Solid-State Circuits*, vol. SC-2, pp. 65–73, Sept. 1967.

7. Noble, P. J. W., "Self-scanned image detector arrays," *IEEE Trans. Electron Devices*, vol. ED-15, pp. 202–209, Apr. 1968.

8. Anders, R. A., Callahan, D. E., List, W. F., McCann, D. H., and Schuster, M. A., "Developmental solid-state imaging system," *IEEE Trans. Electron Devices*, vol. ED-15, pp. 191–196, Apr. 1968.

9. Dyck, R. H., and Weckler, G. P., "Integrated arrays of silicon photodetectors for image sensing," *IEEE Trans. Electron Devices*, vol. ED-15, pp. 196–201, Apr. 1968.

10. Joy, R. C., and Linvill, J. G., "Phototransistor operation in the charge storage mode," *IEEE Trans. Electron Devices*, vol. ED-15, pp. 237–248, Apr. 1968.

11. Soref, R. A., "Monolithic silicon mosaics for far-infrared imaging," *IEEE Trans. Electron Devices*, vol. ED-15, pp. 209–214, Apr. 1968.

12. Crowell, M. H., Buck, T. M., Labuda, E. F., Dalton, J. V., and Walsh, E. J., "An electron beam accessed image sensing silicon diode array with visible response," *1967 Internat'l Solid-State Circuits Conf. Dig. Tech. Papers*, vol. 10, pp. 128–129, Feb. 1967.

13. Weimer, P. K., Borkan, H., Meray-Horvath, L., and Shallcross, F. V., "Solid-state image sensors," Tech. Doc. Rept. RTD-TDR-63-4033, Research and Tech. Div., AF Avionics Lab., Wright-Patterson Air Force Base, Ohio, Oct. 31, 1963.

14. Weimer, P. K., Borkan, H., Sadasiv, G., Meray-Horvath, L., and Shallcross, F. V., Tech. Doc. Rept. AL-TDR-64-56, AF Avionics Lab., Apr. 15, 1964.

15. Weimer, P. K., Sadasiv, G., Meyer, J. E., Jr., Meray-Horvath, L., and Pike, W. S., Tech. Doc. Rept. AFAL-TR-66-381, AF Avionics Lab., Dec. 1966.

16. Weimer, P. K., Sadasiv, G., Pike, W. S., Meray-Horvath, L., "Solid-state digital scanning of mosaic sensors," Tech. Doc. Rept. AFAL-TR-68-82, AF Avionics Lab., Apr. 1968.

17. Weimer, P. K., Sadasiv, G., Meray-Horvath, L., and Homa, W. S., "A 180-stage integrated thin-film scan generator," Proc. IEEE, vol. 54, pp. 354–360, Mar. 1966.

18. Weimer, P. K., "The TFT—a new thin-film transistor," Proc. IRE, vol. 50, pp. 1462–1469, June 1962.

19. Weimer, P. K., Borkan, H., Sadasiv, G., Meray-Horvath, L., and Shallcross, F. V., "Integrated circuits incorporating thin-film active and passive elements," Proc. IEEE, vol. 52, pp. 1479–1486, Dec. 1964.

20. Weimer, P. K., Forgue, S. V., and Goodrich, R. R., "The vidicon—a photoconductive television camera tube," Electronics, vol. 23, pp. 70–73, May 1950; also RCA Rev., vol. 12, p. 306, Sept. 1951.

21. Brugler, J. S., "Low-light-level limitations of silicon-junction photodetectors," Tech. Rept. 4824-1, Stanford Electronics Laboratories, May 1968.

22. Noble, P. J. W., paper presented at the Solid State Devices Conference, University of Manchester, England, Sep. 3–6, 1968.

23. Schuster, M. A., and Strull, G., "A monolithic mosaic of photosensors for solid-state imaging applications," IEEE Trans. Electron Devices, vol. ED-13, pp. 907–912, Dec. 1966.

24. Anders, R. A., Callahan, D. E., Erwin, E. L., List, W. F., McCann, D. H., Mend, W. G., Saboe, J. M., and Schuster, M. A., "Developmental solid-state imaging system," 1968 Govt. Microcircuit Applications Conf. Dig. Tech. Papers, vol. 1, pp. 148–150.

25. Weckler, G. P., "Solid-state image sensors," paper presented at the 1968 Solid State Sensors Symposium, Minneapolis, Minn., Sept. 12–13.

26. Sadasiv, G., Weimer, P. K., and Pike, W. S., "Thin-film circuits for scanning image-sensor arrays," IEEE Trans. Electron Devices, vol. ED-15, pp. 215–219, Apr. 1968.

27. Weimer, P. K., Sadasiv, G., Pike, W. S., and Meray-Horvath, L., "A 256 × 256 element thin-film image sensor with integrated addressing circuits," 1968 Govt. Microcircuit Applications Conf. Dig. Tech. Papers, vol. 1, pp. 305–307.

28. Weimer, P. K., Pike, W. S., Sadasiv, G., and Shallcross, F. V., "Multielement self-scanned mosaic sensors," presented at the IEEE Internat'l Electron Devices Meeting, Washington, D.C., Oct. 23–25, 1968.

W. S. Pike received the B.A. degree in physics in 1941 from Williams College and entered the U.S. Army Signal Corps as a radar officer shortly thereafter. Following service in Europe and the southwest Pacific he was discharged as a captain in 1946 and joined the technical staff of RCA's David Sarnoff Research Center. He has done work on sensory aids for the blind, storage tubes and their applications, color television receivers and cameras, highway vehicle control devices and systems, industrial and educational television camera chains, electronic devices for medical applications, high-altitude balloon-borne television systems for astronomical observations, and camera systems employing solid-state sensors. Mr. Pike is the author or coauthor of more than 20 technical papers and holds approximately 20 patents.

G. Sadasiv received the B.S. degree from Saugar University, Madhya Predesh, India, in 1950 and the M.S. degree in physics from Allahabad University, Uttar Pradesh, India, in 1952. From 1952 to 1956 he was with the Optics Division of the National Physical Laboratory of India, New Delhi, where he worked on the optical absorption spectra of rare-earth salt crystals. From 1957 to 1963 he was with the Physics Department at Purdue University, where he was involved in heat-capacity measurements at low temperatures and transport properties of semiconductors at low temperatures. He received the Ph.D. degree from Purdue in 1963. Since then he has been associated with RCA Laboratories, where he has been working on thin-film devices and thin-film integrated circuits.

F. V. Shallcross received the A.B. degree in chemistry from the University of Pennsylvania in 1953. He did graduate research work in X-ray crystallography and received the Ph.D. degree in physical chemistry from Brown University in 1958. He was employed as a chemist by M. & C. Nuclear, Inc., Attleboro, Mass., from 1957 to 1958. He then joined RCA Laboratories, where as a member of the staff of the Electronic Research Laboratory he has worked in research on laser materials, thin-film photoconductors and semiconductors, television camera tubes, thin-film active devices, and integrated circuits.

P. K. Weimer (F) received the A.B. degree from Manchester College, Indiana, in 1936, the M.A. degree in physics from the University of Kansas in 1938, and the Ph.D. degree in physics from Ohio State University in 1942. From 1937 to 1939 he taught physics and mathematics at Tabor College, Kansas. Since 1942 Dr. Weimer has been engaged in research at RCA Laboratories, where he is a technical staff Fellow. During this period he has participated in the basic development of various types of television tubes and solid-state devices. From 1959 to 1960 he was granted an RCA fellowship for study abroad, which was spent in semiconductor research at the Laboratoire de Physique, Ecole Normale Superieure, Paris. He is the recipient of numerous awards, including the IRE Vladimir K. Zworykin Television Prize in 1959, the RCA David Sarnoff Outstanding Achievement Award in Science in 1963, and the 1966 IEEE Morris N. Liebmann Prize Award. In 1968 he received the honorary doctor of science degree from Manchester College.

L. Meray-Horvath (M) received the B.S. degree in mechanical engineering in 1941 and the M.S. degree in mechanical sciences in 1944 from Jozsef Nador University, Budapest, Hungary. He also completed several postgraduate courses at the Eidgenossische Technische Hochschule, Zurich, Switzerland, and the University of Toronto. From 1948 to 1951 he worked for Luwa, A.G., Zurich, on thin-film vacuum evaporation and atomizer systems for the food industry. Since that time he has worked in Canada as a mechanical design engineer and a ceramics engineer, and also has worked with the Curtiss-Wright Corporation on R&D projects. He joined RCA Laboratories in 1961, where he is working on thin-film transistors.

FIGURE 1. Original photograph. The brightness values in this portrait were sampled at 1024 by 1024 points, quantized to 2048 discrete levels, and fed into a digital computer for subsequent processing. The variously transformed brightness data were reconverted into photographic images by means of a microfilm plotter under computer control (see Figs. 2–9, 12–16, and 18).

Images from computers

Manfred R. Schroeder   *Bell Telephone Laboratories, Inc.*

Modern digital computers, in conjunction with microfilm plotters, are capable of generating a wide variety of images. Beyond the mere plotting of curves, graphs, and labels, special programming techniques can produce halftone renditions of pictorial material with wide applications in optical signal processing and data portrayal. Other possibilities include the composition of images from alphanumeric characters, the generation of moiré patterns, and the encryption of images with subsequent recovery by optical means using computer-generated "keys." More sophisticated techniques allow the combining in a single optical display of different kinds of information in hitherto unforeseen ways.

Microfilm plotters are among the most useful output devices of digital computers. Their value in producing permanent graphical records is, in many respects, unsurpassed. Regrettably, models presently employed have no provision for producing images with a continuous gray scale or "halftones." However, good approximations to halftones can be obtained by appropriate programming techniques or "software." Several programs for obtaining halftone images from computer-controlled microfilm plotters are described here.

The original impetus for this article was the desire to produce, on a digital computer, spectrograms of speech sounds with time as the abscissa, frequency as the ordinate, and spectral intensity on a gray scale. Another early application was the processing of halftone pictures on digital computers in order to remove linear motion blur. In general, the programming techniques described here are useful for plotting physical, psychological, or other data that require a continuous third dimension for better visualization. Successive frames of such data can also be combined into a cinematographic representation to exhibit temporal effects or the dependence of the data on a third independent variable.

In addition to the realization of halftones by software,

This article is based on a paper that appeared in the February 1969 issue of *Communications of the ACM* under the title "Images from Computers and Microfilm Plotters." Copyright 1969 by the Association for Computing Machinery, Inc.

FIGURE 2. Microfilm plotter output obtained from Fig. 1 by plotting only points whose brightness exceeded a fixed threshold. There are only "blacks" and "whites," no intermediate gray tones, reflecting the limitations of existing microfilm plotters, which were designed for producing graphs, alphanumeric characters, and other high-contrast material.

Various interpolation strategies and random-number generating routines have led to a limitless variety of visual patterns and images that can simulate either physical objects and mathematical abstractions—or just pure fantasy

modern digital computers, in conjunction with microfilm plotters, can produce a wide variety of images beyond the mere plotting of curves and graphs. Several such applications are described here, including the composition of images from alphanumeric characters, the generation of moiré patterns, and the encryption of images and their recovery by optical means using computer-generated "keys."

Basic capabilities of microfilm plotters

In addition to the capability of reproducing alphanumeric characters, microfilm plotters can make line drawings. These drawings are produced on the screen of a cathode-ray tube, where an electron beam produces a luminous point whose position is controlled by the computer. In one device (Stromberg-Carlson Model 4020), the beam direction, and therefore the location of the illuminated point, can take on 2^{10} discrete horizontal positions and 2^{10} vertical positions.* Straight lines, curves, grids, and other graphical patterns are obtained by successive illumination of points. During this process, the phosphorescent screen is photographed in time-exposure manner. In the SC 4020, the nonzero intensity of the illumination cannot be varied under computer control. Thus, different film areas are either opaque or translucent, without significant intermediate values of optical transmittance.

In a late model microfilm plotter, the SC 4060 (with a resolution of 2^{12} by 2^{12} points), the brightness of individual points can be controlled by the computer in four discrete levels. Plotters with a continuous or near-continuous brightness scale, however, are still not available commercially.

The effect of brightness-level discreteness is illustrated in Figs. 1 and 2. Figure 1 shows a reproduction of the original photograph, and Fig. 2 the output of an SC 4020

* In conventional applications of microfilm plotters, the exposure of the film is usually such that the developed image of a single point overlaps two or three adjacent points both horizontally and vertically. Thus, the nominal resolution (2^{10} by 2^{10} points in the case of the SC 4020) is not fully realized in practice. However, in most of the applications described here, the camera in the microfilm plotter is set in the range $f11$ to $f22$, yielding a substantially improved resolution as a result of the low exposure—except when this exposure is highly iterated, as will be seen.

FIGURE 3. Reproduction of Fig. 1 using the multiple-exposure technique. Instead of each point in the image being exposed exactly once (or not at all) as in Fig. 2, the number of exposures for each point is variable depending on the corresponding brightness value of the original photograph. The resulting contours reflect the discreteness of this "overwriting" exposure technique.

FIGURE 4. Reproduction of Fig. 1 using probabilistic interpolation strategy. Here the contours visible in Fig. 3 have been obliterated by employing a random rule for rounding between discrete exposure values.

microfilm plotter under control of an IBM 7094 digital computer. Figure 2 was obtained as follows: The optical transmittance of the original transparency (Fig. 1) was measured and sampled at 1024 by 1024 points in a square grid, quantized to 2048 discrete levels. The sampled and quantized picture information was recorded on digital magnetic tape and fed into the computer, which was programmed to expose a point in the grid of the microfilm plotter if the corresponding optical transmittance in the original exceeded a fixed threshold. A reproduction of the resulting black-and-white picture with no intermediate gray values is shown in Fig. 2. The usefulness of this mode of image reproduction is, of course, limited, especially for graphic representations that critically depend on a many-valued gray scale.

Multiple exposure

One method of obtaining intermediate gray values or "halftones" involves *multiple exposure* of the individual points in the grid of a microfilm plotter, resulting in different optical densities or transmittances of the microfilm. In addition, the optical transmittance associated with each point increases with an increasing number of exposures because of a growing halo surrounding each point.

A useful, and for many purposes adequate, approximation to the dependence of the optical transmittance T (of the reversal film customarily used in microfilm plotters) on the number of exposures n is given by the following logarithmic law*:

$$T(n) = (T_{max} - T_{min}) \cdot \log_N (1 + n) + T_{min}$$

$$n = 0, 1, \cdots, N - 1 \qquad (1)$$

where $N - 1$ is the maximum number of exposures, T_{max} is the corresponding maximal transmittance of the microfilm transparency, and T_{min} is the transmittance of the unexposed film ($n = 0$).

For convenience, a normalized transmittance

$$t = \frac{T - T_{min}}{T_{max} - T_{min}}$$

will be used here. In terms of this normalized transmittance, (1) reads as follows:

$$t(n) = \log_N (1 + n) \qquad n = 0, 1, \cdots, N - 1 \quad (2)$$

Thus t increases from 0 to 1 as n increases from 0 to $N - 1$.

FIGURE 5. Enlargement of lip area of Fig. 4, illustrating the "stipple" technique of approximating halftones resulting from the random rounding rule.

The accuracy of the Eq. (2) approximation for a given reversal film, developer, and optical system depends on the (manually adjustable) f-stop setting used in the camera of the microfilm plotter. Good results have been achieved with settings that result in transmittances for single exposures of $t(1) \approx 0.3$ corresponding to $N = 10$. Other values of N, in the range from 6 to 100, have also been used successfully.

Figure 3 displays a microfilm plotter reproduction of Fig. 1 using multiple exposure with $N = 10$. In contrast to the binary-valued, black-and-white, "silhouette"-like representation of Fig. 2, a more recognizable replica of the original is obtained. However, the discrete quantization levels of the transmittance give rise to extraneous contours not present in the original. In the following, strategies for avoiding these contours are described.

Probabilistic interpolation strategy

In order to eliminate undesirable contours between regions of different discrete exposures, the following probabilistic interpolation strategy may be employed.

According to Eq. (2), the "correct" number of exposures n, of a given point in the original image is found by inverting Eq. (2):

$$n_i = N^{t_i} - 1 \qquad (3)$$

where t_i is the transmittance corresponding to the brightness of the original at point i.

Except for special values of t_i, the number of required exposures n_i is not an integer and, therefore, cannot be executed. By rounding off n_i to the nearest integer, a picture with contours, such as Fig. 3, will result. In order to avoid these contours, *probabilistic rounding* is employed, in which the number of exposures is given by

$$\tilde{n}_i = [n_i + r_i] = [N^{t_i} - 1 + r_i] \qquad (4)$$

where the r_i are independent uniform random variables in the range 0 to 1, chosen independently for each picture point; and $[n_i + r_i]$ denotes the largest integer

that is not greater than $n_i + r_i$.

For example, with Eq. (4) and $n_i = 4.7$, $\tilde{n}_i = 4$ with probability 0.3 and $\tilde{n}_i = 5$ with probability 0.7.

Figure 4 shows a reproduction of a microfilm output obtained in this way using ten discrete values of exposure ($n = 0, 1, 2, \cdots, 9$). The probabilistic relation between the correct transmittance t, and the actual one is reflected in the "graininess" of the resulting image. This graininess is clearly seen in the partial enlargement reproduced in Fig. 5. This illustration also shows the "mosaic" structure of the microfilm image, i.e., its composition of many individual dots. Because of photographic grain, the dots are shaped rather irregularly.

It is evident that such a probabilistic procedure for obtaining halftones, although convenient to use and adequate for many purposes, is not the best method if minimum "grain" and maximum spatial resolution are desired. In these respects, deterministic strategies should be superior. A general design of deterministic plotting strategy is described in the following.

Deterministic interpolation strategy

The strategy considered in this section is based on the requirement that a given spatial average of the transmittances $\bar{t}_i$ of adjacent points in the microfilm transparency correspond as closely as possible to the transmittance of the original picture p_o:

$$\frac{1}{\Sigma \alpha_i} \sum_{i=0}^{K-1} \alpha_i \bar{t}_i \approx p_o \qquad (5)$$

where the α_i are the spatial weighting coefficients ($\alpha_0 = 1$), and K is the number of points over which the spatial average is performed.

Equation (5) is used in a sequential plotting strategy as follows: Points $i = 1, 2, \cdots, K - 1$ have already been plotted and, in addition to the transmittance p_o of the original, those of the microfilm $\bar{t}_i$ for $i = 1, 2, \cdots, K - 1$ are known. Equation (5) is then used to determine $\bar{t}_0$ and the corresponding number of exposures.

Solving (5) for $\tilde{l}_0$ yields

$$\tilde{l}_0 \approx t_0$$

where t_0 is defined by

$$t_0 = p_0 \cdot \Sigma \alpha_i - \sum_{i=1}^{K-1} \alpha_i \tilde{l}_i \qquad (6)$$

The next stage is to find the number of exposures n_0 that give rise to a transmittance equal to t_0. However, this is not, in general, possible because n_0 is limited to integral values. The "best" we can do is pick an integral value for n_0 that is as close as possible to the required value. This value of n_0 is given by

$$n_0 = [N^{t_0} - \tfrac{1}{2}] \qquad (7)$$

The corresponding actual transmittance $\tilde{l}_0$ is [Eq. (2)]

$$\tilde{l}_0 = \log_N (1 + n_0) \qquad (8)$$

After the number of exposures n_0 for $i = 0$ has been found in this manner, and the corresponding $\tilde{l}_0$ calculated with (8), the calculation proceeds to the next point using (6), (7), and (8) over again with the index i diminished by one.

Figure 6 shows a reproduction of a microfilm output obtained in this manner for a choice of weighting coefficients α_i corresponding to a spatial average over nine points in a 3×3 square array, or

$$|\alpha_i| = \begin{matrix} 0.25 & 0.35 & 0.5 \\ 0.35 & 0.5 & 0.7 \\ 0.5 & 0.7 & 1.0 \end{matrix} \qquad (9)$$

The coefficients of (9) were chosen asymmetrically, with the "last" coefficient (lower right) being the largest, to improve stable sequential operation. The expected reduction in graininess, compared with Fig. 4, is easily noticed. A blowup of the area near the lips (Fig. 7) shows a rather interesting "brush technique" employed by the computer in obeying the averaging and quantization rules previously specified.

Application to image restoration

The plotting strategy just described has been used in a variety of image restoration and processing schemes that were simulated on a large digital computer (GE 645). A microfilm plotter, in conjunction with plotting methods for halftone pictures, has resulted in exceedingly rapid turnaround times from the computation center.

Figure 8 is a photograph obtained from the original

FIGURE 6 (above). Reproduction of Fig. 1 using deterministic interpolation strategy. Obtained by the same microfilm plotter used for Fig. 2, the halftones are realized by a special program (software) that makes local spatial averages of the brightness values in the replica equal to the brightness values of corresponding points in the original.

FIGURE 7 (right). Blowup of lip area of Fig. 6, revealing an interesting "brushstroke" technique resulting from the spatial averaging rule written into the computer program for approximating halftones.

(Fig. 1) by linear-motion blur. (The direction of the blur is horizontal and the blurring distance corresponds to one eighth of the total width of the picture.)

A respectable replica (Fig. 9) of the original was reconstructed from the blurred image by a method described elsewhere.[1] Only the blurred image of Fig. 8 was used in the reconstruction process.

Application to number theory

Graphic representation can be an important tool in the understanding of complex phenomena. Hidden structures can often be brought out by appropriate graphic display, even in areas of research and human activity that are not primarily thought of as graphic in nature. An example of graphic representation in number theory is illustrated in Figs. 10 and 11.

Figure 10 represents the number-theoretic function defined by

$f(x, y) = 1$ if x and y are relatively prime

$f(x, y) = 0$ if x and y have a common divisor greater than one

The abscissa in Fig. 10 corresponds to x in the range 1 to 256; and the ordinate to y in the same range. The function $f(x, y)$ was processed on a digital computer and Fig. 10 was obtained from a microfilm plotter in the customary (binary) mode of either plotting or not plotting a point, depending on whether coordinates are relatively prime or not.

The fraction of points plotted (about 60 percent) is fairly independent of x and y and corresponds closely to the asymptotic density of relative prime pairs given by $6/\pi^2 = 0.608 \cdots$ (the reciprocal of Riemann's ζ-function of argument 2).

Upon close inspection, Fig. 10 reveals many interesting geometric patterns, some of which represent well-known number-theoretic theorems and are easily understood. Many of the patterns and structures visible in Fig. 10 have no simple theoretical correlates, however.

Another interesting insight into the distribution of relative prime pairs, especially periodic straight-line patterns, is afforded by a two-dimensional Fourier transform of the function $f(x, y)$ as already defined. Figure 11 shows the spectrum (magnitude of the Fourier transform) of the function with the origin at the center of the picture. Multiple exposure was used to represent different values of the spectrum.*

As expected, the spectrum of the relative prime pairs is symmetric about the two 45-degree diagonals. In

FIGURE 8. Blurred photograph obtained by linear-motion blur from the original photograph (Fig. 1).

FIGURE 9. Computer-reconstructed image using only information contained in the blurred image of Fig. 8. The computer first determines direction (horizontal) and extent (one eighth of picture width) of blur and then reconstructs an approximation to the original.

FIGURE 10. The plane of integers x from 1 to 256 and y from 1 to 256. A point is plotted if its two coordinates x and y are relative primes, i.e., if they have no common divisor. This example, using a digital computer and microfilm plotter to "view" number-theoretic relationships, shows the intriguing combination of regularity and randomness that characterizes the distribution of prime numbers and the property of joint divisibility.
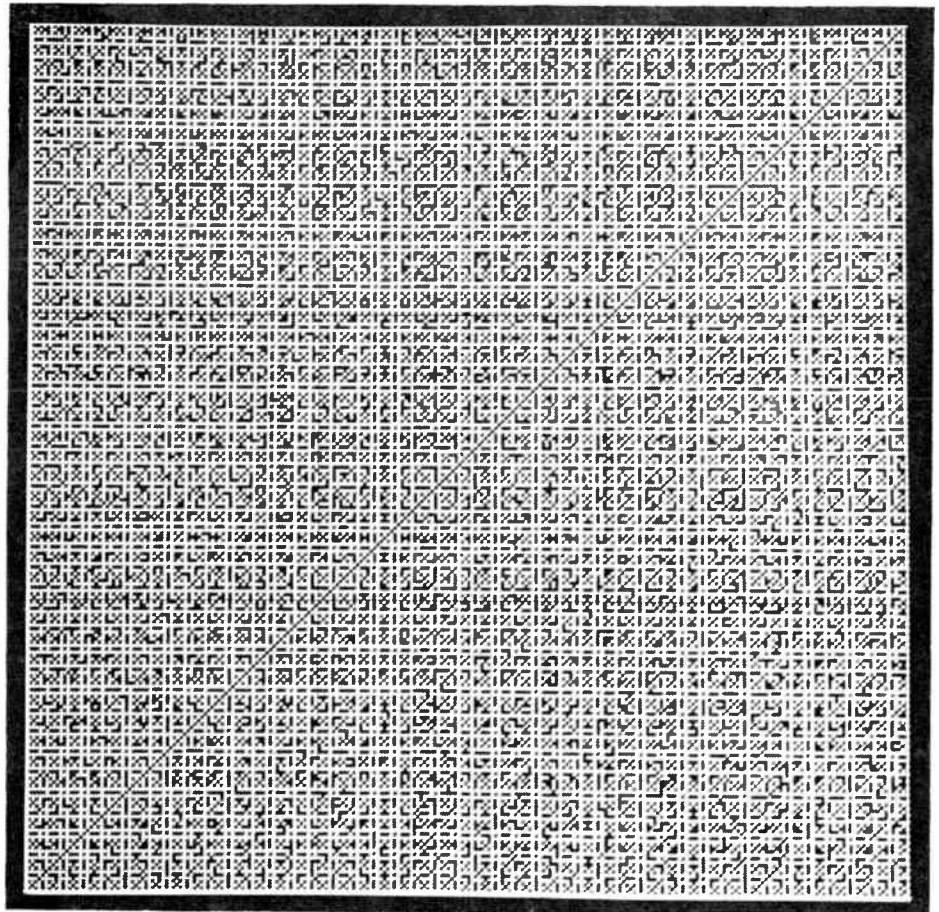
FIGURE 11. The "spectrum" (magnitude of the Fourier transform) of relative primes. If there are periodic regularities in the distribution of relative primes, then these should become visible in the spectrum. The "stars" in this figure, as well as many other patterns—some explainable, others not—show that such periodicities indeed do exist. Here is a fascinating new way of looking at numbers and perhaps discovering new relationships among them.

72
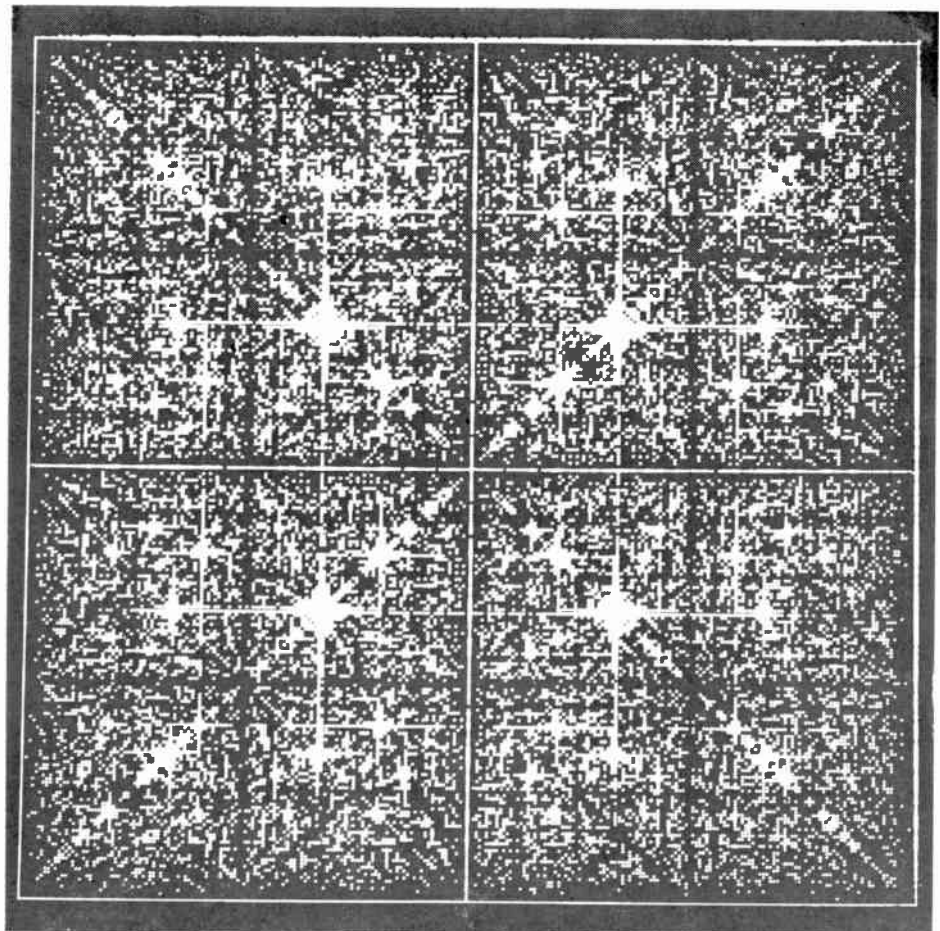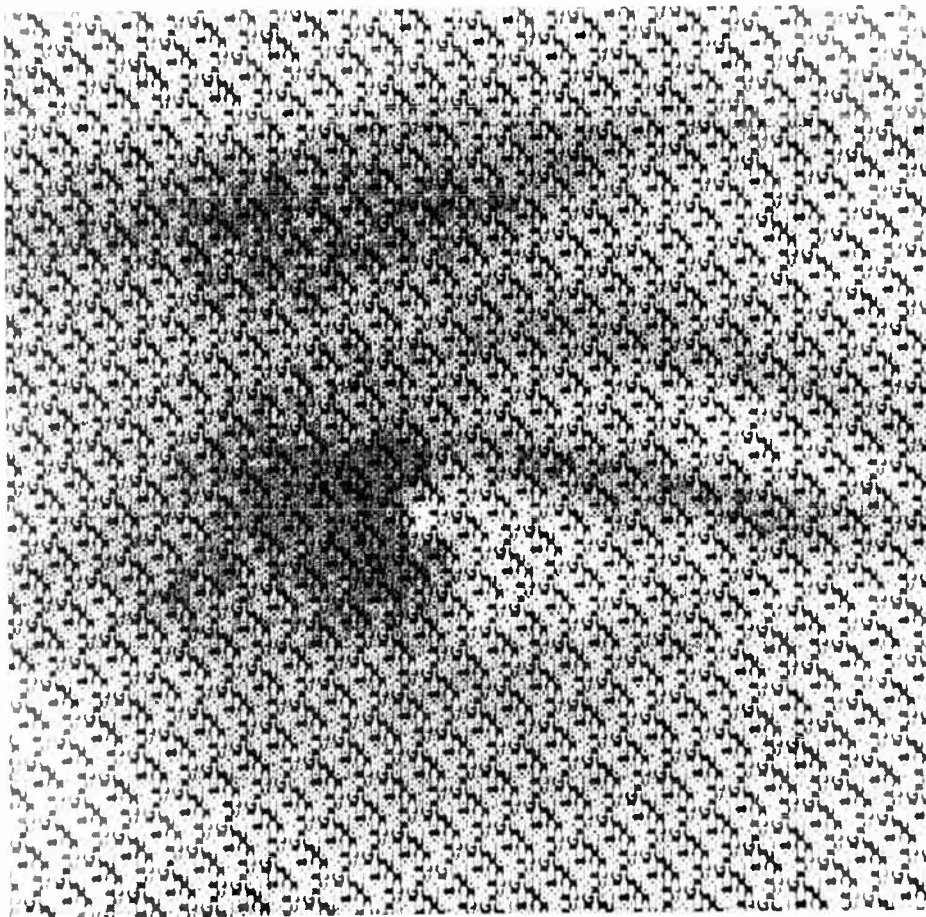
FIGURE 12. "Wordy eye" —a human eye (the left eye from Fig. 1) composed of individual letters and spaces forming the English sentence "One picture is worth a thousand words" repeated over and over again. Four kinds of information or patterns are visible: (1) the individual letters, (2) the words and sentences, (3) the periodic design pattern resulting from the repetition of the sentence, and (4) the eye.

addition, the spectrum can be seen to be approximately symmetric about the abscissa and ordinate. The prominent "stars" in Fig. 11 reflect periodicities in the distribution of relative prime pairs, which, though present, are barely visible in Fig. 10.

Gray scale representations

"One picture is worth a thousand words" is an ancient Chinese proverb. Nevertheless, the information content in a picture can be enhanced by combining it with text or other symbolic information. The microfilm plotter, in conjunction with one of the plotting strategies described, opens up rather astonishing possibilities in this direction. For example, if letters or symbols, instead of small luminous points, are used in producing the halftone picture, text or symbolic information can be superimposed on the pictorial information.

This is depicted in Fig. 12, which represents a small area corresponding to 128 by 128 sampling points surrounding the left eye of the photograph of Fig. 1. Each of the 16 384 picture points in Fig. 12 is represented by a single letter or space from the quotation at the beginning of this section repeated over and over again. Each letter is exposed from one to forty times in accordance with the probabilistic strategy that has already been described.

It is conceivable that this method of combining text with pictorial information, presently just a curiosity, will find useful applications in information display or perhaps even disguise.

Line-width modulation

In addition to multiple exposure of points, letters, and symbols, other processes have been explored to obtain halftone images from microfilm plotters under digital computer control. Some of these processes only simulate halftones by modulating the size of "white" areas on a "black" background in accordance with the graphical information to be presented. Such processes lead to halftone perception only when viewed from a sufficiently large distance away. An example of this technique can be seen in Fig. 13, a reproduction of a microfilm output showing concentric circles whose width has been modulated in such a way that the white areas of small segments of the circles correspond to the transmittance of the desired image (of Fig. 1) in the same neighborhood.

Figure 13 was obtained as follows: In order to produce concentric circles of *constant* relative width w, the microfilm plotter is instructed to plot a point with coordinates x_i, y_i if the following inequality holds:

$$0 \leq c \sqrt{x_i^2 + y_i^2} - [c \sqrt{x_i^2 + y_i^2}] < w \qquad (10)$$

where the brackets, as before, signify the largest integer not exceeding the value inside the brackets. The constant c determines the combined width of a pair of adjacent white and black circles. If w is replaced by a function p_i of x_i and y_i ($0 \leq p_i \leq 1$), then the line width of the white circle at x_i, y_i will be proportional to this function. For Fig. 13, the values of p_i were chosen from the photograph of Fig. 1 and c was made equal to $1/10$, resulting
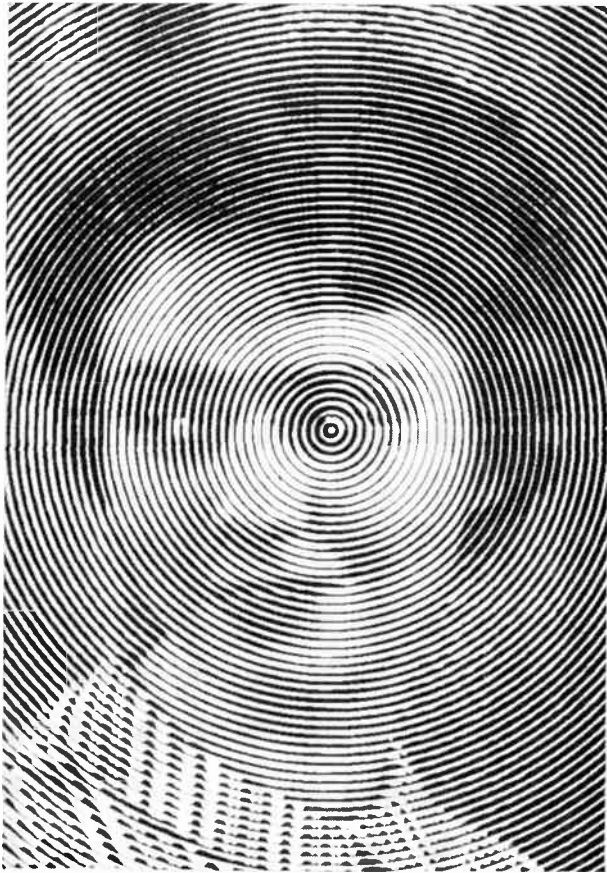
FIGURE 13. "Circles around eye"—simulation of half-tones by "area modulation." This picture combines two kinds of information—connectivity (the circles) and black–white area ratio (the portrait). Viewed from a short distance, the circles are more apparent; from afar (or by defocused projection), the portrait prevails.

FIGURE 14. Moiré pattern obtained from a program for plotting narrow concentric circles. Because of the discrete point grid of the microfilm plotter, a spatial beat, or moiré, pattern is seen instead.
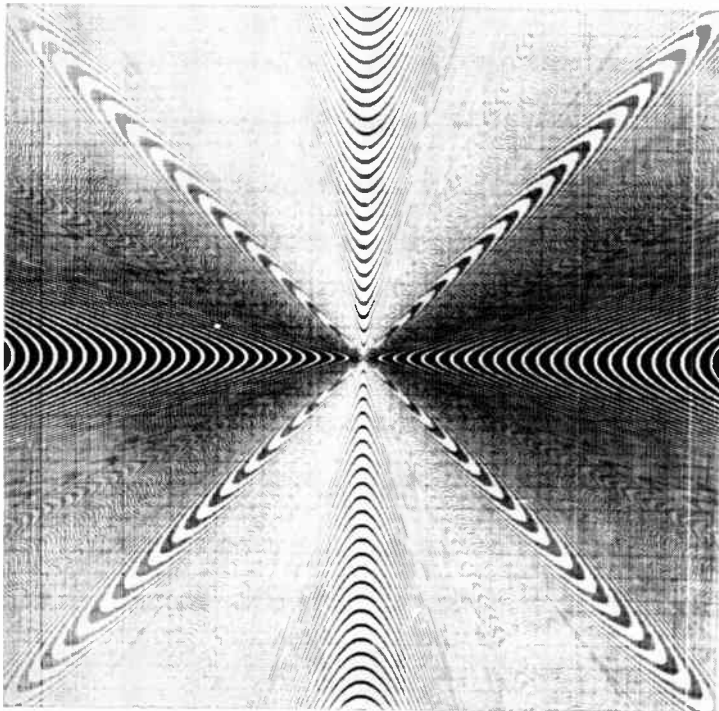
in a total of approximately 50 complete circles of variable width in the square area defined by $-512 \leq x_i \leq 512$ and $-512 \leq y_i \leq 512$.

Moiré patterns

If a larger value is chosen for the constant c, the number of circles will increase to a point where, instead of concentric circles, the moiré pattern for a superposition of concentric circles and the square grid of the microfilm plotter will appear. This is illustrated in Fig. 14, where the function determining relative line width was made dependent on the polar angle ϕ_i, as indicated in the following equation:

$$p_i = \tfrac{1}{4} + \tfrac{1}{2}\cdot\sin^2 \phi_i$$

or, in terms of Cartesian coordinates,

$$p_i = \frac{1}{4} + \frac{1}{2}\cdot\frac{y_i^2}{x_i^2 + y_i^2} \qquad (11)$$

The *intended* lines (concentric circles) are no longer visible, but the width modulation is still reflected in the lower brightness of the moiré pattern along the abscissa ($y_i = 0$) compared with the ordinate ($x_i = 0$). In fact, the picture generated by Eqs. (10) and (11) resembles its own negative after rotation by 90 degrees. This follows from the fact that the complement of p_i,

$$1 - p_i = \frac{1}{2} + \frac{1}{2}\cdot\frac{x_i^2}{x_i^2 + y_i^2} \qquad (11a)$$

is equal to an expression that results from (11) after interchanging x and y.

Contour maps

Instead of concentric circles, many other patterns are suitable for line-width modulation. In particular, width modulation can be applied to *contour lines* (connecting points of equal values of brightness, intensity, etc.). In this method, the information contained in a two-dimensional pattern or a function of two variables can be portrayed graphically in two different ways: (1) as isograms, and (2) as area ratios of "white" to "black."

Although this may often be an efficient way of conveying information, there are instances when this mode of representation leads to rather uncommon displays, such as that shown in Fig. 15, which was derived from Fig. 1 by a rather simple computer program. The computer was programmed to cause the microfilm plotter to plot a point with coordinates x_i, y_i if the corresponding transmittance p_i obeyed the following inequality:

$$0 \leq 8p_i - [8p_i] < p_i \qquad (12)$$

where, again, the brackets indicate the largest integer not exceeding its contents.

It is easily seen that if $8p_i$ is equal to an integer, then $8p_i - [8p_i] = 0$ and the corresponding point will be plotted. If $8p_i$ is just a little smaller than an integer, the point will not be plotted. Thus, the left half of the inequality generates contours, represented by a black–white boundary, corresponding to constant values of p_i, namely, $p_i = n/8$ with $n = 0, 1, \cdots, 7$; and the right half of the inequality determines how wide the white contours are. If the factor 8 is replaced by a larger constant, more contours will be generated, resulting in a more recognizable replica of the original photograph.

Generalized moiré patterns

Moiré patterns result from the spatial interference or "beats" between two or more superimposed geometrical patterns with nearly equal spatial frequencies in the superimposed areas. In addition to their practical usefulness,[a] many moirés have considerable esthetic appeal probably resulting from their peculiar combination of high symmetry, a certain degree of regularity, and a strong element of chance. In Fig. 14, for example, the horizontal, vertical, and 45-degree diagonal directions display perfect periodic structure, whereas in-between directions show less pronounced periodicities.

Are the geometrical patterns usually seen in moirés the limit of what spatial interference can produce, or can one generate *arbitrary* patterns in this fashion? The answer to this question is astounding. With the help of computers and microfilm plotters it is possible to construct two images showing, to the naked eye, two arbitrarily chosen scenes with a microstructure (invisible) such that upon optical superposition a third, arbitrarily specified, image will result. The principle involved is quite simple, but takes the precision of digital computers and the high resolution and registration of modern microfilm plotters to translate the principle into reality.

Suppose the brightness values of individual samples (dots) of the two original images are designated by a_i and b_i, respectively ($0 \leq a_i \leq 1$, $0 \leq b_i \leq 1$). The image desired from the superposition is characterized by brightness samples c_i. Next, the computer is programmed to produce a first image with a spatial array of sample values composed of 2×2 arrays as follows:

$$a_i' = \begin{matrix} a_i & 0 \\ \epsilon_i & 1 - \epsilon \end{matrix} \qquad (13)$$

where $\epsilon_i = 0$ or 1 chosen in an arbitrary way. If an image composed in this fashion is viewed with a resolution that does not resolve the individual samples in this 2×2 array, then an average brightness in the area occupied by the array will be seen:

$$\overline{a_i'} = \tfrac{1}{4}(1 + a_i) \qquad (14)$$

Thus, except for a limited gray scale ($\tfrac{1}{4} \leq \overline{a_i'} \leq \tfrac{1}{2}$), the first image with samples a_i will be seen. The second image, also 2×2 arrays, is constructed as follows:

$$b_i' = \begin{matrix} 0 & b_i \\ |c_i + \epsilon - 1| & |c_i - \epsilon| \end{matrix} \qquad (15)$$

The four-sample spatial average of b' is

$$\overline{b_i'} = \tfrac{1}{4}(1 + b_i) \qquad (16)$$

independent of c_i and the choice of ϵ_i, which could represent a fourth image or some other information.

Upon superposition, in perfect registry, of the two transparencies composed of arrays a_i' and b_i', respectively, an image composed of the point-by-point *product* of a_i' and b_i' will result. If $\epsilon_i = 0$, the result is

$$a_i' \cdot b_i' = \begin{matrix} 0 & 0 \\ 0 & c_i \end{matrix} \qquad (17)$$

If $\epsilon_i = 1$, the product is

$$a_i' \cdot b_i' = \begin{matrix} 0 & 0 \\ c_i & 0 \end{matrix} \qquad (18)$$

In either case, the spatial average over the four points of the two superimposed 2×2 arrays is

$$\overline{a_i' \cdot b_i'} = \tfrac{1}{4}c_i \qquad (19)$$

Thus, except for a limitation in the extent of the gray scale and a loss of spatial resolution by a factor of 2, the superposition of two transparencies showing arbitrarily chosen images results in a third freely chosen image. The superposition of a "father" slide (a_i) and a "mother" slide (b_i) brings forth a "child" (c_i). The possibilities stagger the mind.

Can one go even further and produce two transparencies of individual dots with brightness values restricted to 0 and 1, chosen at random with equal probability and independent from point to point, such that their optical superposition will result in an arbitrarily chosen scene? The answer, surprisingly, is yes, if the individual dots are restricted to brightness values 0 or 1. To obtain a recognizable image with an apparent gray scale when viewed with limited resolution, the probabilistic rounding principle presented can be employed.

Suppose one wants to create a scene resembling an image whose individual brightness values are p_i; then

$$\pi_i = [p_i + r_i] \qquad (20)$$

FIGURE 15. "Leprosy"—contour lines connecting points of equal brightness in the original photograph. The width of these lines is modulated to reflect the different brightness levels. Again, as in Fig. 13, two kinds of information are combined—connectivity and black–white area ratio. An example of the bizarre kind of images obtainable on microfilm plotters.

A
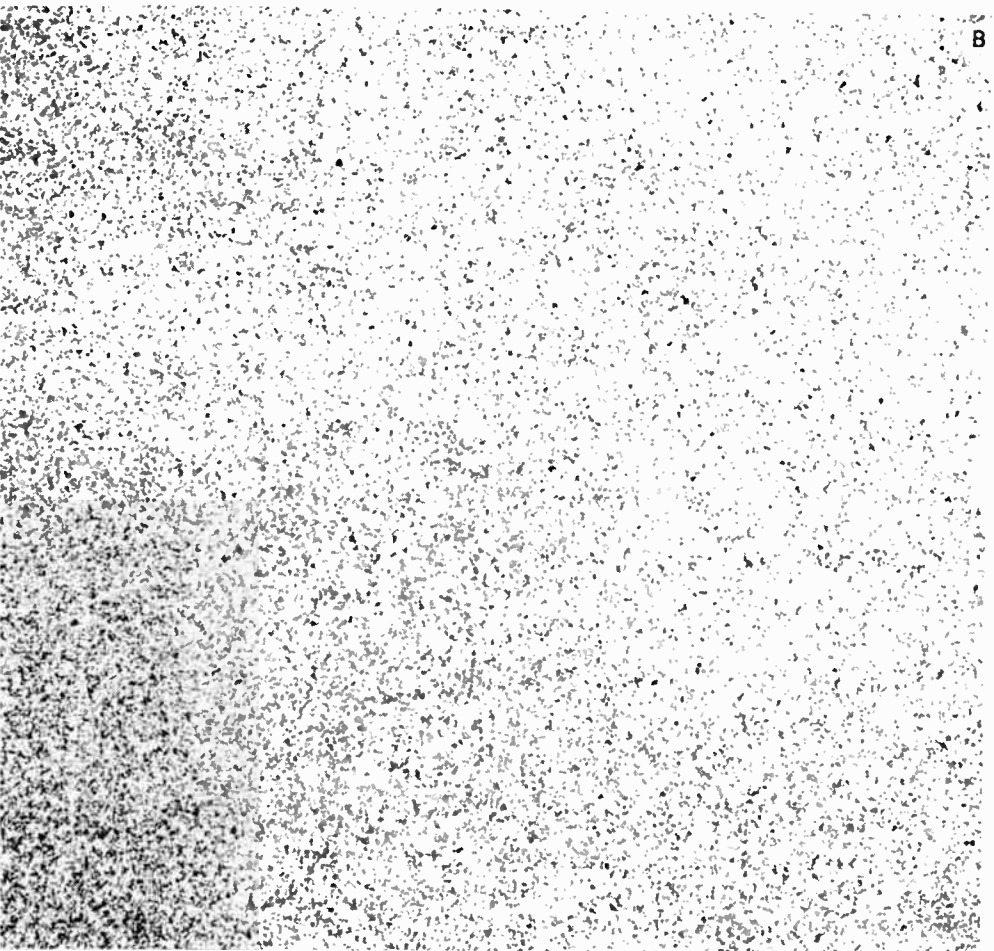
B

FIGURE 16. A—Random picture obtained by quantizing the brightness information in Fig. 1 to two levels (0 = black and 1 = white) and then encrypting the resulting binary representation by adding (mod 2) a binary random key. The result is the "encrypted" picture shown. B—The random "key" used in obtaining Fig. 16(A). C—Photograph of the superposition of two transparencies corresponding to Figs. 16(A) and (B), the "deciphered" quantized original.

where r_i is a random process uniformly distributed in the interval 0 to 1 and independent from point to point. Although $\pi_i = 0$ or 1, its statistical expectation equals p_i. Thus, an image composed of dots with transmittance π_i will resemble the original image p_i with a strong noise component. (Since the noise has a flat spectrum of spatial frequencies, because of the point-by-point independence of r_i, its effect can be reduced by limiting the resolution. This can be done by an out-of-focus projection of the image π_i.)

Now π_i is combined with a *binary* random process σ_i having values 0 or 1 chosen at random with equal probability and independent from point to point:

$$\tilde{\pi}_i = (\pi_i + 1 - \sigma_i)_{\mathrm{mod}\,2} \qquad (21)$$

For $\sigma_i = 1$, $\tilde{\pi}_i = \pi_i$; for $\sigma_i = 0$, $\tilde{\pi}_i = 1 - \pi_i$. In fact, it can be shown that $\{\tilde{\pi}_i\}$ is a stochastic process with the same ensemble properties as $\{\sigma_i\}$, i.e., $\tilde{\pi}_i = 0$ or 1 with equal probability, independent from point to point. However, the optical superposition of $\tilde{\pi}_i$ and σ_i in point-by-point registry results in

$$\tilde{\pi}_i \cdot \sigma_i = \begin{cases} \pi_i & \text{if } \sigma_i = 1 \\ 0 & \text{if } \sigma_i = 0 \end{cases} \qquad (22)$$

Thus, except for a random replacement (with a probability of one half) of samples of π_i by 0 (black dots), the superposition of the two random transparencies $\tilde{\pi}_i$ and σ_i results in the quantized version π_i of the original picture p_i. This is illustrated in Fig. 16. Figure 16(A) shows $\tilde{\pi}_i$ obtained from p_i (from Fig. 1) by Eqs. (20) and (21). Figure 16(B) shows the random "key" σ for unlocking the information buried in Fig. 16(A). Figure 16(C) gives the result of superimposing and photographing transparencies corresponding to Figs. 16(A) and 16(B). The quantized original is thus "deciphered."

Since ordinary microfilm transparencies show an overlap between the images of neighboring points, only every second or third point (both horizontally and vertically) should be used to achieve this remarkable deciphering optical process. Another requirement calls for near-perfect registry between the two transparencies, i.e., the disguised one and the key.

Random walks and programming errors

In preceding sections, the use of random numbers to eliminate unsightly contours in images with quantized brightness levels (Figs. 4 and 5) was discussed. Random numbers can also disguise a scene [Fig. 16(A)] and

uncover it again [Fig. 16(C)]. "Random"-number generating routines, either by themselves or in combination with deterministic processes, can lead to a limitless variety of patterns and images representing physical objects, mathematical abstractions, or pure fantasy.

A well-known physical phenomenon with a random habit, which has attracted the brightest physical minds, is Brownian motion—the random meanderings of grave particles in a hot environment of smaller particles.

Figure 17 illustrates a Brownian motion superimposed on a deterministic drift in diagonal directions. A total of 36 particles are involved starting out as quadruplets from nine random locations and being attracted by four distant force centers. However, because of some programming error, the particles that were supposed to migrate toward the upper right and lower left lost their attractive charge and hovered around their origins—resulting in a woolly looking overexposure of the microfilm.

It is said that some discoveries have been made by accident or miscalculation. Have any new insights been gained by programming error or computer miscalculation? Perhaps! In any case, nonsense calculations can be beautiful if allowed to manifest themselves geometrically. Figure 18 shows an example of a pure programming error. It doesn't look like the expected result—several things in the program (or the machine) must have gone wrong. What went wrong? Why? We never did find out.

FIGURE 17. "Brownian motion," a well-known phenomenon in statistical physics, here superimposed on a deterministic drift (from upper left to lower right). Some of the particles have no drift and hover around their points of origin—resulting in overexposure of the film.

FIGURE 18. An example of programming error.

Figures 6, 7, 10–15, 17, and 18 were copyrighted by Bell Telephone Laboratories, Inc., in 1968.

REFERENCES

1. Sondhi, M. M., and Schroeder, M. R., "Restoration of blurred photographs," J. Opt. Soc. Am. (to be published).
2. Oster, G., and Nishijima, Y., "Moiré patterns," Sci. Am., vol. 208, p. 54, Jan. 1963.

Manfred R. Schroeder (SM) was born in the city of Ahlen, Germany, on July 12, 1926. He received the Diplom Physiker degree (1951) and the Dr. rer. nat. in physics (1954) from the University of Göttingen, coming to the U.S. to join the research staff of Bell Telephone Laboratories at Murray Hill, N.J., immediately after graduation. Dr. Schroeder's work at Bell Labs. has encompassed a variety of phases in the fields of acoustics, engaging him in fundamental studies of architectural acoustics, electroacoustics, underwater sound, speech, and hearing. He is also known for contributions to the communications sciences, for his statistical theory of random-wave fields, and for several new measurement methods in acoustics and other disciplines, and holds numerous patents in these fields. In 1958, Dr. Schroeder was appointed head of the Acoustics Research Department at Bell Labs., and in 1963 he became director of the Acoustics and Speech Research Laboratory. In 1964, he assumed responsibility for all areas of acoustics and ultrasonics research at Bell Labs. as director of the Acoustics, Speech, and Mechanics Research Laboratory. Dr. Schroeder has been active in a number of assignments for the U.S. government, serving on the National Stereophonic Radio Committee, the Joint Committee on Hearing and Bioacoustics of the Armed Forces, and the National Research Council. In 1966, he was appointed to the new technologies panel of the President's National Advisory Commission on Health Manpower. A Fellow and former governor of the Audio Engineering Society and a member of the German Physical Society, Dr. Schroeder is also a Fellow of the Acoustical Society of America, and an associate editor of the Journal of the Acoustical Society of America.

A sinusoidal voltage-controlled oscillator for integrated circuits

Since design parameters are dependent upon passive-component ratios only, this circuit is ideally suited for the loose absolute-value tolerances that are exhibited by the diffused components of ICs

Alan B. Grebene   Signetics Corporation

This article describes an inductorless near-harmonic voltage-controlled oscillator circuit that utilizes a compensated Wien-bridge topology with a voltage-controlled Miller integrator as the tuning element. Suitable for monolithic integrated realization, the VCO offers a two-to-one control range for frequencies up to 10 MHz, with less than a 1-dB amplitude variation and less than a ten percent total harmonic distortion over the entire control range.

Sinusoidal voltage-controlled oscillators (VCOs) offer a wide variety of applications in modern communication systems.[1] They are often utilized as synchronized local oscillators in signal comparators and phase-locked demodulators.[2,3] To be suitable for a broad class of applications in FM signal detection and demodulation, the VCO is required to have a broad frequency tuning range with minimum amplitude variation and harmonic distortion.

This article presents an inductorless sinusoidal VCO design for phase-locked demodulator applications that closely fulfills these basic performance requirements, and that is well suited for monolithic integration. The VCO circuit is derived from the basic Wien-bridge topology, a simplified diagram of which is shown in Fig. 1. This configuration is chosen for the VCO synthesis because the Wien-bridge circuit, with the possible exception of a positive-impedance inverter topology,[1] requires the lowest stable forward gain for sustained oscillations. For nearly sinusoidal operation, the natural frequencies of the Wien-bridge oscillator can be written as the roots of the characteristics polynomial:

$$p^2 + p\left(\frac{R_a C_a + R_b C_b + (1 - \alpha)R_a C_b}{R_a R_b C_a C_b}\right) + \frac{1}{R_a R_b C_a C_b} \tag{1}$$

where $p = j\omega$ is the complex frequency variable.

Nearly sinusoidal oscillations can be obtained by setting the amplifier forward gain α equal to the critical loop gain α_0, where

$$\alpha_0 = 1 + \frac{C_a}{C_b} + \frac{R_b}{R_a} \tag{2}$$

This corresponds to a frequency of oscillations f_o that is given as

$$f_o = \frac{1}{2\pi} \frac{1}{\sqrt{R_a R_b C_a C_b}} \tag{3}$$

The input capacitance C_a is chosen as the voltage-
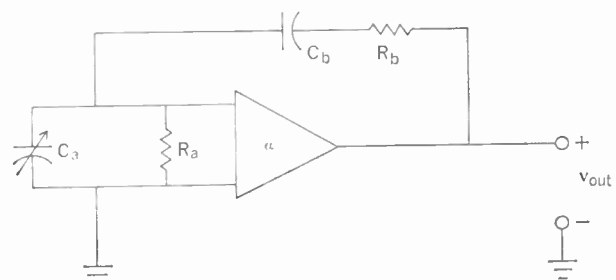
FIGURE 1. Basic Wien-bridge oscillator topology.
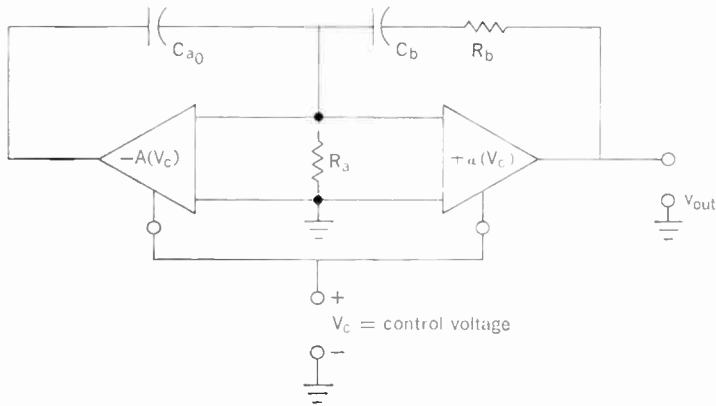
FIGURE 2. Block diagram of the compensated Wien-bridge voltage-controlled oscillator.
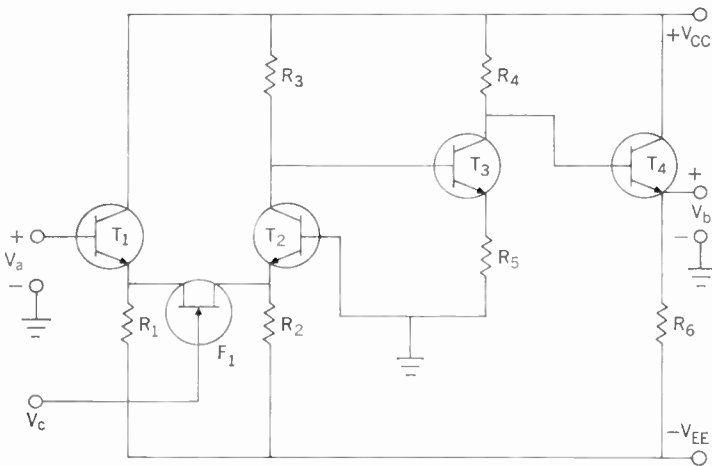
FIGURE 3. Voltage-controlled gain block for the Miller multiplier circuit.
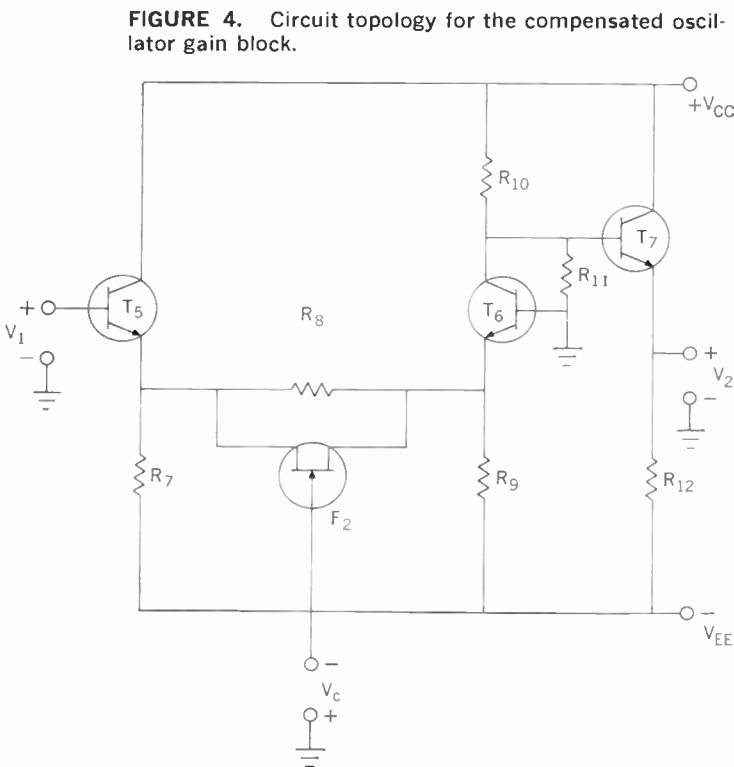
FIGURE 4. Circuit topology for the compensated oscillator gain block.

dependent control element for the VCO. In order to realize the desired wide control range with minimum control voltage, the variable capacitance C_a is obtained by applying capacitive Miller feedback around an inverting gain block of voltage gain $-A$, as shown in Fig. 2. The effective value of C_a can be expressed as

$$C_a = C_{a_0}(1 + A) \tag{4}$$

where the gain A is, in turn, a function of the dc control voltage, V_c.

As indicated by Eq. (2), the critical gain of the oscillator gain block for nearly sinusoidal oscillation is a function of the capacitor C_a. Substituting Eq. (4) into Eq. (2), it can be shown that the critical loop gain α_0 is a monotonically increasing function of A:

$$\alpha_0 = \frac{C_{a_0}}{C_b}(1 + A) + \frac{R_b}{R_a} + 1 \tag{5}$$

Therefore, in order to sustain near-sinusoidal oscillations without excessive amplitude variation or harmonic distortion, it is necessary to vary α and A simultaneously to satisfy the critical gain requirement of Eq. (5).

Circuit design

The voltage-controlled inverting gain block used in simulating the variable capacitor C_a can be realized in terms of the circuit topology of Fig. 3. In this circuit, the transistor T_1 serves as a high-input-impedance buffer stage. The field-effect transistor (FET) F_1 provides voltage-controlled resistive coupling[5] between T_1 and T_2. Along with the inverter stage T_3, T_2 provides the necessary voltage amplification. The transistor T_4 serves as an output buffer stage, providing a low-impedance output. The control voltage is applied to the gate terminal of F_1, thus controlling its source-drain resistance. Owing to the balanced nature of the circuit, F_1 has a zero dc bias across it. The ac gain of the circuit can be expressed as

$$\frac{V_b}{V_a} = -A = -\frac{R_3 R_4}{R_{sd} R_5} \tag{6}$$

where R_{sd} is the FET source-drain resistance and a function of the control voltage, V_c. The circuit offers a wide bandwidth, with a dominant pole p_1 located at

$$p_1 \simeq -\frac{1}{2C_c R_3} \tag{7}$$

where C_c is the collector-base capacitance of the bipolar transistors. For practical values of R_3 and C_c, p_1 is located far outside the frequency range of interest.

The oscillator gain block is synthesized utilizing the circuit topology of Fig. 4. Transistors T_5 and T_7 serve as buffer stages, providing high input and low output impedances for the gain block. The FET F_2 is utilized in the same manner, and under identical bias conditions, as F_1 of Fig. 3. Assuming the F_1 and F_2 have identical geometries, the voltage gain α of the oscillator block can be written as

$$\alpha \simeq \frac{R_L}{R_9}\left(1 + \frac{R_8}{R_{sd}}\right) \tag{8}$$

where R_L is the shunt combination of R_{10} and R_{11}. The net phase shift within the oscillator gain block can be minimized by locating the dominant pole p_2 of the α

block outside the frequency range of interest, where

$$p_2 \simeq -\frac{1}{2C_r R_L} \qquad (9)$$

Comparing Eqs. (6) and (8), one can relate α to A as

$$\alpha = \frac{R_L}{R_s}\left(1 + \frac{R_s R_2}{R_3 R_4}A\right) \qquad (10)$$

From Eqs. (5) and (10), it can be shown that, to a first order, the critical loop gain α_0 can be made independent of A by choosing

$$\frac{C_{a_0}}{C_b} = \frac{R_L R_3}{R_3 R_4} \qquad (11)$$

The corresponding value of the critical loop gain then becomes:

$$\alpha_0 = \frac{C_{a_0}}{C_b} + \frac{R_b}{R_a} + 1 = \frac{R_L}{R_s} \qquad (12)$$

In the actual synthesis, however, R_s must be chosen slightly smaller than that implied by Eq. (12) to make up for the parasitic losses in the circuit (such as the non-unity gain of buffer stages).

Figure 5 displays the complete circuit diagram for the VCO. As long as the FETs F_1 and F_2 are well matched, and the passive component values are chosen to satisfy Eq. (11), the oscillator loop gain and the output waveform become independent of the control voltage V_c. It should be noted that the equality of Eq. (11) depends only on the passive-component ratios, and not on the absolute values. This makes the gain-compensated Wien-bridge circuit of Fig. 5 ideally suited for integrated realization using diffused components with relatively loose absolute-value tolerances. Furthermore, junction or insulated-gate FETs of either conductivity type can be used as the gain control device.

Since R_{sd} does not appear in Eq. (11), the circuit compensation does not depend on the absolute values of the FET parameters. The form of the control-voltage versus frequency characteristics, however, depends on the value of the FET pinch-off voltage, V_p. For a uniformly doped channel junction-gate FET structure, the frequency of oscillation f_o can be related to the control voltage as

$$f_o = \frac{f_1}{\sqrt{1 + \frac{R_3}{R_0}\left(1 - \sqrt{\frac{V_c + \phi}{V_p}}\right)}} \qquad (13)$$

where f_1 is the maximum frequency of oscillation corresponding to $R_{sd} = \infty$, R_0 is the value of R_{sd} for zero applied gate bias, and ϕ is the base-emitter voltage drop of the n-p-n bipolar transistors adjacent to F_1 and F_2 in Fig. 5.

Experimental results

The performance evaluation of the VCO circuit of Fig. 5 was carried out using diffused resistors and compatible monolithic n-p-n bipolar and n-channel epitaxial FETs. The experimental results indicate that the circuit is capable of operating up to 10 MHz with a control range f_{max}/f_{min} of $\geq 2 : 1$. The circuit prototype was evaluated with the following component values:

$$R_1 = R_2 = R_6 = R_7 = R_9 = R_{10} = R_{12} = 5\ k\Omega$$

$$R_4 = R_5 = 2\ k\Omega \qquad R_3 = 3\ k\Omega$$

FIGURE 5. Circuit diagram of the VCO.
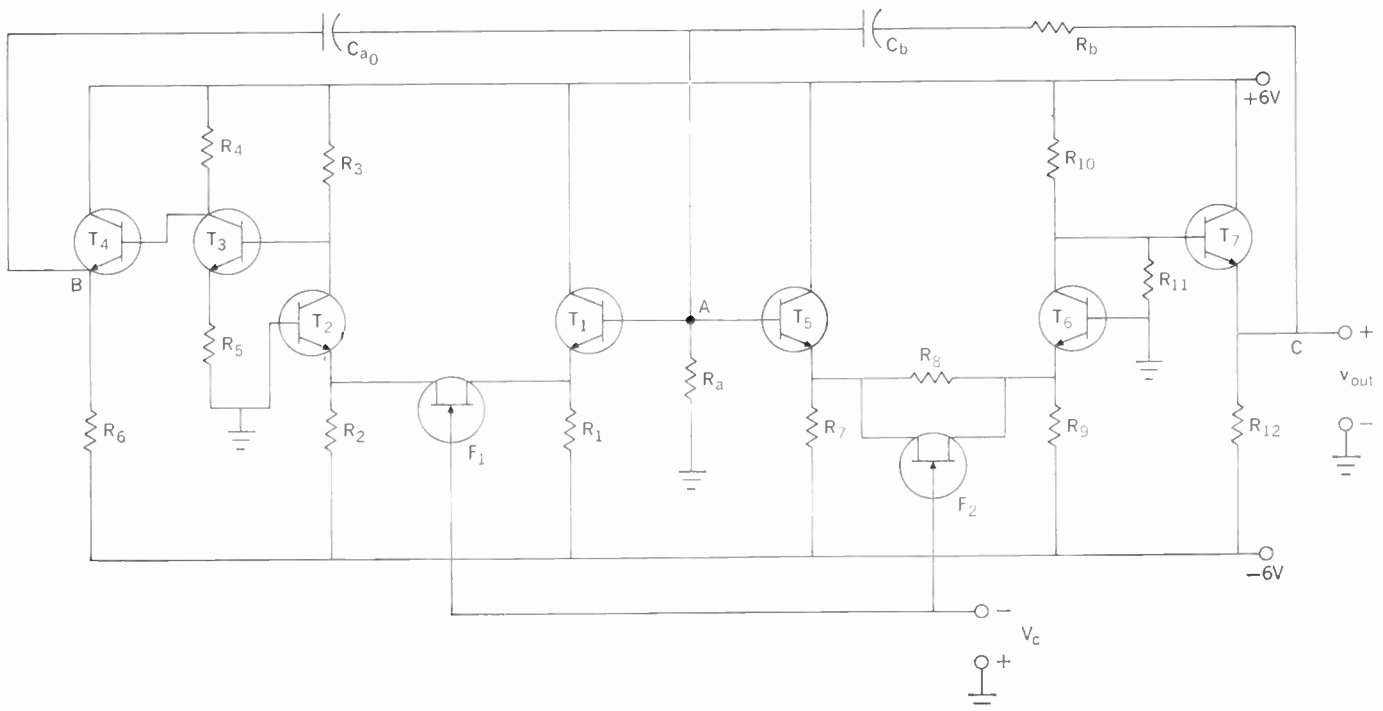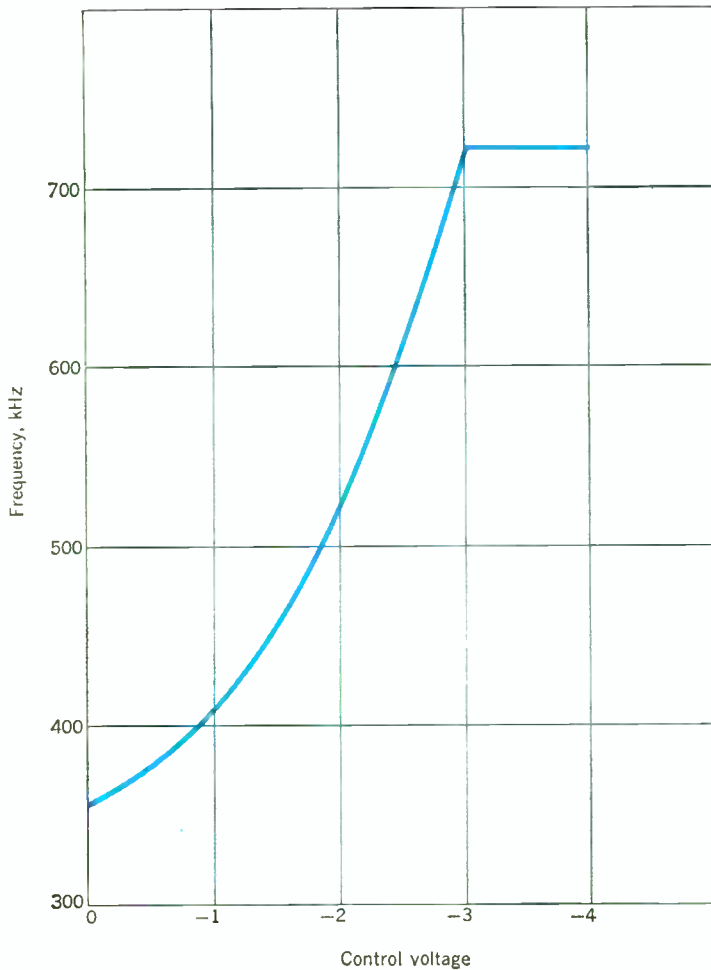
FIGURE 6. Typical control characteristics for the VCO.

FIGURE 7. Typical temperature drift characteristics of the VCO within the control range.
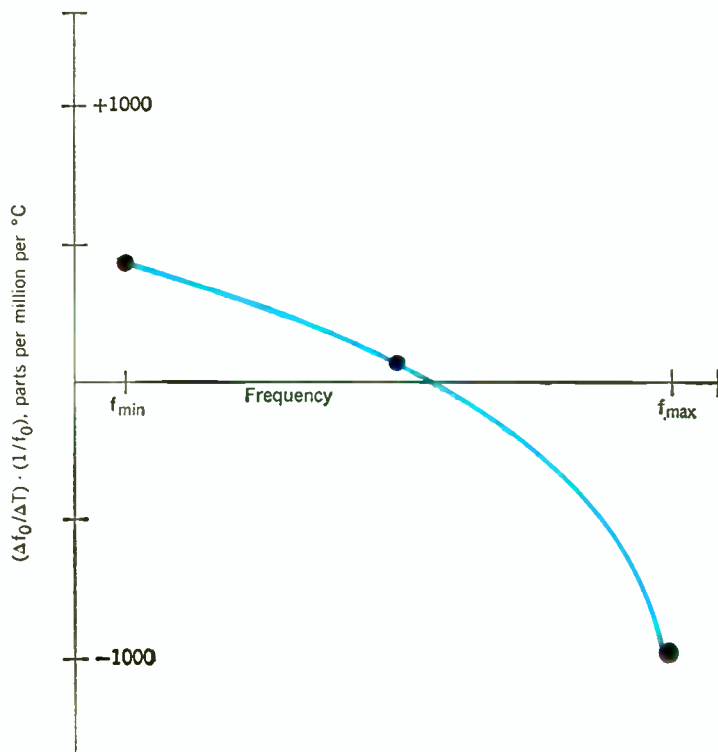
$$R_s = 250 \ \Omega \qquad R_{11} = 1.5 \ \text{k}\Omega$$

$$R_a = 2 \ \text{k}\Omega \qquad C_{a_o} = 30 \ \text{pF}$$

$$R_b = 7 \ \text{k}\Omega \qquad C_b = 100 \ \text{pF}$$

$$V_{CC} = V_{EE} = 6 \ \text{V}$$

The corresponding control characteristics of the circuit, using n-channel epitaxial FETs, are plotted in Fig. 6.

Figure 7 illustrates the average temperature drift characteristics for the VCO over a 0°C to 90°C temperature range as a function of the frequency range of operation, using diffused resistors and silver-mica capacitors. The FET source-drain resistance R_{sd} has a stronger temperature dependence than the base-diffused resistors ($\simeq +4000$ ppm/°C vs. $\simeq +1000$ ppm/°C). Therefore, the voltage-controlled capacitor, C_a, has a negative temperature coefficient that tends to cancel the positive temperature coefficients of R_a, R_b, and C_b. This compensation is particularly dominant at the lower end of the frequency control range, where $A \geq 1$.

Finally, the output waveform of the circuit is first-order insensitive to the control voltage, displaying an amplitude variation of less than 1 dB and a total harmonic distortion of less than 10 percent over the entire tuning range.

REFERENCES

1. Klapper, J., and Acampora, A., "Improved communications techniques," Tech. Rept. AFAL-TR-66-20, Radio Corporation of America, June 1966.

2. Howard, W. G., and Pederson, D. O., "Integrated voltage-controlled oscillators," NEC Proc., pp. 279–284, Oct. 1967.

3. Moschytz, G. S., "Miniaturized RC filters using phase-locked loop," Bell System Tech. J., vol. 44, pp. 823–870, May 1965.

4. Rigby, G. A., and Lampard, D. G., "Integrated selective amplifiers for RF," presented at Internat'l Solid-State Circuits Conf., Philadelphia. Pa., Feb. 1968.

5. Grebene, A. B., and Pepper, R. S., "A wide-band AGC block suitable for integrated realization," presented at Internat'l Solid-State Circuits Conf., Philadelphia, Pa., Feb. 1965.

Alan B. Grebene (M) was born in Istanbul, Turkey, in 1939. He obtained the B.S.E.E. degree from Robert College, Istanbul, in 1961, the M.S.E.E. degree from the University of California at Berkeley in 1963, and the Ph.D. degree from Rensselaer Polytechnic Institute, Troy, N. Y., in 1968. During 1963 and 1964, he was employed as an integrated-circuit research engineer at Fairchild Semiconductor Research and Development Laboratories in Palo Alto, Calif.; and, from 1964 through 1965, he served on the technical staff of the Sprague Electric Company's Micro-electronics Division in North Adams, Mass. Dr. Grebene was a member of the electrical engineering faculty at R.P.I. from 1965 to 1968. He is presently a senior member of the technical staff at the Signetics Corporation, Sunnyvale, Calif., where he is involved in the design and development of linear integrated circuits for communication systems. Dr. Grebene has authored a number of papers and holds several U. S. patents in the fields of solid-state devices and integrated circuits. He is a member of Sigma Xi, Eta Kappa Nu, the American Society for the Advancement of Science, and the American Society for Engineering Education.

The economical fuel cell

One of the first applications of economically competitive fuel cells will be as a battery charger, either for replenishing discharge cells or for use with conventional secondary batteries in hybrid configurations

Galen R. Frysinger   U.S. Army Electronics Command

Most of today's development work in fuel cells is geared to the specific adaptation of these energy sources to user requirements. For powering lightweight portable equipment, the fuel cell–battery hybrid system has been found to be extremely useful and versatile. A minimum number of fuel cell and battery components can service a wide range of equipment at low development costs.

Fuel cells, for the first time, are becoming sufficiently simple, reliable, and low in cost to be considered for a wide variety of practical applications. The determination of their feasibility for a given application requires careful study. Both the initial cost of the fuel cell power source and its operating cost relative to output must be taken into consideration.

It is virtually impossible for fuel cells to compete economically with central station power, or even with diesel auxiliary power equipment, for general-purpose uses. There are, however, many present cases in which a high price per kilowatthour is willingly paid for usable electric energy in order to gain other advantages. Energy for lightweight portable equipment, for example, is purchased at a premium price. The conventional Leclanche cell costs about $30 per kilowatthour

in the packages of carbon–zinc cells commonly used to power radios, hand lanterns, and other lightweight portable equipment.

Energy sources that were used to power the high-intensity lights used for color television coverage of the 1968 U.S. political conventions had to fulfill the requirement of high portability in mobile man-pack operation. Remote relay stations and weather telemetry stations provide other examples of applications for which direct-energy-conversion devices look most promising.

For most commercial uses secondary batteries, such as the vented or sealed nickel–cadmium alkaline types, are convenient and desirable if economical recharging procedures and power sources are available for energy renewal at the end of a full discharge. Because of existing use patterns for highly mobile and portable electric power, one of the first applications of the economical fuel cell will be as a battery charger, either to replenish discharge cells or to be used with conventional secondary batteries in hybrid configurations. This is a most attractive means for providing electricity in those locations where it is not normally available. Energy can be distributed in easily packaged and transportable form as chemical fuel for fuel cells. Since the total amount of fuel involved is actually very small—

in fact, there is a reduction in both volume and weight compared with carbon–zinc primary batteries of equivalent output—any fuel can be used if it can be successfully packaged for safe storage, safe handling, and safe transfer to the fuel cell in the field. Any fuel is economical if it is less expensive than the equivalent form of electric energy that otherwise would be utilized. Since most fuel cells use hydrogen as the active material for oxidation at the anode, a solid or liquid hydrogen compound is preferable. Lithium hydride is a conveniently supplied solid fuel at a cost competitive with carbon–zinc batteries.

Fuel cells as battery chargers

The fuel cell is becoming sufficiently reliable and simple to be used as a portable power source for communications and surveillance equipment. It is interesting to note that the lightweight fuel cells now being developed are not replacing batteries; instead, they are assisting conventional secondary batteries by providing extended life in special fuel cell–battery hybrid configurations. A favorable combination of virtues stems from the fact that the secondary battery has the power density (watts per unit of weight) and can instantly provide power for the equipment, and the fuel cell portion effectively converts a primary fuel to electric energy at a steady continuous rate to provide a high energy density after its initial warm-up. The attractiveness of this combination of power sources is seen when one analyzes the limitations of traditional batteries used in lightweight communications equipment, as well as the effect that microminiaturization of lightweight man-portable equipment has on the selection of a power source.

The bulk of the electric energy consumed in for-ward-area tactical military communications and surveillance equipment comes from the discharge of primary carbon–zinc batteries. At drain rates of approximately 10 watts or less, these batteries give virtually trouble-free service for periods of about 10 to 20 hours. At the end of the discharge, the battery is discarded and replaced. The present conversion from the carbon–zinc cell to the magnesium cell promises to give an increase in energy density and improved high-temperature-storage capability. The increased energy density often allows twice the period of service from a battery of the same equivalent volume and weight as the conventional carbon–zinc battery; however, no significant increase in power density has been achieved with these magnesium cells.

Microminiaturization of components has greatly reduced the amount of electric power required in the normal radio for equivalent performance. For example, the receive or standby power requirement of a typical radio may be as low as 2 to 3 watts. But since microminiaturization has also allowed the designer to incorporate extended range and improved performance in a very small man-portable package, greatly increased amounts of power are required for transmit periods. A radio may have only a 3-watt standby requirement, but as much as 120 to 150 watts may be needed for transmission.

For applications in which periodic higher peaks of power are required than can be accommodated within the low rate limitations of standard dry batteries, secondary batteries, principally of the vented nickel–cadmium type, must be used. These secondary batteries can supply the large pulses of energy that may be

FIGURE 1. Hybrid power supply for radio set.

Radio set

30-watt fuel cell

Ni-Cd storage battery
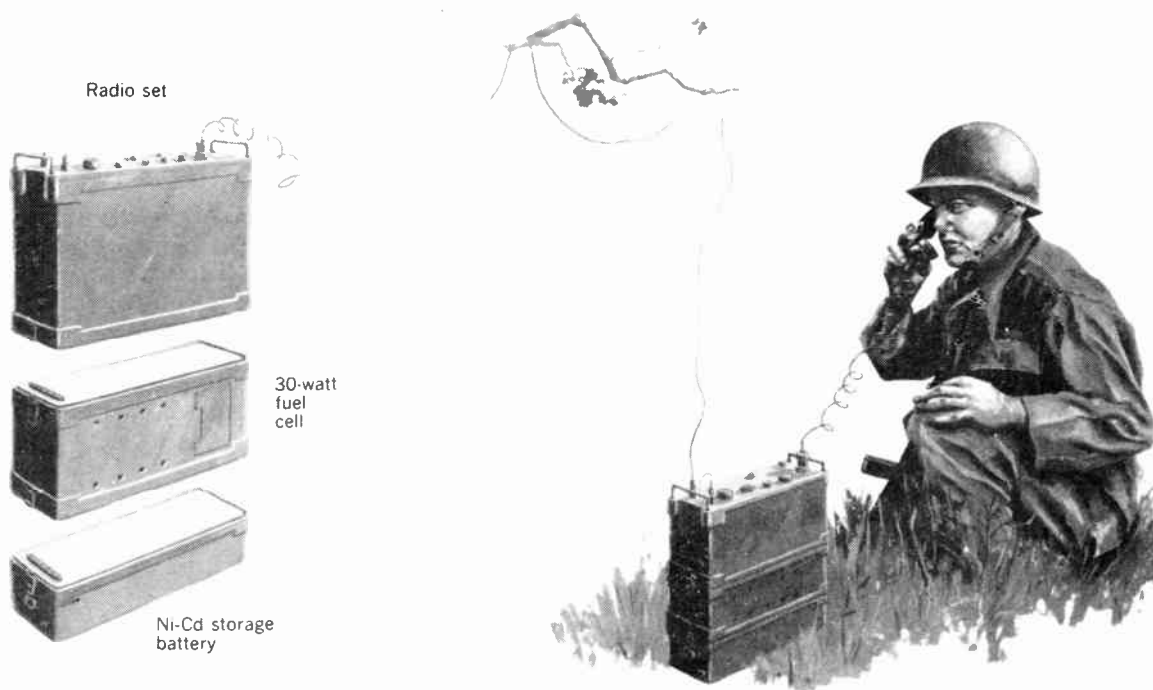
required for several minutes of transmission within well-prescribed voltage limits. The principal difficulty is that in standard military packaging they have energy densities of only approximately 10 watthours per pound (22 Wh/kg). If a total lightweight package is required, their energy content is soon depleted and recharging is necessary.

It is quite evident that the optimum method of renewal for a power source in military communications and surveillance applications should use chemical energy, the source of which can be carried in a disposable container. Whether the energy source involves the traditional package of carbon–zinc cells in a radio battery or a container of fuel for fuel cells makes very little difference. It therefore became apparent that one very attractive application for fuel cells was to use them in combination with a secondary battery, so that the secondary battery provides the peak pulses and the fuel cell efficiently converts the chemical fuel into electric energy at a continuous rate. This scheme combines the attractiveness of a disposable fuel container (yielding several hundred watthours per pound of fuel) with the ability to meet high periodic electric power requirements in an extremely small power-source package. For mobile military operations in which weight reduction is extremely significant, a premium price can be paid for a fuel cell that offers these advantages.

Hybrid power source

The combination of a radio with a 30-watt fuel cell and a nickel–cadmium storage battery is shown in Fig. 1. Drawing power directly from the storage battery, the operator can operate his radio instantly under any type of field condition. This instant-load feature is not inherent in a fuel cell operating alone because it has a start-up lag, resulting from the fact that its normal optimum operating condition is different from the ambient environment in which it is stored. If the operator contemplates continued use of his radio in both the receive and transmit conditions he will activate the fuel cell by providing it fuel from a disposable container and will allow it to provide the power he requires and the power for recharging of the battery automatically after its initial warm-up. The size of the fuel cell and the capacity of the battery must, of course, be properly selected for the equipment to be powered so that full operating performance can be maintained over the total time required and so that the smallest and lightest-weight power-source unit can be assembled. A wide range of communications and surveillance equipment was analyzed to determine the power level that would be most attractive if only one fuel cell were picked to mate with a variety of batteries. The first analysis, which covered a range of highly portable radios, radars, and night-vision equipment, indicated that an average power of 20 to 30 watts was encountered with peaks usually not exceeding 100 to 140 watts during high-intensity power periods. Based on this analysis, a very simple 30-watt fuel cell was designed to work in a hybrid configuration with 12- and 24-volt batteries. A later study indicated that many types of normally vehicular-mounted equipment could also take advantage of this hybrid configuration, but required an average power of 40 to 100 watts, with peaks going as high as 300 to 400 watts

during transmit periods. To meet this requirement a slightly different fuel cell, with improved response and overload characteristics but with increased complexity, was designed.

Chemical-fuel forms

For the 30- and 60-watt fuel cells, the total amount of fuel consumed in 8 to 12 hours is only a fraction of a pound, hence large quantities of fuel are not involved. Actually a reduction in both volume and weight over the equivalent supply of carbon–zinc primary batteries can be achieved. Thus, any fuel that can be successfully packaged so that it can be safely stored, safely handled, and safely transferred to the fuel cell can be utilized in the field. Because of the high cost per kilowatthour of electric power supplied from Leclanche carbon–zinc batteries, almost any type of nonexotic chemical fuel could be cost competitive. The use of gaseous fuels in the field has not been contem-
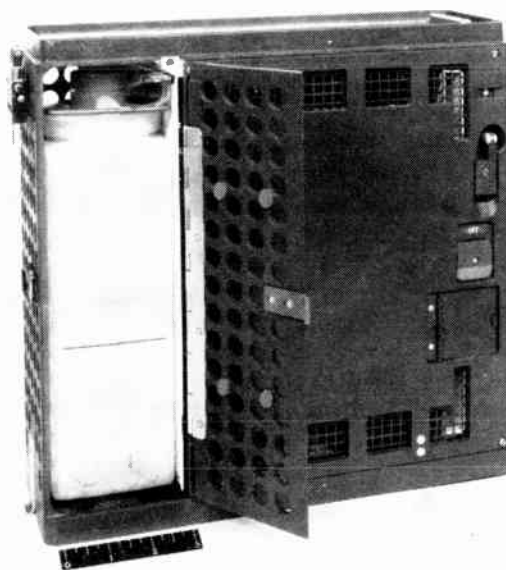
FIGURE 2. Experimental 30-watt metal hydride–air fuel cell for direct mounting to radio set.

FIGURE 3. Typical fuel tablet and hydrogen generator assembly.
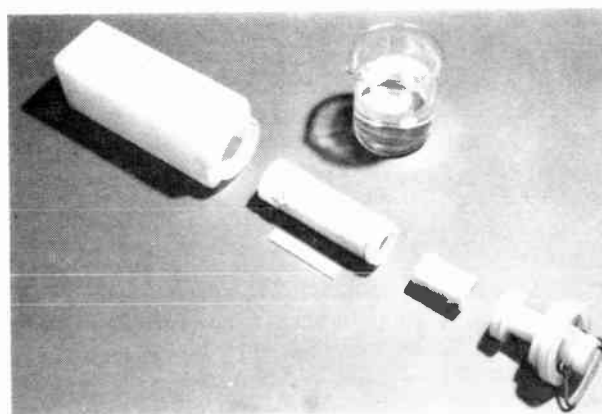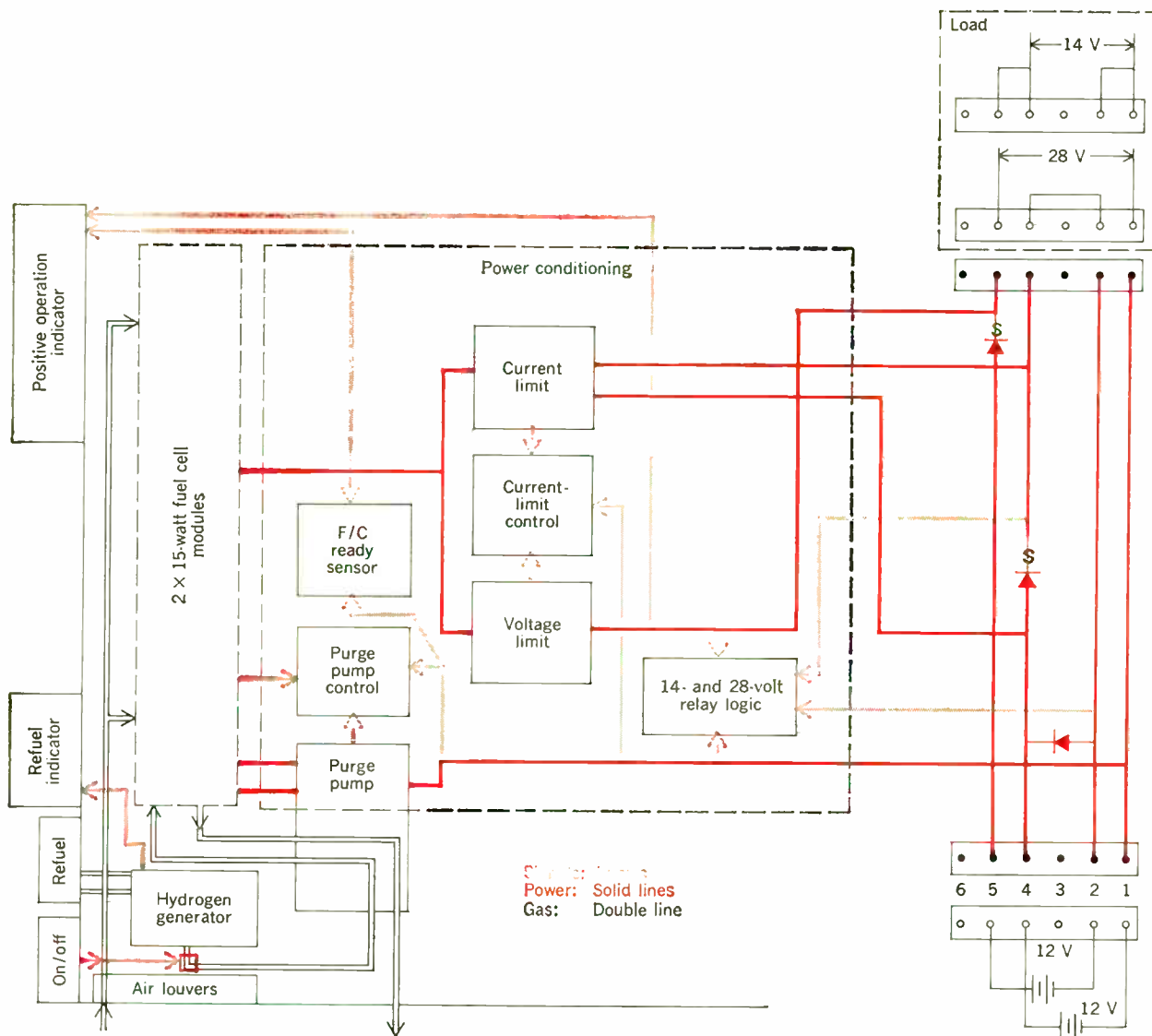
FIGURE 4. Simplified electrical diagram of 30-watt metal hydride–air fuel cell.

plated because of possible safety considerations. Since most fuel cells use hydrogen as the active material for oxidation at the anode, a solid or liquid compound of hydrogen is attractive. A solid compound, either lithium hydride or sodium aluminum hydride, was selected as the fuel for the 30-watt fuel cell. Either hydride can generate active hydrogen for the fuel cell by reaction with water in a system that requires no moving parts. Hydrazine (N_2H_4), a liquid, has been known to be very reactive in fuel cells and is an almost ideal type of fuel for this power range. Although it requires a somewhat complicated system, it was selected for the 60- to 100-watt range because as a soluble fuel in an alkaline electrolyte system it can provide very low impedance and a high overload capability. Approximately 1 kWh/lb (2.2 kWh/kg) is obtained from lithium hydride at a cost of about $10/kWh and 0.35 kWh/lb (0.77 kWh/kg) from hydrazine at a cost of about $3/kWh. In comparison, standard military Leclanche cells provide only about 30 Wh/lb (66 Wh/kg) at a cost of about $44/kWh.

The 30-watt metal hydride–air fuel cell

Figure 2 shows an experimental model of a 30-watt fuel cell packaged in the hybrid configuration compatible with direct mounting to the radio and to the auxiliary secondary battery, as shown in Fig. 1. In the left-hand portion of the fuel cell package is the hydrogen generator, the parts of which are shown in Fig. 3. The cylindrical fuel tablet, weighing about 0.25 lb (0.11 kg), is inserted into the core of the hydrogen generator (center of the photograph), the core is attached to the top closure, and water is added to the outer chamber. The hydrogen generator is then assembled for use.

The fuel cell consists of 14-volt hydrogen–air modules, which can be used in series or parallel to interface with 24- or 12-volt batteries. A simplified electrical diagram is shown in Fig. 4. The single on–off control releases hydrogen to the fuel cell modules and opens the air louvers. A light indicates positive operation and a refill indicator tells the operator when the hydrogen generator must be disassembled for refueling.

FIGURE 5. Nickel-cadmium battery (4.0 ampere-hours, 24 volts) for use with fuel cells in hybrid configurations.

FIGURE 6. Power and voltage curves for fuel cell–battery source supplying load power both for receiving and transmitting purposes.
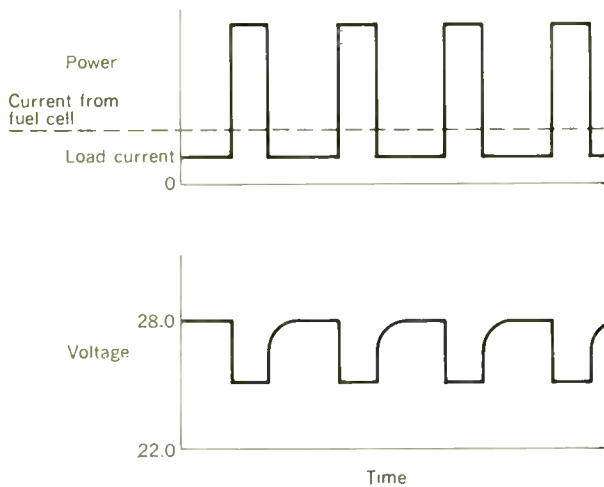
FIGURE 7. Electrical output characteristics of converter/regulator for hydrazine fuel cell.
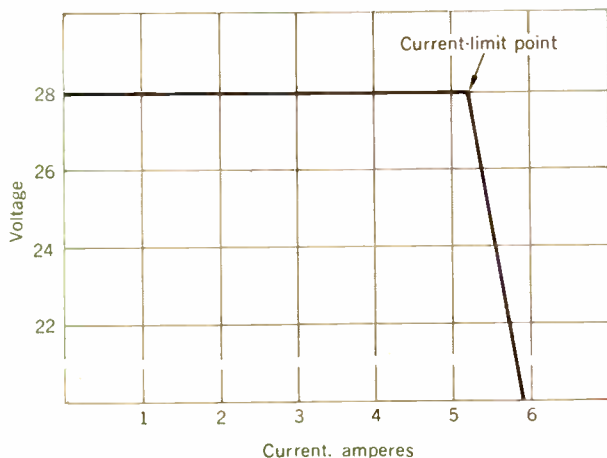
The current-limiting control located in the output circuit allows the fuel cell to be used at a set constant current in recharging the battery during periods when no external load is applied or when the external load is less than the full output of the fuel cell. This current limitation was employed so that sealed as well as vented nickel–cadmium batteries could be utilized without exceeding their continuous overcharge rate. During normal float operation of the battery, recharge rates limited only by the excess power available from the fuel cell could easily be used. However, since the operator has no knowledge of the condition of the battery used in the fuel cell–battery configuration, it is impossible to protect a small sealed battery from possible damage during extended overcharge unless this type of current limitation is employed. A coulometer or other means of charge control could be used to feed information from the battery back to the fuel cell to provide automatic regulation of the amount of the charging current. However, this technique has not been used here, since a prime consideration in the selection of the fuel cell hybrid component is its ability to use any type of standard battery now existing in the system. The fuel cell, therefore, must be compatible with and recharge any of the secondary batteries in the same way as any other external battery charger. Previously the lightest-weight nickel–cadmium battery (24 volts) in the system had a capacity of 5.5 ampere-hours and a weight of 17 lb (7.7 kg). Small, sealed, 24-volt nickel–cadmium batteries of 0.45, 1.2, 1.8, and 4.0 ampere-hours were specifically developed to reduce the weight of this type of hybrid configuration. The 4.0-ampere-hour battery is shown in Fig. 5.

Output characteristics

The use of a hybrid power source for powering electronic equipment is, of course, not new. Electronic equipment mounted on a vehicle may use power from the battery (normally at 24 volts), but it is also capable of being powered at 28 volts dc when the generator or alternator is operating. Since most of the military electronic equipment is designed for vehicular use, it was decided that the fuel cell–battery hybrid should employ the same voltage characteristics. Load-power and source-voltage characteristics for a fuel cell and battery in hybrid operation are shown in Fig. 6. These curves are based on experimental data obtained from a fuel cell producing a steady 60 watts with an alternating load of 30 and 170 watts. Under this harsh duty cycle the fuel cell must be changed if it is to be capable of an overload (100 watts at 25 volts), or the battery will eventually be depleted.

The 30-watt fuel cell, which has an ion-exchange membrane electrolyte, has a high impedance and can provide a highly regulated 28 volts for direct powering of the equipment and for recharging of the battery only by extensive power conditioning, using a voltage limiter. It is therefore not well suited for the type of load in Fig. 6, which would benefit from a fuel cell overload during the peak-load periods. For a higher-output fuel cell utilizing hydrazine as the fuel and an alkaline electrolyte, the inherent regulation of the fuel cell is better, the voltage–current curve being highly regulable by controlling several of the operating varia-
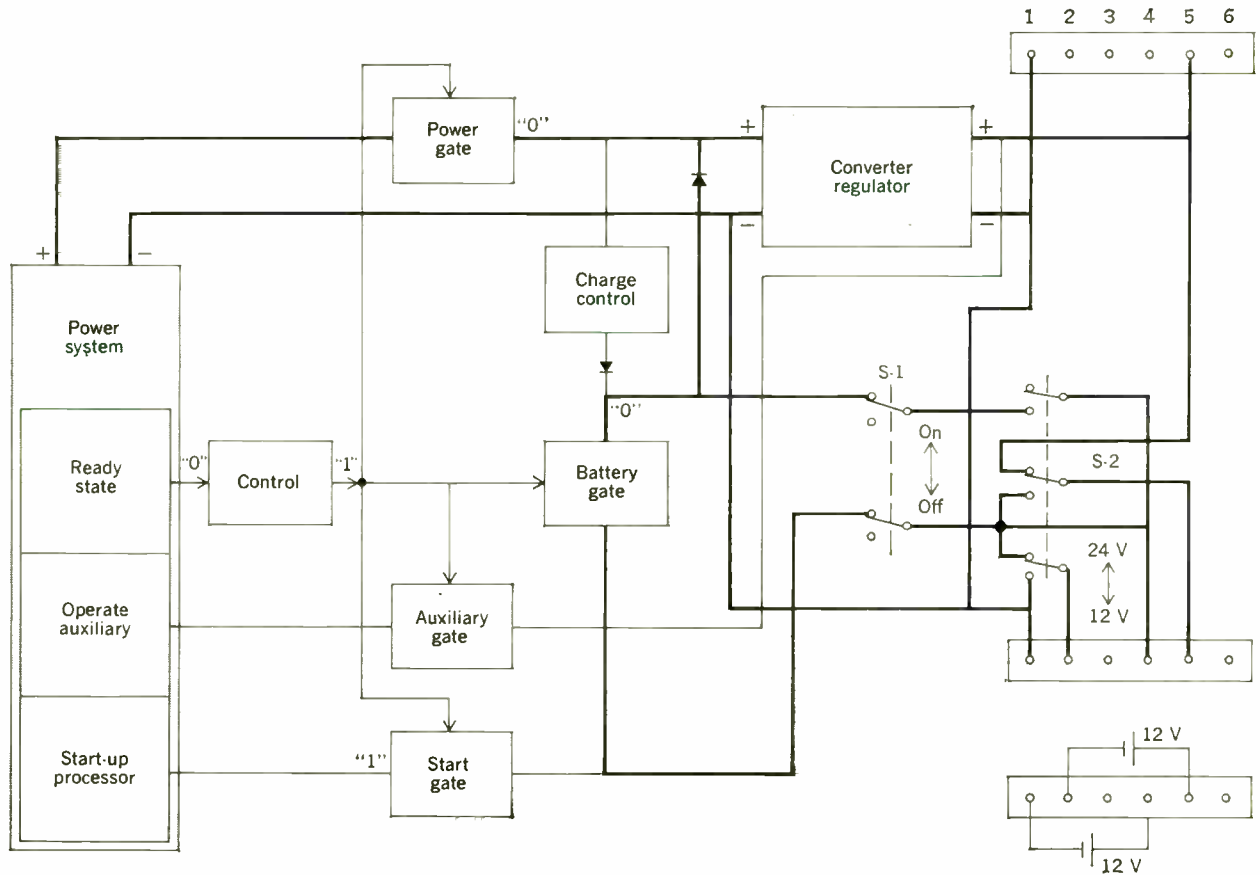
FIGURE 8. Simplified schematic diagram of hybrid control interface.

FIGURE 9. Electrical output characteristics of fuel cell–battery hybrid system.
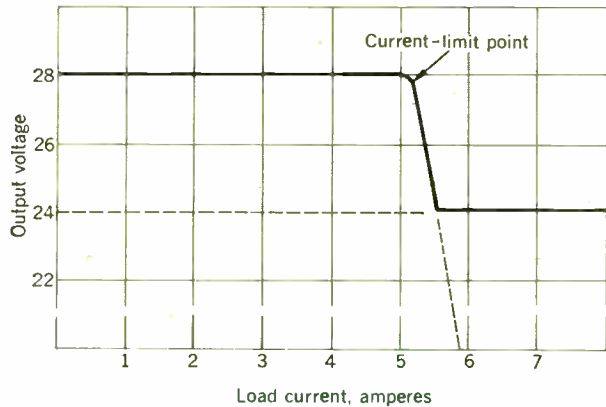
bles (fuel concentration, temperature, air flow). To allow high flexibility in control and the use of a lower operating voltage from the fuel cell stack, a dc-to-dc converter/regulator, with the output characteristics shown in Fig. 7, has been incorporated into the system. The converter/regulator has an adjustable output voltage from 28 to 32 volts to compensate for the fact that at lower temperatures of operation the battery must be floated at a higher voltage to obtain the desired recharge rates. Figure 8 is a simplified schematic diagram of how the battery is interfaced with

the dc-to-dc converter and the fuel cell stack.

Vented batteries, which can safely take up to 5 amperes of recharge current, can provide 24 volts directly to the output and will be recharged at 28 volts dc (28–32 volts adjustable) from the output of the dc-to-dc converter/regulator when no external load is applied. In this mode the fuel cell can be used as a battery charger for any battery (constant potential charge), not necessarily in a hybrid configuration.

Sealed batteries can also be used as a 12-volt input in parallel with the fuel cell power system input to the converter/regulator. The charge control and battery gate allow recharge of the 12-volt battery directly from the fuel cell stack. In this hybrid configuration power for the start-up processor is taken from the battery. This 12-volt source also serves to stiffen the input to the converter/regulator during transients, when the fuel cell stack voltage may drop to 12 volts. This start-up and stiffening function is independent of whether a 12-volt (paralleled sections of a sealed battery) or 24-volt vented battery (having a 12-volt tap across one side) is used.

Instant load capability is possible at 24 volts from an attached vented nickel–cadmium battery or through the converter/regulator from the sealed batteries. In either case the fuel cell power gate is closed when the control indicates a ready state (fuel cell at operating temperature). The output voltage jumps to 28 volts and is maintained there within the current limits of Fig. 7 and for as long as the fuel cell has fuel to maintain its output voltage.

A hydrazine fuel cell of the type described, in combination with an appropriately sized vented battery, can provide extremely high electrical output for short periods of time (1 to 2 minutes) without compromising the voltage stability of the whole system. The voltage–current characteristic of the hybrid system is shown in Fig. 9. At currents up to 5 amperes the output is held at 28 volts by the converter/regulator. At 150 watts the current limiter on the converter/regulator drops the voltage to the normal plateau of the attached 24-volt vented nickel–cadmium battery. The output voltage will remain at this plateau level depending only on the polarization characteristics of the size of the battery employed.

Hydrazine fuel cells

Hydrazine fuel cells have been in development for several years. An exploratory development model of a 60-watt cell is shown in Fig. 10. This fuel cell weighed 14.5 lb (6.6 kg) and produced approximately 390 watthours per pound (860 Wh/kg) of fuel. The chemical process system used is shown in Fig. 11. Hydrazine fuel is injected into an electrolyte tank to provide a constant level of hydrazine concentration in the anolyte. The anolyte is circulated through the

FIGURE 10. Exploratory development model of 60-watt hydrazine–air fuel cell.

FIGURE 11. Chemical-process system for hydrazine–air fuel cells.
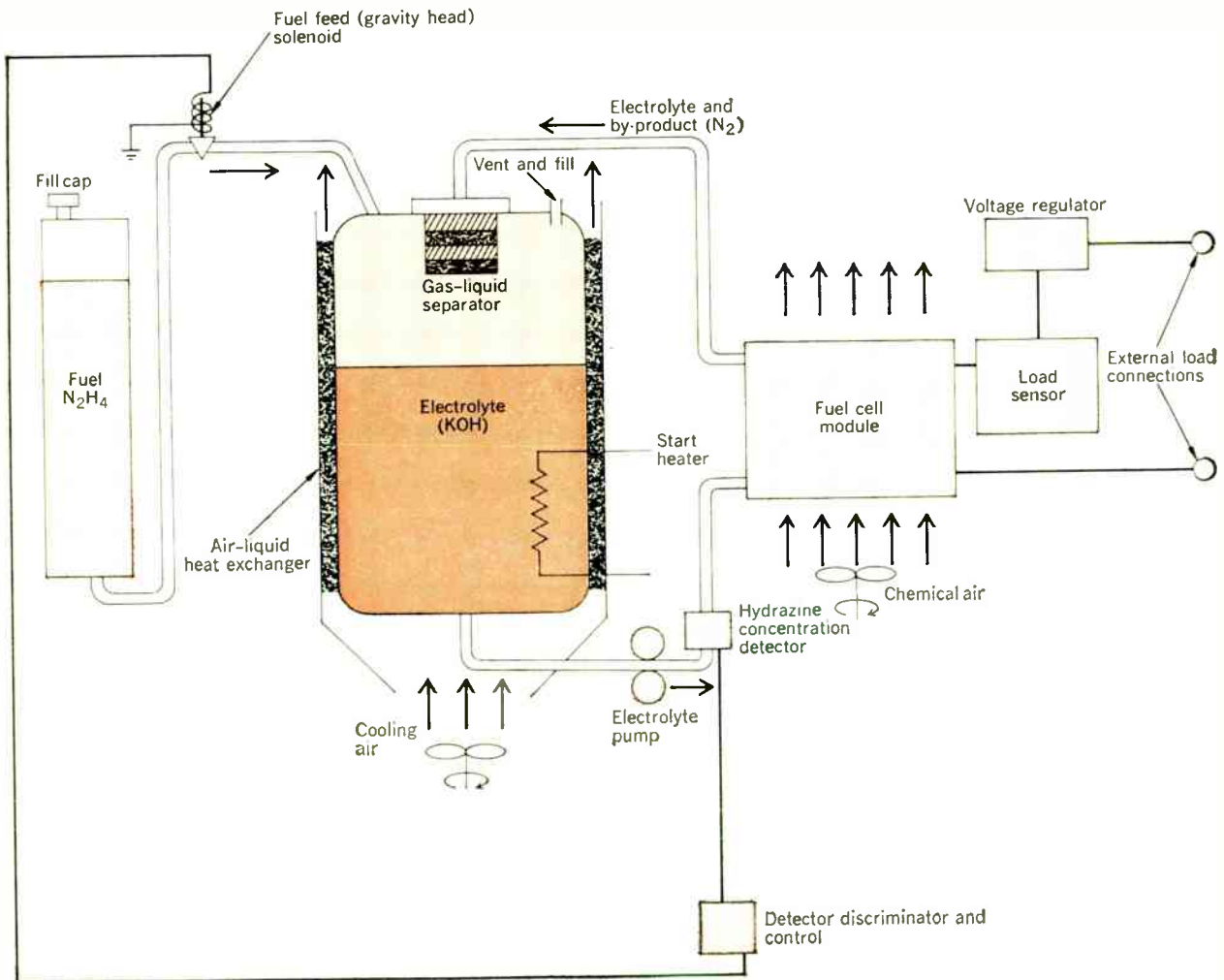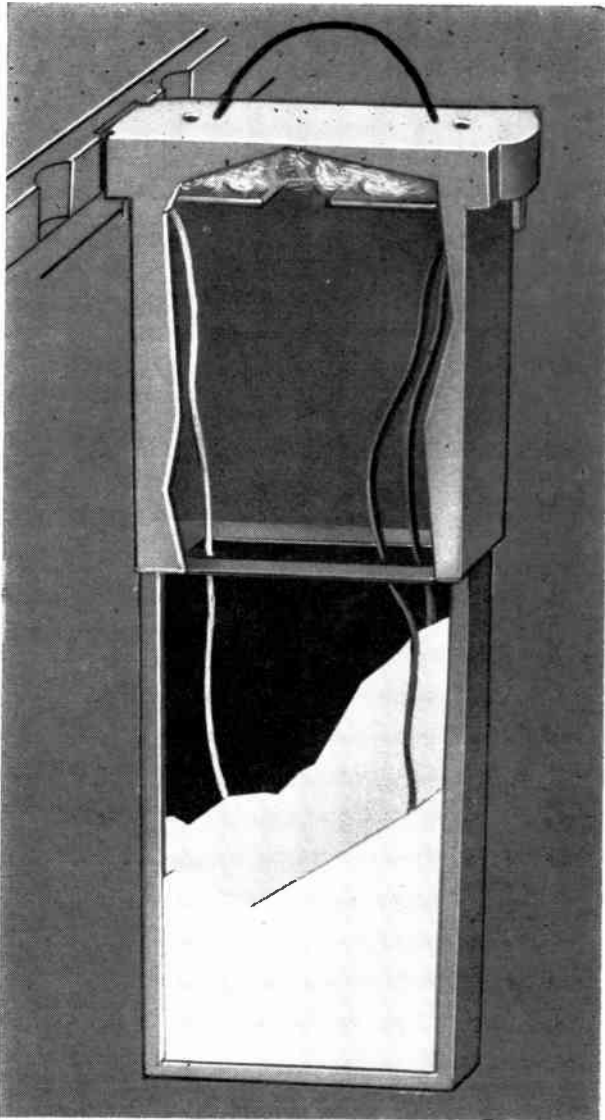
FIGURE 12. Hydrazine–air bicell.

FIGURE 13. Hydrazine–air fuel cell for use in a hybrid configuration.
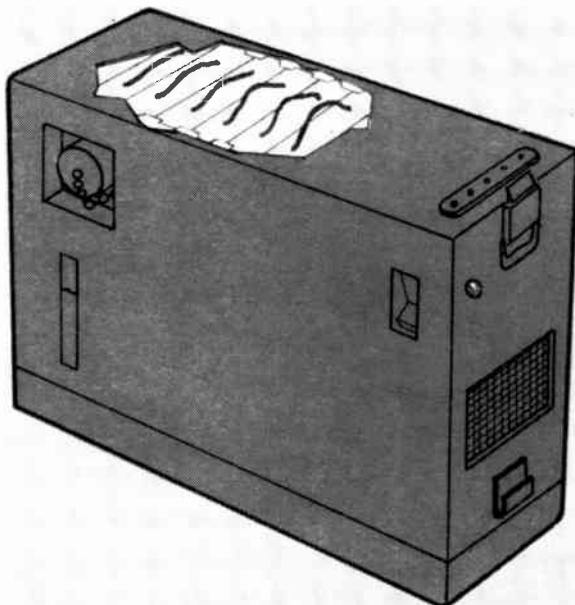
anode compartment of the fuel cell module and air is blown through the cathode compartment. Other components are required to maintain heat and moisture balances. More recent models have a simplified fuel-feed control system, which feeds fuel in proportion to the amount of gas evolved. A gas-exhaust pump in the anolyte compartment maintains a negative pressure on the anolyte, thereby improving the operation of the air cathode and removing the nitrogen formed as a reaction product. This reduced pressure can also be used to introduce fuel as required into the anolyte chamber.

By the use of a bicell construction, an alternative scheme would eliminate the common electrolyte (the same anolyte being used in a series of cells, which can result in current leakage and possible cross migration of active materials). This construction is very similar to that used in zinc–air cells, in which a replaceable zinc anode is contained between two air cathodes. In this case, however, a fixed, highly porous nickel anode is placed between two air cathodes (Fig. 12) and hydrazine is injected into the anolyte serving this single-voltage cell. The lifting action of the product nitrogen is sufficient to provide anolyte circulation. Incorporation of membranes for separators reduces hydrazine contact with the cathodes and allows the bicells to run at hydrazine concentrations as high as 20 to 25 percent. Periodic injection of hydrazine into the individual bicells can be accomplished by electrical or mechanical means. Figure 13 is an artist's conception of this simplified hydrazine fuel cell, which would mate in a hybrid configuration and have the output characteristics shown in Fig. 9. The operator interface is extremely simple. Liquid hydrazine fuel can be added to the fuel tank at periodic intervals. A simple on–off switch can activate the system. A light indicates to the operator when the fuel cell is providing its 28 volts through the dc-to-dc converter to the load or for recharging the associated battery.

Galen R. Frysinger received the bachelor's degree in chemistry from Juniata College in 1953. After receiving the master's and doctor's degrees from Yale University, he spent two years in Germany at the Max Plank Institut studying in his special field of electrochemistry with the aid of a Fulbright Scholarship and a National Science Foundation Fellowship. After returning to the United States he taught thermodynamics and physical chemistry at the University of North Carolina. He later worked on the development of new batteries for Arthur D. Little, Inc., as well as fuel cell development for the U.S. Army Research and Development Laboratories, Fort Belvoir, Va. He is now chief of the Power Sources Division, U.S. Army Electronics Command, Fort Monmouth, N.J.

Power requirements for ~~deep-space~~ telecommunication links

The vital communications link between earth and various space probes, manned or unmanned, must be maintained in order to insure safety and obtain needed information — and these requirements must be met with a maximum of power and efficiency and a minimum of space-borne weight

M. H. Brockman, E. C. Posner   California Institute of Technology

The signal-to-noise ratio in a given equivalent bandwidth must be maintained above a minimum value during a deep-space mission in order to provide predictable performance, and in order to maintain effective telemetry communications with spacecraft at interplanetary distances it is necessary for earth stations to use maximum antenna gain. One solution is to extend telecommand range by reducing system noise temperature in the spacecraft receiver and reducing the bandwidth of the receiver's phase-lock loop. Low-noise preamplifiers have not yet been applied in planetary spacecraft in order to maintain simplicity and reliability. An answer to the problem seems to be high-power transmitters (earth-based) with outputs in the 1000-GW range.

A successful deep-space research mission requires a telecommunications link between the spacecraft and the earth stations that can provide three basic functions —tracking, telecommand, and telemetry—over interplanetary distances. The tracking function provides information for (1) the determination of the position

and velocity of the spacecraft, (2) the determination of the precise time for critical maneuvers, and (3) angular pointing for highly directional earth-station receiving and transmitting antennas. In addition, tracking permits scientific investigation of the atmosphere of the sun and planets during periods when the spacecraft is occulted by them. The telecommand function permits earth stations to guide and control the spacecraft, and the telemetry function provides for transmission back to the earth stations of scientific and engineering data obtained aboard the spacecraft. The three functions are combined in a system, as shown in Fig. 1, which provides for efficient utilization of the radio spectrum.

The telecommunications system functions in either a one-way or a two-way coherent mode. In the one-way mode, telemetry information phase-modulates a crystal-controlled carrier frequency generated in the spacecraft, which is then transmitted to the base station. The telemetry information is demodulated at the station receiver by means of coherent detection techniques. In the coherent two-way mode, the earth station trans-

FIGURE 1. Spacecraft block diagram illustrating combined tracking, telecommand, and telemetry.
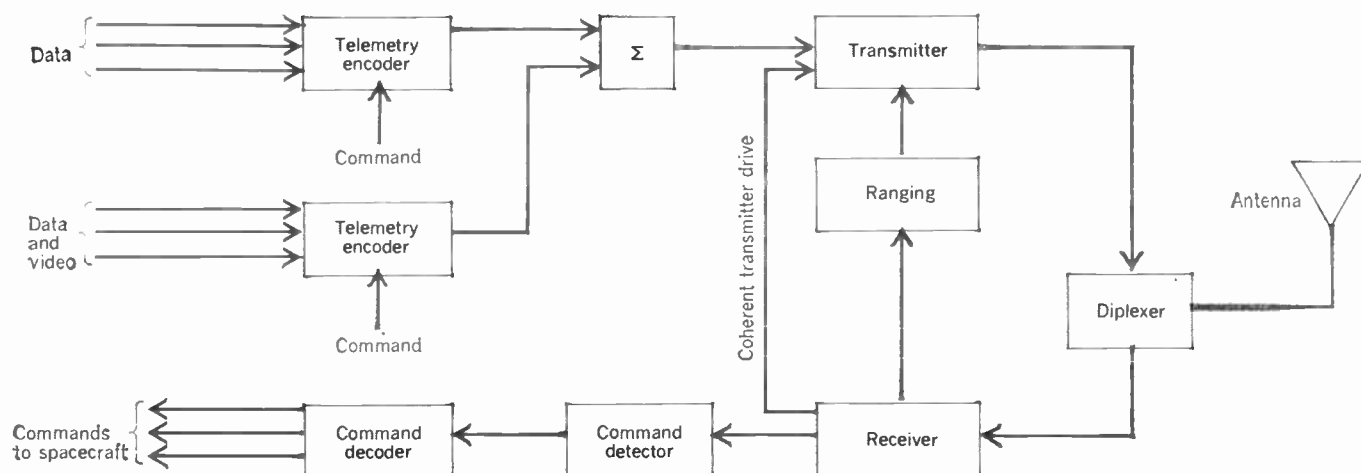
mits a phase-modulated radio-frequency (RF) carrier to the deep-space vehicle. The spacecraft receiver coherently tracks the RF carrier by means of a phase-lock loop. After coherent frequency translation, the spacecraft transmits the phase-lock loop estimate of frequency and phase as the carrier for transmission of telemetry information back to the earth station. The earth station receiver coherently tracks the phase of the received carrier and demodulates the telemetry information. In this two-way mode, precise measurement of radial velocity (relative to the earth base) is obtained as a two-way Doppler shift of the RF carrier. In addition, accurate measurement of range is obtained by

appropriate phase modulation of the earth-to-spacecraft-link RF carrier, modulation detection in the space vehicle receiver, and remodulation of the spacecraft-to-earth-link RF carrier by the detected modulation waveform. Telecommand information is transmitted to the spacecraft as phase modulation of the earth-to-spacecraft link, and telemetry information is transmitted to the earth as phase modulation of the spacecraft-to-earth link. When transmitting telecommand, the two-way coherent mode is generally used although it is possible in an emergency to transmit telecommands blind, that is, without immediate knowledge of the reception by the spacecraft of the telecommand.

In order to maintain effective telemetry communications with spacecraft at interplanetary distances, it is necessary to use as much antenna gain as possible in the communication system. It is more economical to put some of the required gain on the spacecraft through use of directional antennas than to put all of it in earth station. The gain of the spacecraft directional antenna
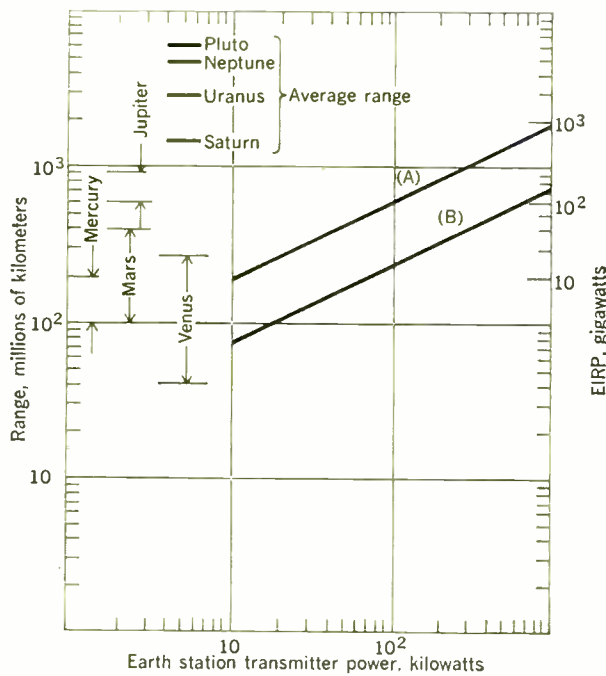
FIGURE 2. Chart at left illustrates telecommand capability at 2.1 GHz. Spacecraft is using an isotropic antenna with an RF loop bandwidth of 20 Hz; command rate is equal to one bit/second, and BER is 1/10, with a 10-dB margin. Earth-station antenna diameters are (A) 64 meters and (B) 26 meters.

FIGURE 3. Chart (below, left) illustrates turnaround ranging capability at 2.1–2.3 GHz. Spacecraft is using an isotropic antenna with an RF loop bandwidth of 20 Hz for reception; for transmission the antenna diameter is one meter, with a nine-degree beam width. RF power = earth station power/12 × 10. Earth station has an RF bandwidth of 3 Hz. Antenna diameters as in Fig. 2.

FIGURE 4. Chart shown below illustrates telemetry capability (coherent two-way model) at 2.1–2.3 GHz. Isotropic spacecraft antenna has an RF loop bandwidth of 20 Hz (receiving), and earth-station antenna has a 3-Hz RF loop bandwidth. Antenna diameters as in Fig. 2.
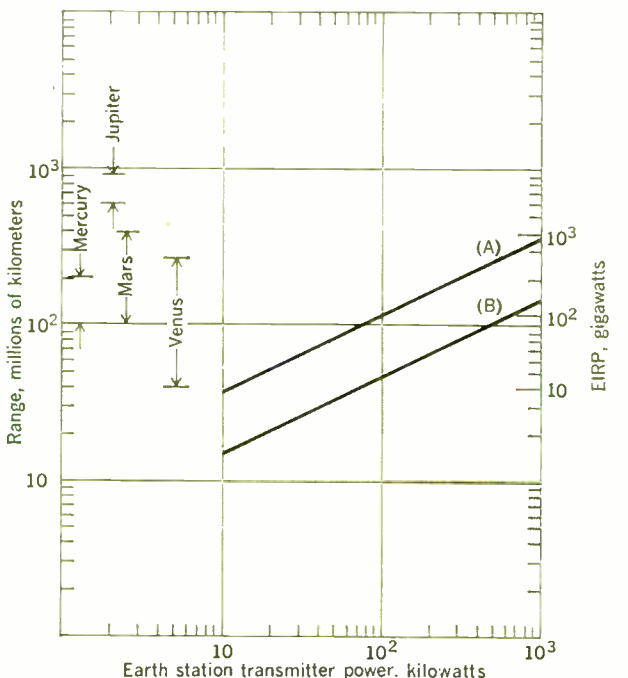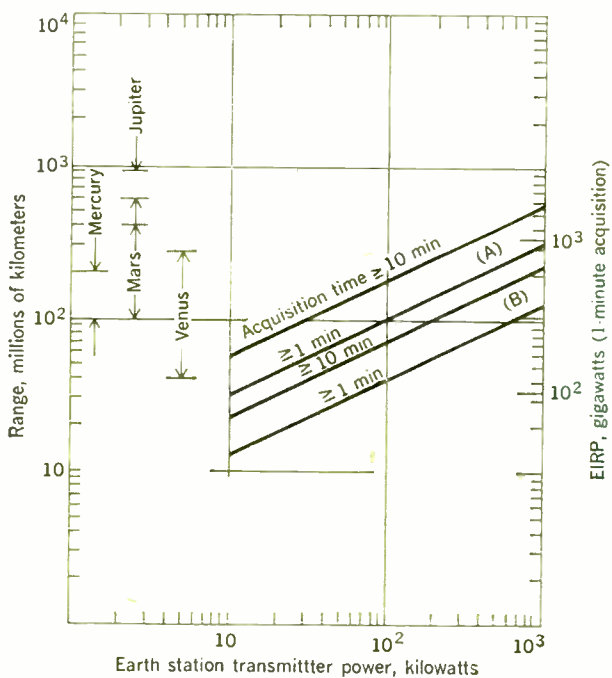
is heavily dependent on practical economic considerations as well as the size and physical capacity of the launch vehicle; gains of 10 to 25 dB are presently being achieved. However, the use of directional antennas requires a spacecraft attitude-positioning capability; this capability is usually accomplished by using power jets that are controlled either automatically, from celestial sensors aboard the spacecraft, or by telecommand from the earth. Since the spacecraft directional antenna may not always be pointing toward the earth, either because of the necessity for spacecraft maneuvers or because of the failure of attitude sensors, the success of a mission is critically dependent upon the ability to send telecommands to a spacecraft during crucial periods, regardless of its attitude. This is accomplished by using omnidirectional antennas on board the spacecraft. Because of the difficulty of designing truly omnidirectional antennas on board large spacecraft, such antennas generally have gains of from zero to several decibels less than zero, depending on spacecraft attitude.

It is possible to extend the telecommand communications link range by reducing the system noise temperature of the spacecraft receiver and reducing the bandwidth of the spacecraft receiver phase-lock loop. However, due to spacecraft receiver simplification, reliability, and weight reduction, low-noise RF preamplifiers have not been considered. The bandwidth of the phase-lock loop in the receiver is dependent upon a complex interplay among phase noise, acquisition reliability, and spectral purity of the RF carrier transmitted from the earth.

Telecommunication capability

In order to provide predictable performance capability, the signal-to-noise ratio in a given equivalent bandwidth must be maintained above a minimum value during a deep-space mission. In the following material, which provides typical characteristics for telecommand, tracking, and telemetry, propagation between the spacecraft and earth station is line of sight through space assumed to be transparent to the radio waves, subject to the effects of the earth's atmosphere on propagation and on apparent sky noise temperature.[1,2]

For both the telecommand and telemetry functions the ratio of signal energy per bit to noise spectral density ST_b/N_o must be maintained above a minimum value to realize the desired bit error rate (BER) or average bit error probability.[3] In addition, the signal-

to-noise ratio in the RF carrier tracking phase-lock loops must be maintained at a sufficiently high level (typically +16 dB) so that ST_b/N_o, and hence the bit error rate, will not be materially affected by RF carrier phase noise.[4]

Figure 2 illustrates the RF power requirements at an earth station to transmit telecommands to a spacecraft within the solar system. This figure is based upon the present deep-space telecommand characteristic; namely, a carrier frequency of 2.1 GHz, a command data rate of one bit per second with a bit error rate of 1 in 10^5, a 10-dB margin for various losses, and an omnidirectional spacecraft antenna with a gain of unity. Figure 2 illustrates that a minimum of 100-GW eirp (equivalent radiated power relative to an isotropic antenna) will be required for communication with a
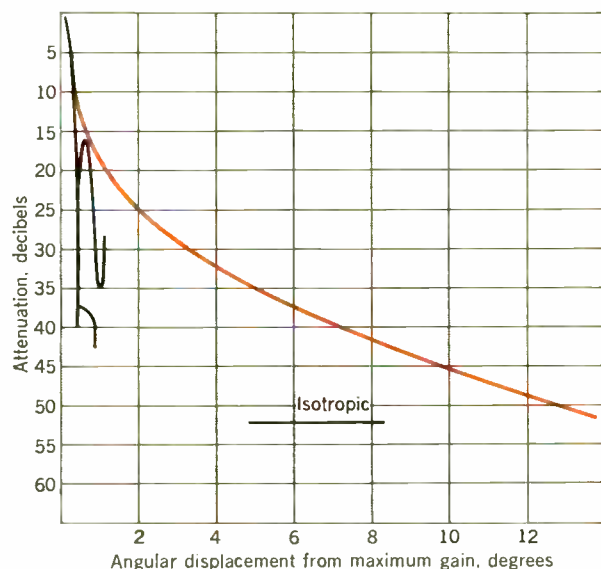
FIGURE 5. Antenna peak sidelobe pattern characteristic for a 26-meter-diameter paraboloid.

FIGURE 6. Peak sidelobe pattern characteristic for a 64-meter-diameter paraboloid antenna.
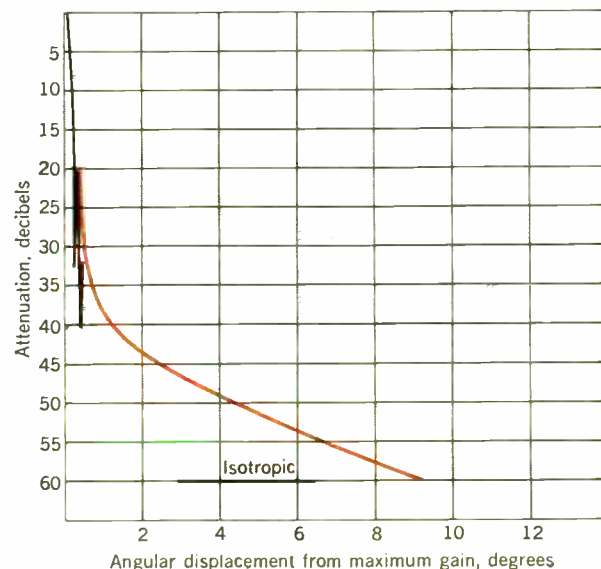
I. PSK telemetry capability

Spacecraft Transmitter Antenna			Ratio of Station to Spacecraft Trans-mitting Power	Digital Coding	Data Rate, bits per second
Diam., meters	Gain, dB	Beam Width, degrees			
1.0	25	9	400 000	Uncoded	10
			65 000	Uncoded	100
			16 000	Uncoded	500
			16 000	Block coded	800
2.0	31	4.5	4 000	Block coded	15 000
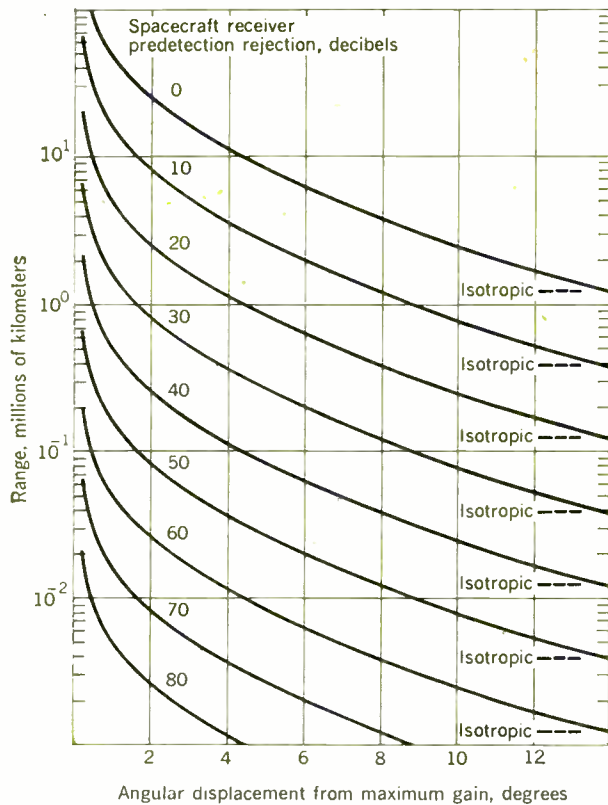
FIGURE 7. Spacecraft RF interference resulting from a 26-meter-diameter earth-station antenna peak sidelobe radiation (transmitter power 100 kW).

FIGURE 8. Spacecraft RF interference resulting from 64-meter-diameter earth-station antenna peak sidelobe radiation (transmitter power 100 kW).
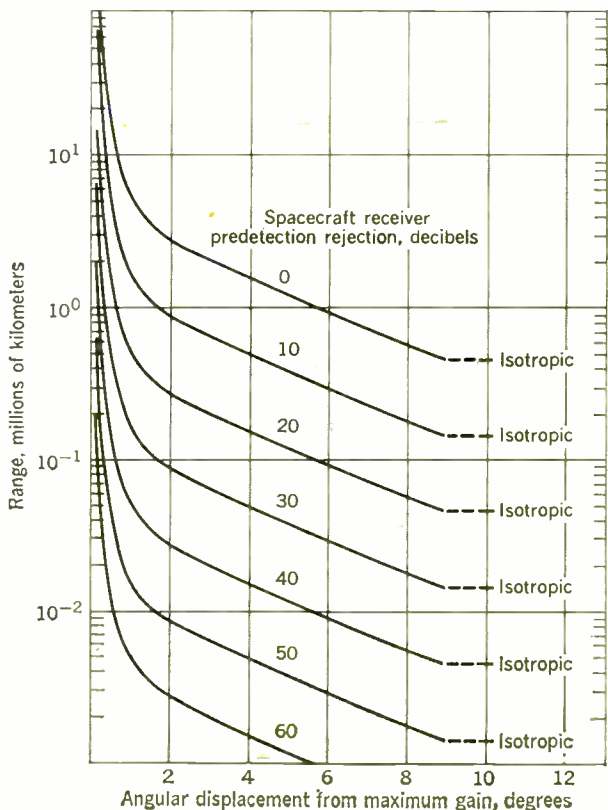
spacecraft at Jupiter distance and that, even with 1000-GW eirp, improvements will have to be made in the telecommand communication link in order to communicate at distances equal to the orbits of the three outer planets.

One must also consider the need of high power for tracking and telemetry purposes. It is necessary at this point to consider the spacecraft's transmitter power and antenna gain and the sensitivity of the earth station. Figures 3 and 4 illustrate these two functions, using the present capabilities of the Deep Space Network and typical spacecraft directional antennas and transmitter powers. In Fig. 3, turnaround ranging capability is illustrated for acquisition times of one minute and ten minutes. It should be noted that a ten-minute acquisition time represents near-threshold conditions for ranging. The eirp values shown in Fig. 3 are associated with the one-minute acquisition capability. Representative telemetry capability associated with the coherent two-way mode illustrated in Fig. 4 is shown in Table I for uncoded and block-coded digital phase-shift-keyed (PSK) telemetry systems,[3] using biorthogonal coding for bit error probability of 1 in 10³. The characteristic shown in Fig. 4 is conservative, since it includes a 10-dB margin for communication-link circuit losses and for tolerances on communication-link parameters; any reduction in this margin will provide a corresponding increase in telemetry range.

It will be noted that Fig. 2 indicates a greater range capability for a telecommand than for either ranging or coherent telemetry. In actual practice the telecommand capability has never been used by itself except in an emergency when commands have had to be sent blind. Generally, commands have been sent when the telecommunication channel is in a two-way coherent mode, so that the earth station can receive telemetry that will determine the successful acquisition of the command by the spacecraft and can obtain ranging and tracking data for use in determining spacecraft location and orbit. In addition, it is desirable for the earth station to know the spacecraft receiver automatic-gain-control setting and loop phase error in order to optimize the earth-to-spacecraft communication link. It is also necessary to have a sufficiently strong carrier received at the spacecraft, so that the resultant phase noise in the coherent frequency translation loop will not impair the telemetry demodulator performance at the earth station.

RF interference

Figures 5 and 6 represent the peak sidelobe radiation of 26- and 64-meter-diameter paraboloid antennas operating at 2.1 GHz, with a Cassegrain shaped-beam feed system. It is noted that isotropic radiation is reached at an angle of 14 degrees off the main beam for a 26-meter-diameter antenna and 9 degrees off the main beam for a 64-meter-diameter antenna. Using the information illustrated in Figs. 5 and 6, the sidelobe-radiation characteristics at 2.1 GHz are obtained for the 26- and 64-meter-diameter earth station antennas. This sidelobe radiation results in an interfering signal level of −171 dB (W),[5] at ranges shown in Figs. 7 and 8, to a spacecraft receiver with 0-dB predetection rejection, and operating with an isotropic antenna for line-of-sight propagation through transparent space.

with the earth station transmitting at 15 and 95 GW eirp, respectively, in the main beam. Predetection rejection is defined as any attenuation to an interfering signal (normally achieved by filtering in the receiving system) that occurs prior to RF-carrier detection and command demodulation. Consequently, predetection rejection in the spacecraft receiver to earth station radiation (of interfering RF carriers and telecommands) permits a corresponding increase in input signal level above −171 dB (W) as shown in Figs. 7 and 8. For RF-carrier tracking and telecommand, spacecraft receivers have predetection filters with half-power bandwidths of a few kilohertz. At frequencies displaced about five times the half-power bandwidth, the predetection filter typically provides a predetection rejection of 40 dB. A 40-dB predetection rejection will permit operation of the 26- and 64-meter-diameter antennas to within 1.5 and 0.3 degrees, respectively, of line of sight to another spacecraft at lunar distances for the eirp values considered in Figs. 7 and 8.

Figures 7 and 8 illustrate that radiation interference to spacecraft can be effectively eliminated by proper selection of frequencies for the various spacecraft. In addition, during the near-earth phase of a mission, the earth station antenna can be scheduled so as not to illuminate another spacecraft with the main antenna beam.

Interference to earth receivers

Earth stations are located in isolated areas that provide a natural horizon of several degrees above horizontal. For over-the-horizon propagation by sidelobe radiation (0-dB gain region) with an interference level of −220 dB (W) per hertz and 100-kW transmitter power, the minimum permissible distance between typical deep-space earth stations and terrestrial stations is 440 km. This spacing is required for the case of 0-dB predetection rejection. It should be noted that predetection rejection between deep-space stations (transmit and receive) is greater than 200 dB for an 8 percent difference between transmit and receive frequencies. As a consequence, predetection rejection of the earth-based receiver to the earth-based transmission greatly reduces the 440-km minimum permissible spacing between stations.

Reflection via the moon should also be considered as a possible means by which an interference level of −220 dB (W) between earth stations can be realized. With a 26-meter-diameter receiving antenna pointed at the moon, a predetection rejection of 40 dB is required when a 26- or a 64-meter-diameter transmitting antenna, operating at 400 kW, is illuminating the moon with sidelobe radiation (0-dB gain region). For the 8 percent difference between transmit and receive frequencies described in the foregoing, the transmitting antennas can be pointed directly at the moon at a transmitter power level of 1000 kW without causing interference.

Conclusions

Deep-space exploration of the four nearest planets will require earth station eirp values of up to 1000 GW.

Because of the high-power RF levels, the predetection rejection of near-earth satellites to deep-space

transmissions must be specified, so that pointing of the earth station antenna can be scheduled when necessary.

Deep-space vehicles can operate on closely adjacent frequencies providing that adequate predetection rejection between spacecraft is specified, so that RF interference resulting from high-power RF radiation can be effectively eliminated during a mission.

Consideration should be given to the need for eirp values greater than 1000 GW for deep-space exploration to the four outer planets.

REFERENCES

1. "Factors affecting the selection of frequencies for telecommunications with and between spacecraft," CCIR Rept. 205-1, Documents of the IXth Plenary Assembly, Oslo, 1966, published by the Internat'l Telecommunications Union, Geneva, 1967.
2. Dimeff, J., Gunter, W. K., Jr., and Hruby, R. J., "Spectral dependence of deep-space communications capability," IEEE Spectrum, vol. 4, pp. 98–104, Sept. 1967.
3. Golomb, S. W., Baumert, G. D., Easterling, M. F., Stiffler, J. J., and Viterbi, A. J., Digital Communications. Englewood Cliffs, N.J.: Prentice-Hall, 1964.
4. Lindsey, W. C., "Performance of phase-coherent receivers processed by bandpass limiters," IEEE Trans. Communication Technology, vol. COM-16, pp. 245–251, Apr. 1968.
5. "Interference and other special considerations for telecommunication links for manned and unmanned spacecraft in the space-research service," CCIR Rept. 219-1, Documents of the XIth Plenary Assembly, Oslo, 1966.

M. H. Brockman (SM) received the B.S.E.E. degree from the University of Washington in 1943 and the M.E.E. degree from Polytechnic Institute of Brooklyn, N.Y., in 1953. He was a special research associate at the Radio Research Laboratory, Harvard University, from 1943 to 1945. From 1946 to 1955 he served as a member of the engineering staff at the Airborne Instruments Laboratory, Mineola, N.Y.

Since 1955 Mr. Brockman has been employed at the Jet Propulsion Laboratory, California Institute of Technology, in the Telecommunications Division, concerned principally with research and development of deep-space tracking and communications. He participated in the early Explorer satellite experiments as well as early lunar probe experiments (Pioneer III and IV) and Project Echo.

E. C. Posner (SM) who was born in New York, N.Y., in 1933, received the B.A. degree in physics from the University of Chicago in 1952. He received the M.A. and the Ph.D. degrees in mathematics from the same university in 1953 and 1957, respectively.

Dr. Posner worked in the Advanced Systems Studies Department of Bell Telephone Laboratories, New York, N.Y., from 1956 to 1957. In 1957 he joined the staff of the University of Wisconsin Mathematics Department as a research instructor in mathematics and statistics. He joined the Jet Propulsion Laboratory in 1961, heading the Information Processing Group there until 1967, when he was appointed deputy manager of the Communications Systems Research Section. In 1968 he assumed the additional duties of Telecommunications Division representative for research and advanced development.

The future role of breeder

J. K. Dillard, C. J. Baldwin, N. H. Woodley
Westinghouse Electric Corporation

Numerous considerations, chiefly related to cost, contribute to the growth pattern of electric generation. Although water reactors will undoubtedly dominate U.S. nuclear expansion into the 1980s, the high-gain fast breeder holds the greatest economic advantage over the long term. The factors leading to this conclusion are presented and analyzed here, and some predictions are made for the 20-year period beginning in 1986.

The economy and reliability of the light-water reactor in the United States have resulted in a growth of nuclear power far beyond the expectations of optimistic forecasters of recent years. In 1967 there were about 2900 MW of nuclear power in operation.[1] In 1966 alone, orders were placed for 23 000 MW in 29 separate nuclear units. In the first half of 1967 an additional 17 000 MW of capacity, representing 22 more nuclear units, was ordered.[2] The result has been a spread of nuclear power over most areas of the United States, except those regions with very low fuel cost or sparse populations (Fig. 1).

This accelerated growth rate is the direct result of decreasing costs of nuclear power over the past decade. This has greatly expanded the span of competition for nuclear power in the United States. For example, at the World Power Conference in Lausanne, Switzerland, in 1964, a report was presented showing the merits of nuclear power in areas where the delivered cost of fossil fuels was more than 28.4 cents per million kilojoules (30 cents per million Btu).[3] Shortly after preparation of that paper, substantial improvements were made in the capital and fuel costs of water reactors. For a year or so, reactors competed with fossil fuels in the neighborhood of 23.7 cents per million kilojoules (23.7 cents per gigajoule). In late 1966, taking cognizance of further capital and fuel cost improvements, a study showed that nuclear plants for base-load operation could be built to compete with coal-fired plants using fuel costing as low as 18 cents/GJ.[4]

The massive expansion program of nuclear plants has brought about repeated revisions of long-range nuclear capacity forecasts. The most recent authoritative prediction indicates that by 1980 there will be 150 000 MW of installed nuclear capacity in the United States.[5,6] By the year 2000 the U.S. Atomic Energy Commission expects this figure to grow to 750 000 MW[7]; see Fig. 2. The cumulative ore requirements resulting from this capacity prediction are

FIGURE 1. Central-station nuclear installations in the United States and Puerto Rico (August 23, 1967).

Nuclear Generating Capacity		
• In operation	(18)	2 900 MW (e)
▲ Planned and under construction	(48)	50 000 MW (e)
TOTAL	(66)	52 900 MW (e)
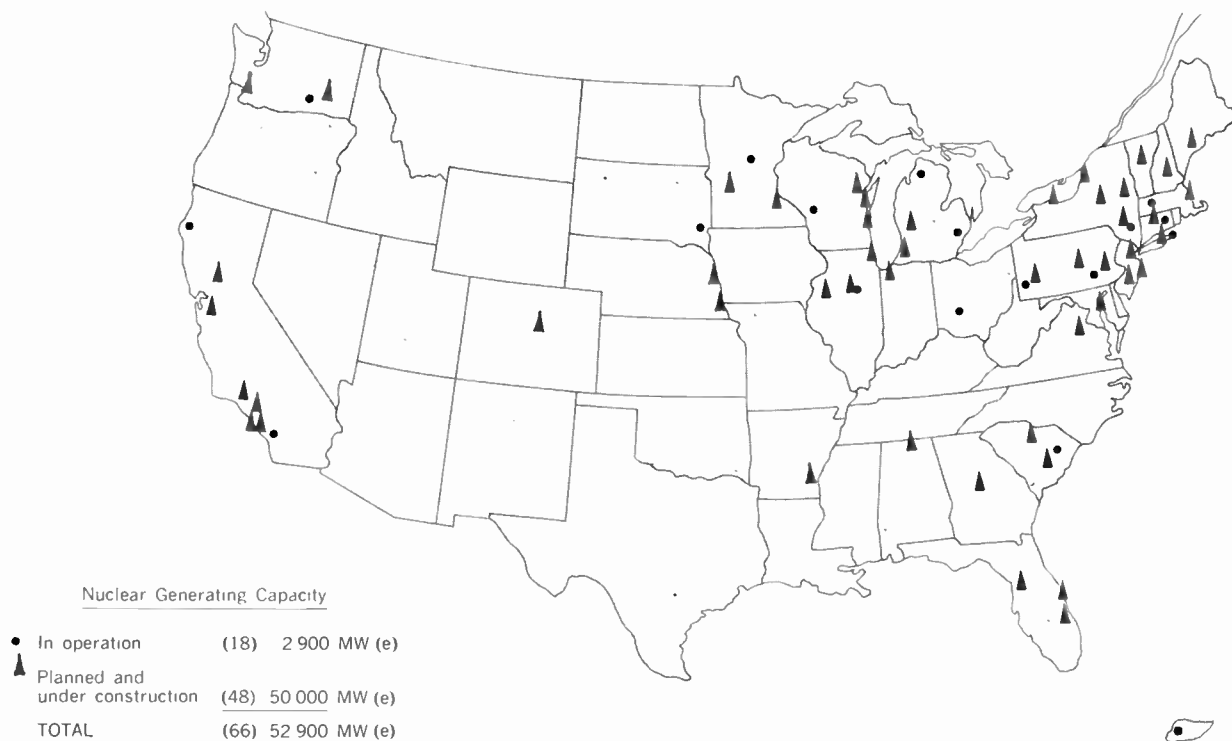
reactors in utility planning

Breeder reactors are expected to play an increasingly important part in the overall energy generation picture in the United States, particularly after the mid-1980s

shown in Fig. 3.[7] Approximately 200 000 tonnes (200 million kilograms) of U_3O_8 will have been required by 1980. To meet this large demand, the uranium mining industry has recently announced that it will spend collectively over $77 million by 1970 in exploration to increase known reserves substantially.[8] Hence, it is reasonable to believe that nuclear growth will continue as indicated by current predictions.

As water reactors consume fissile uranium, a certain amount of fissile plutonium is produced. Of course, this plutonium can be recycled into the water reactors—but beyond 1980, with ever-larger amounts of plutonium being produced, additional economic benefits can be realized by the development of a commercial high-gain fast breeder reactor. Utilizing plutonium as fuel, this reactor creates a better market for plutonium produced by today's light-water reactors.

Besides producing more fissile material than it consumes, the high-gain fast breeder operates at a much higher temperature, improving the thermal efficiency of the overall cycle. Today's light-water reactors convert approximately one percent of the latent energy of the fuel into thermal energy. With the breeder it is possible to convert over 60 percent of the latent energy of the fertile fuel into heat. With a breeding ratio of 1.5, the amount of fissile material can be doubled every ten years or less, enough to keep pace with the growth of the U.S. utility load.

Economic study techniques

The economic justification for breeder reactors requires long-range projection of system load growth and plant usage. Characteristics of single units cannot be compared because of the influence of one unit on another in day-to-day plant usage and in long-range impact on fuel availability and price. Fortunately, digital computer simulation programs have been avail-

able for about eight years to study long-range economic problems of utilities.[3,9]

The digital programs simulate system growth on a week-by-week basis over time periods of 10 to 30 years. The computer programs automatically determine future unit installation dates using probability mathematics to maintain system reliability to a specified criterion. They simulate realistic annual maintenance schedules, operating rules covering spinning reserve, and the economic dispatch of generating units to meet the simulated load in each week.

Each computer run evaluates the annual revenue requirements and their present worth for a specific generation expansion pattern.[10] The revenue requirements may not be the same each year, but it is possible to use a levelized equivalent. Table 1 is an illustrative example of the computation of levelized annual savings for a 35 percent breeder–65 percent water reactor pattern compared with a base case. The present-worth savings of $511.61 million can be levelized over the 20-year study period by dividing the sum of the present-worth factors for the period. The resulting $44.6 million savings each year of the study period is then exactly equivalent to a larger single-payment present-worth value at the beginning of the period. Use of

FIGURE 2. Forecast of installed nuclear generating capacity for the United States.
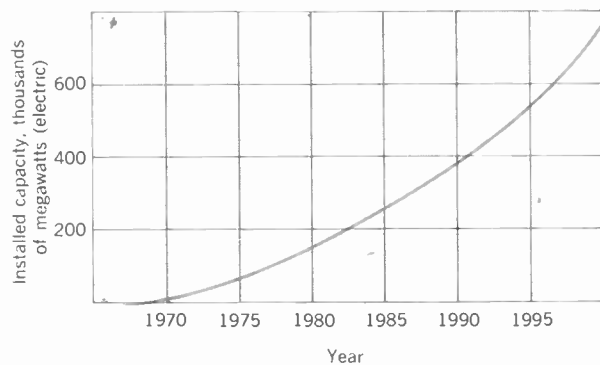
FIGURE 3. Cumulative U_3O_8 requirements.
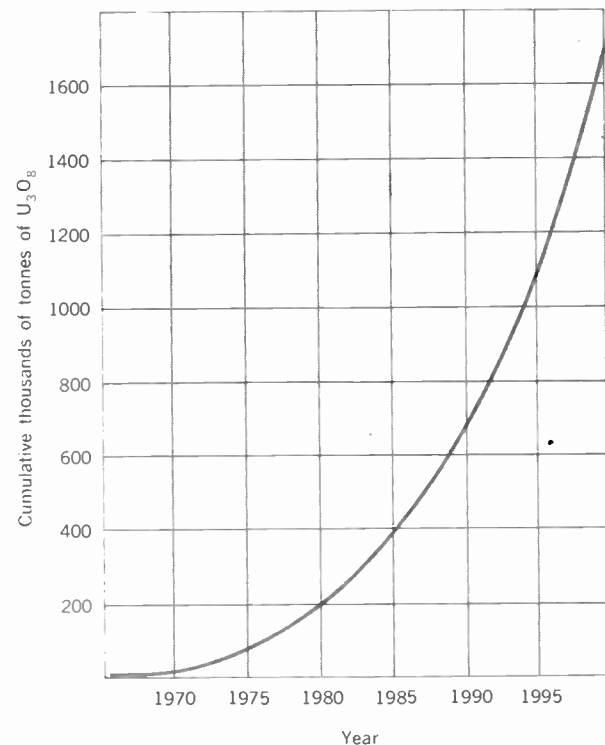
equivalent levelized values permits comparison of expansion alternatives on an economic basis.

A generation expansion pattern is a list of specific future generating units, in desired order of installation, to be installed during the simulated growth. By repeating the growth simulation, each time with a different expansion pattern, the economic evaluation for each alternative is determined. The alternative pattern with the lowest present worth of all future revenue requirements is the economic choice.

The results of different expansion-pattern evaluations are all represented as savings of various patterns over a base case. An all-fossil expansion pattern is an appropriate base case in a study of the introduction of the first water reactors. In a breeder-reactor study, a logical base case is the optimum water-reactor pattern that can be developed.

I. Computation of levelized annual savings, millions of dollars

	Base Case (35% WR, 65% F)		Alternate Pattern (35% BR, 65% WR)
Generating plant investment	$1784.00		$1406.39
Production expense	2974.00		2840.00
Present-worth future revenue requirements*	$4758.00		$4246.39
Savings		$511.61	

$$\text{Levelized annual savings} = \frac{(\text{Savings})}{\sum\limits_{n=1}^{20} \text{PWF}_n} = \frac{\$511.61}{11.4699} = \$44.60$$

* These figures are present worth of revenue requirements for 20 years of the study period.

With digital simulation techniques, the use of breeder reactors can be compared with the use of water reactors only, or with the use of fossil-fuel plants only, or with any mix of the three types. All important parameters may be varied to study the sensitivity of the economic choice to fossil-fuel price, breeder capital cost, nuclear-fuel price, and utility growth rate.

The system hypothesis

The best way to study breeder-reactor economics is to examine the role of breeders on a power system in which a significant percentage of the installed generation is nuclear. Over the past two years, such a system has been studied. It has a present installed capacity of 4000 MW and will have approximately 14 000 MW installed by 1986, of which 35 percent will be nuclear. Detailed characteristics of the system are given in Table II, which reflects a load growth rate of 7 percent. Seasonal peak-load variations and weekly load curves are typical of those found on many U.S. systems. The system has an annual load factor of 58 percent and a winter peak; however, the study results would be unaffected by varying the time of peak.

A 20-year study period was chosen, since this is the usual period used in U.S. studies. The base year was chosen to be 1986, which is estimated to be the first year that operation of large-scale commercial fast breeder reactors could have any significant impact. New units are assumed to range in size from 1000 to 3500 MW, typical for a 1986 power system of 14 000 MW that grows to 50 000 MW by the twentieth year, 2005. Figure 4 shows the relative capital cost of fossil units, water reactors, and fast breeder reactors as a function of size. Table III shows operation and maintenance costs and full-load heat rates for these same large units.

Forced outage rates and maintenance cycles are important parameters, since they determine the amount

II. Existing 1986 system

	Fossil	Gas Turbine	Nuclear
Initial installed capacity, fossil base pattern, MW	13 940	2600	0
Initial installed capacity, nuclear base pattern, MW	9220	2600	4720
Number of units, fossil base pattern	72	17	0
Number of units, nuclear base pattern	66	17	6
Average unit size, fossil base pattern, MW	194	153	
Average unit size, nuclear base pattern, MW	140	153	787
Maximum unit size, fossil base pattern, MW	950	200	
Maximum unit size, nuclear base pattern, MW	600	200	950
Full-load heat rate, fossil base pattern, kJ/kWh (Btu/kWh)	9100–15 800 (8625–15 000)	12 650 (12 000)	
Full-load heat rate, nuclear base pattern, kJ/kWh (Btu/kWh)	9270–15 800 (8800–15 000)	12 650 (12 000)	10 900–10 950 (10 350–10 400)
Fuel cost, cents/GJ (cents/MBtu)	19–23.7 (20–25)	47.4 (50)	8.75–8.91* (9.23–9.4*)
Forced outage rate, percent	5.0	1.0	5.0
Five-year maintenance cycle, weeks/year	3-3-4-3-3	0-0-1-0-0	3-3-4-3-3

1985 peak load: 13 351 MW
Load-growth rate: 7 percent
Load factor: 0.58

* Does not include working capital for fuel inventory.

of reserve capacity and date of unit installations. For base-load units (breeders, water reactors, and fossil plants) a five-year maintenance cycle of 3-3-4-3-3 weeks per year including refueling time for nuclear units was used. A 5 percent forced outage rate was used for the base-load units. Evidence to date suggests that this rate is too high for nuclear units, but it was used as a conservative estimate. The expansion patterns were supplied with some peaking units, since our experience indicates that optimum system development usually requires their use. Gas turbines were used with a forced outage rate of one percent and one week of maintenance every third year.

Expansion-pattern development

An unlimited number of expansion patterns might be devised to study breeder economics. However, careful selection of expansion patterns will point out the importance of major parameters in breeder-reactor economics and the sensitivity to these parameters. Table IV shows a few, but not all, of the patterns. These are representative of the various mixes that were examined. In the first pattern shown in Table IV, water reactors are installed in sufficient capacity to maintain 35 percent water reactors, 65 percent fossil units, which was the ratio of existing units on the system in 1986. In the second pattern shown, breeder reactors are installed until they reach 35 percent of system capacity. Then water-reactor installations are alternated with breeders to maintain the breeder participation at 35 percent for the remainder of the expansion. The third pattern installs breeders until 65 percent of the total capacity is achieved, and so forth.

Results

Two generalized studies of breeder reactor economics have been performed on the foregoing system during the past two years. The first assumed a relatively low nuclear-power growth rate.[11] It concluded that with low-cost uranium, the optimum expansion pattern called for growth without limit in water reactors but restricted breeder participation to 35 percent of peak load.

The second study compared high-gain breeders with low-gain breeders and steam breeders for the more recent higher projections of nuclear power growth.[12] It also examined the sensitivity of the resultant levelized annual savings to variations in fuel costs. A partial summary of significant results is depicted in Figs. 5 and 6. Figure 5 compares water-reactor-only expansions with an all-fossil plant expansion. Two fossil-fuel costs, 19 and 23.7 cents/GJ, are examined. The results are shown in two ways, first as the present worth for each pattern and second as the equivalent 20-year levelized annual savings or penalty over the fossil-fuel pattern.

The first column represents the all-fossil-fuel base case. The next group of four columns shows that if U_3O_8 prices remain below $22 per kilogram, the optimum amount of water reactors is the maximum possible. General inflation in the economy would affect both capital and fuel costs. This factor has not been considered because many economic studies have shown that general inflation usually does not affect the economic choice between alternatives. However, if
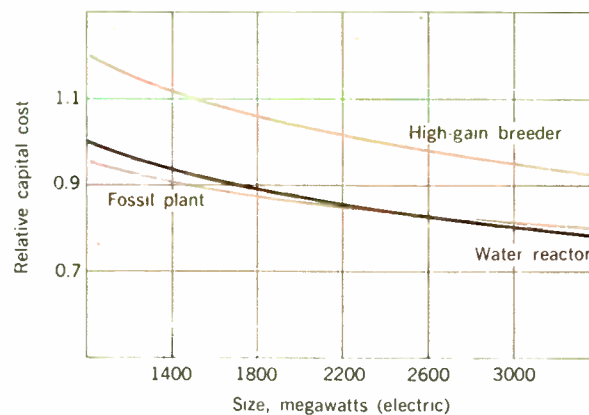
FIGURE 4. Capital cost of generating plant, excluding working capital for fuel inventory.

III. New-unit characteristics

Unit Size, MW	Fixed Operation and Maintenance Costs, millions of dollars per year			Full-Load Heat Rate, kJ/kWh		
	F	WR	BR	F	WR	BR
1000	0.710	0.960	1.160	9080	10 900	8810
1500	0.830	1.100	1.320	8900	10 840	8700
2000	0.910	1.210	1.460	8760	10 790	8590
2500	0.985	1.315	1.580	8600	10 750	8500
3000	1.045	1.405	1.685	8500	10 700	8440
3500	1.120	1.500	1.790	8350	10 680	8350

IV. Base-load unit additions for typical expansion patterns

Year	Size, MW	35% WR, 65% F	35% BR, 65% WR	65% BR, 35% WR	50% BR, 20% WR, 30% F
1986	1000	F	BR	BR	BR
1987	1100	WR	BR	BR	BR
1988	1100	F	BR	BR	BR
1989	1200	F	BR	BR	BR
1990	1300	WR	BR	BR	BR
1991	1400	F	BR	BR	BR
1992	1500	F	WR	BR	BR
1993	1600	WR	BR	BR	BR
1994	1700	F	WR	BR	BR
1995	1800	F	WR	BR	BR
1996	1900	WR	BR	BR	BR
1997	2100	F	WR	BR	BR
1998	2200	F	WR	BR	F
1999	2400	WR	BR	BR	BR
2000	2600	F	WR	BR	F
2001	2700	F	WR	WR	BR
2002	2900	WR	BR	BR	WR
2003	3100	F	WR	WR	F
2004	3300	F	WR	BR	BR
2005	3500	WR	BR	BR	WR
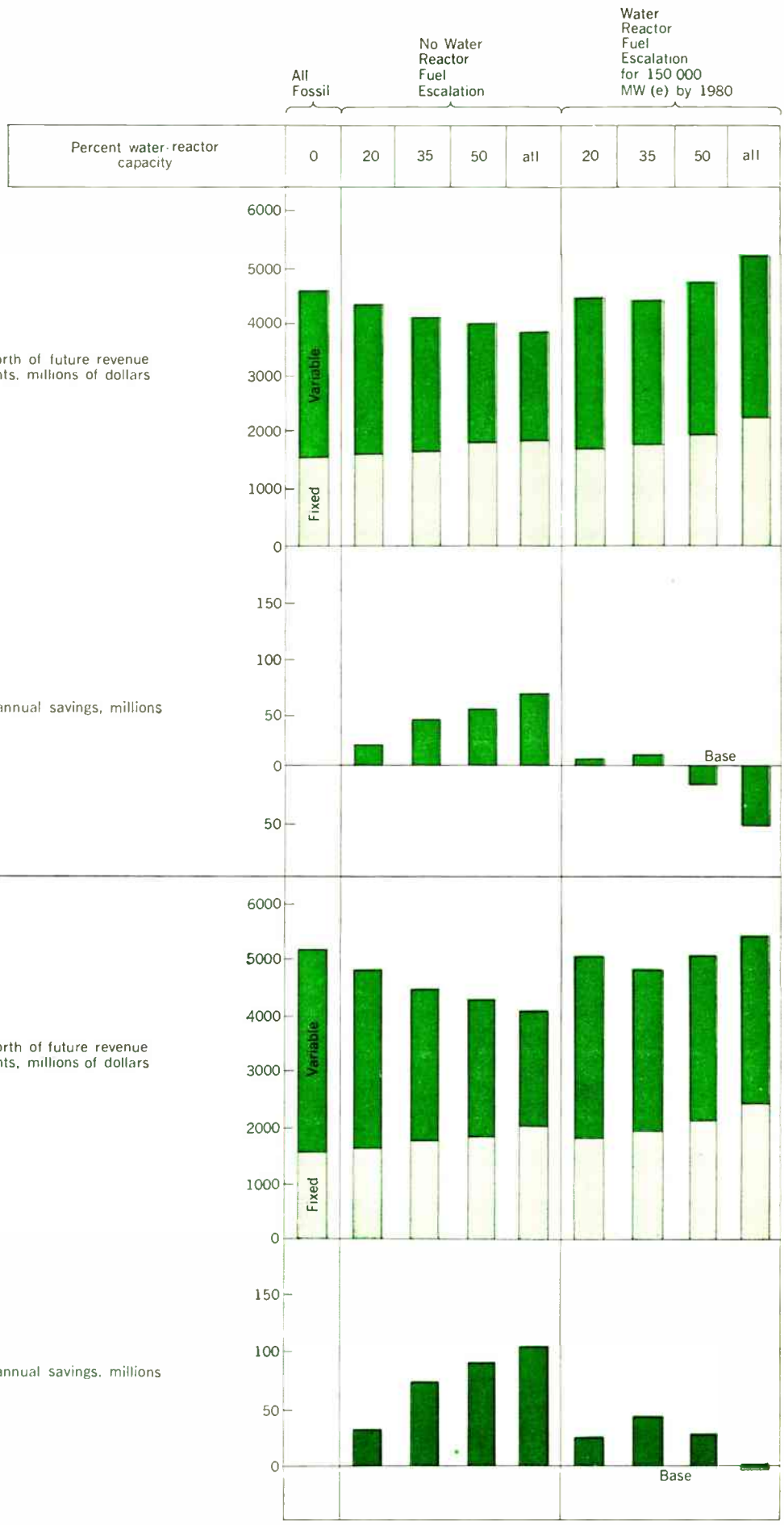
fuel costs escalate because of supply-and-demand considerations, then a difference can exist in choosing alternatives. The remaining four columns show what would happen in the event that ore costs increase. With escalating ore costs, the optimum water-reactor capacity is substantially less than the maximum possible. In fact, it comes out to be 35 percent for the period beyond 1986.

The lower half of Fig. 5 illustrates the same set

Percent breeder capacity	0	35	35	50	65	100
Percent water-reactor capacity	35	0	65	20	35	0

Levelized annual savings, millions of dollars, with fuel escalation

Base

Levelized annual savings, millions of dollars, with no fuel escalation

Base
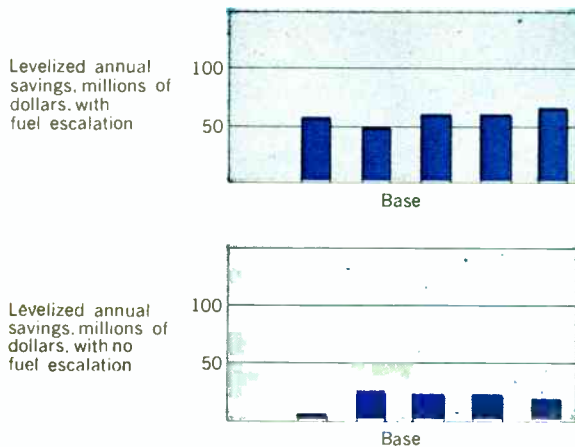
FIGURE 6. Economic advantages of high-gain breeder reactor.

FIGURE 7. Load-growth sensitivity.

Load-growth rate: 7%   5%   7%   5%

Expansion pattern: 35% breeder   50% breeder
                    65% fossil   20% water
                                     30% fossil

of conclusions for fossil fuel costing 23.7 cents/GJ. Of course, higher fossil-fuel cost assumption results in higher savings for the water-reactor expansions.

Breeder reactor savings. Figure 6 illustrates the additional equivalent levelized savings that result from including breeder reactors. Increasing ore costs were again used along with the 23.7 cents/GJ coal assumption for the results presented in the upper half of Fig. 6. Results shown in the lower half assume 23.7 cents/GJ coal but no escalation of nuclear fuel cost. A new b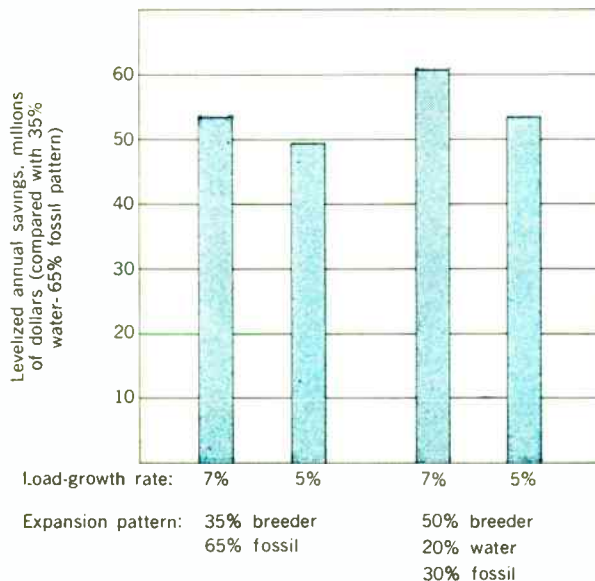ase pattern, 35 percent water reactors, is used. Thus the savings shown in Fig. 6 are savings attributed to breeder reactors only. Another interesting result shown by Fig. 6 is the relative lack of sensitivity of savings to the mix of units.

More recent study of this same system investigates the sensitivity of the levelized annual system savings to variations in the three most critical assumptions. These are load growth rate, breeder capital costs, and the value of plutonium as a breeder-reactor fuel.

Sensitivity to load growth. One of the uncertainties in forecasting nuclear reactor economics after 1985 is the growth rate of utility systems at that time. System growth may continue at something near the present 7 percent. On the other hand, what would be the effect if the system growth rate is only 5 percent? Figure 7 shows the effects of growth rate on levelized annual savings for the system with escalating ore costs and a coal cost of 23.7 cents/GJ. Patterns examined represent the 35 and 50 percent high-gain breeder participation. The patterns with high percentages of breeder units are more sensitive to load-growth reduction, as might be expected. However, the most important point is that breeder reactors still offer substantial savings even if the growth falls to 5 percent.

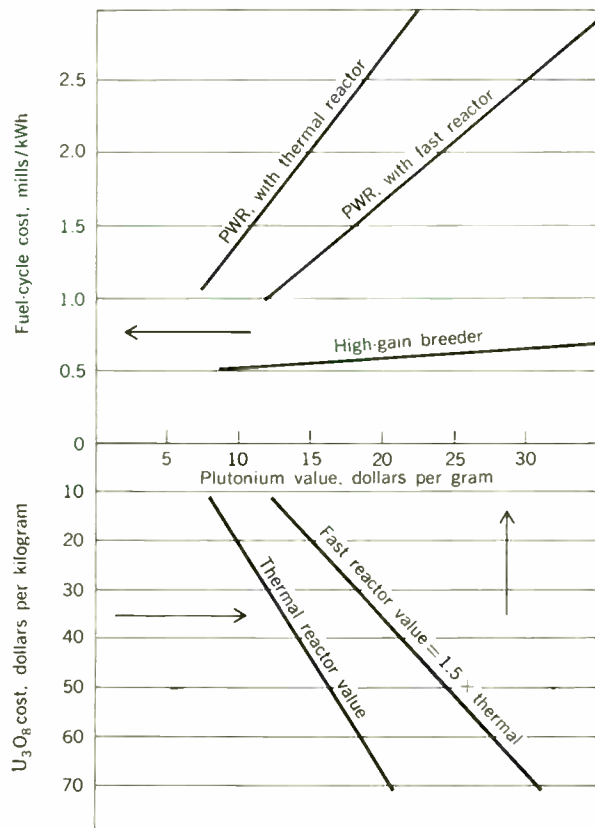FIGURE 8. Capital-cost sensitivity for various high-gain breeder-reactor patterns.

35% high-gain breeder

50% high-gain breeder

All high-gain breeder

1.3   1.4   1.5   1.6   1.7
Breeder capital cost
Water-reactor capital cost
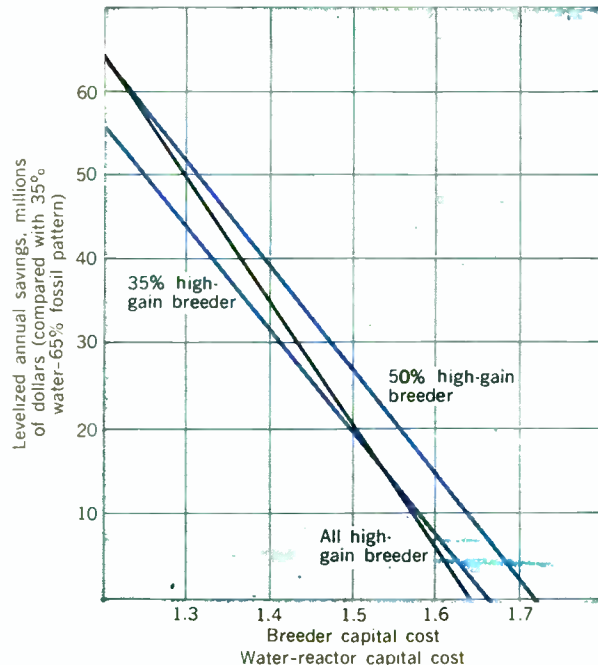
FIGURE 9. Effects of ore cost on total fuel-cycle cost for 1000-MW unit.

FIGURE 10. Sensitivity of plutonium value for various high-gain breeder patterns.

Sensitivity to capital cost. Figure 4 showed the relative capital cost assumptions for fossil plants, water reactors, and high-gain breeders. High-gain breeders were assumed to cost 20 percent more than water reactors. An important sensitivity analysis examines variations in the capital cost of breeders. How much more can a breeder reactor cost than a water reactor before projected savings from the fuel cycle vanish? Figure 8 presents the results of studies in which breeder plant capital costs were increased to the point where levelized annual savings are zero. Again, escalating ore costs and the higher coal cost are used. The curves plotted represent breeder participation of 35, 50, and 100 percent of all new base-load units added in the 20-year period beginning in 1986. The higher the percentage participation, the faster the savings disappear with increasing breeder capital costs. However, even with expansion patterns employing all breeder units, those units could cost up to 64 percent more than water reactors and still be the economic choice.

Sensitivity to plutonium value. Perhaps the greatest uncertainty is the value of plutonium recycled through breeder reactors. Although plutonium has yet to be introduced as the fissile material to maintain the chain reaction in large commercial reactors, experimental work has established a fair idea of its value as fuel for light-water reactors. However, the value of plutonium as fuel in the breeder reactor will be different because of better neutron utilization and better plant efficiency.
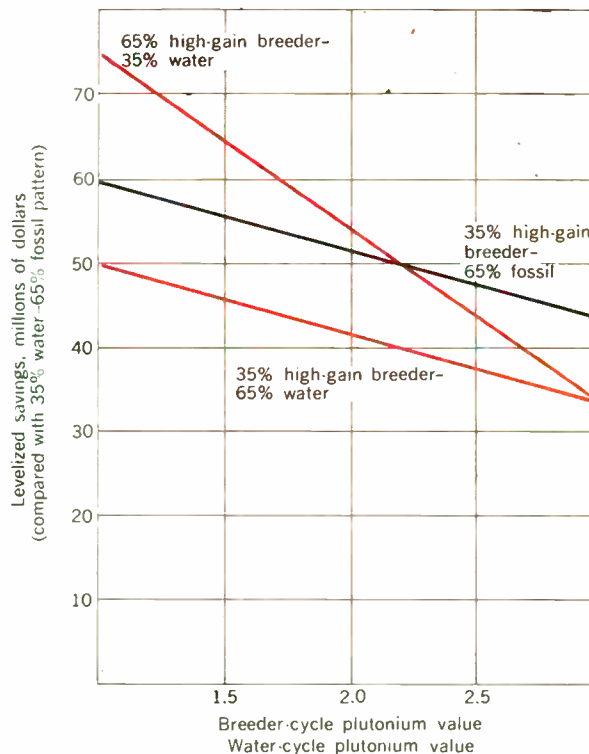
The breeder plant's variable fuel-cost component decreases with increasing value of plutonium because excess plutonium is produced as the plant generates kilowatthours. However, as the plutonium becomes more valuable, the cost of working capital to maintain the core inventory increases, and the fixed fuel-cycle-cost component increases more rapidly than the variable cost decreases. Hence, the total breeder fuel-cycle cost as a function of plutonium value has a small net positive slope, as shown in the upper half of Fig. 9. This is contrasted to the large positive slope shown for the water reactor's total fuel-cycle costs versus plutonium value.

The lower half of Fig. 9 shows that the plutonium value depends directly upon the basic cost of natural uranium ore (U_3O_8) and the reactor characteristics. The cost of separative work and the unique reactor fuel cycle determine the position and slope of these curves. The figure also shows how the fuel cost is affected by the value of plutonium in either an all-thermal or in a mixed thermal–breeder environment. Plutonium will generally be more valuable as breeders are introduced to use it. The curve assumes that the use of breeders will increase the value of plutonium by 50 percent. The arrows indicate how the reactor fuel-cycle costs are obtained in either environment for variations in basic ore cost. Previously, it was assumed that the value of plutonium in a breeder-reactor cycle is 1.5 times its value in a water reactor, as plotted in the lower part of Fig. 9. The exact relationship between ore cost and plutonium value for the breeder cycle depends on separative processes and characteristics of reactors yet to be designed and operated in

substantial numbers. For this reason, a sensitivity study was made of this relationship assuming escalating ore costs and a coal cost of 23.7 cents/GJ.

Figure 10 shows the levelized annual savings for several breeder patterns for variations in the ratio of plutonium value in the two cycles. The plutonium value for the breeder cycle has been assumed to go as high as 3.0 times its value in a water cycle. Today's realistic assumption is 1.5; but even at twice this figure, substantial savings from breeders are still evident. As the saturation of breeders in the pattern increases—for example, to 65 percent breeders—the savings decrease at a faster rate as plutonium value goes up. This is because of the higher fixed cost of the plutonium inventory in the breeder reactors. Nevertheless, the savings remain substantial for any realistic assumption of plutonium value.

One final comment is necessary on the sensitivity study of plutonium value. The only type of breeder plant considered is the high-gain breeder with its high specific power (1200 kW, thermal, per kilogram of fissile material) and its short compound doubling time (seven years). Previously, little economic advantage was shown from low-gain and steam breeder reactors, which have lower specific powers and longer doubling times. Since these other breeder types have higher specific inventories (kilograms of plutonium per megawatt of electrical output), they would be much more sensitive to increasing plutonium values.

Conclusion

Water reactors will continue to dominate nuclear expansion into the 1980s. Nevertheless, the high-gain fast breeder holds the greatest long-term promise. The economic advantages of the breeder reactor are substantial; the capital cost of breeders can be over 50 percent higher than water reactors and still be economic. Breeder-reactor advantages are not extremely sensitive to utility growth rates; substantial savings still exist for growth rates even as low as 5 percent. The relative cost of plutonium as fuel in the breeder compared with the water reactor can vary greatly without destroying the breeder's advantage.
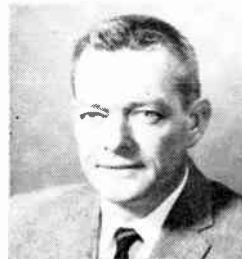
REFERENCES

1. 1967 Supplement to the 1962 Report to the President on Civilian Nuclear Power, p. 23, Feb. 1967.
2. Seaborg, G. T., "The new world," address presented at Rio de Janeiro, Brazil, July 3, 1967.
3. Dillard, J. K., and Baldwin, C. J., "Economic development of mine-mouth power plants, EHV transmission, and nuclear generation in the United States," Paper 78, 1964 World Power Conference, Lausanne, Switzerland.
4. Johnson, W. E., "Nuclear power and the Northwest," remarks before the Washington Public Utility District's Association, Seattle, Wash., Dec. 8, 1966.
5. Seaborg, G. T., "Fast-breeder power reactors—a world outlook," address presented at Montreal, Que., Canada, May 31, 1967.
6. Simpson, J. W., remarks at the 1966 Annual Meeting of the Association of Edison Illuminating Companies.
7. Lane, J. A., "Economics of nuclear power," U.S. Army Nuclear Science Seminar, Oak Ridge, Tenn., July 18 1967.
8. "Uranium drilling topping 1957 record; more in sight for 1968–69," Nucleonics Week, vol. 8, Aug. 24, 1967.
9. Dillard, J. K., and Baldwin, C. J., "System simulation," Westinghouse Engr., vol. 20, pp. 130–135, Sept. 1960.
10. Jeynes, P. H., and Baldwin, C. J., "Financial concepts for economic studies," Westinghouse Engr., vol. 24, pp. 8–47, Mar. 1964.
11. Nordman, D. A., Smith, E. E., and Wright, J. H., "Application of advanced nuclear reactors to utility systems," presented at the American Nuclear Society Summer Meeting, June 1966.
12. Wright, J. H., Smith, E. E., and Nordman, D. A., "The economic impact of breeder reactors on utility systems," Proc. Am. Power Conf., 1967.

J. K. Dillard (F) received the B.S.E.E. degree from the Georgia Institute of Technology and the M. S. degree from the Massachusetts Institute of Technology. He served on the staff of the Electrical Engineering Department at M.I.T. before joining Westinghouse in 1950. His first assignment was in the Electric Utility Engineering Department, where he dealt with system studies of surge protection, transient phenomena, circuit analysis, and economic dispatch. As manager of the department since 1956, he is responsible for the engineering relationship of Westinghouse with electric power companies all over the world, and for technical and economic investigations, looking 10 to 15 years into the future. Major programs currently under his direction include the Apple Grove EHV Test Project, involving transmission voltages up to 750 kV; the Waltz Mill 1100-kV Project on research in underground transmission; and computer applications to power systems.

C. J. Baldwin (F) is an electrical engineering graduate of the University of Texas and M.I.T. He has been with the Electric Utility Headquarters of Westinghouse since 1952. As a sponsor engineer he dealt with system engineering problems of utilities in the Ohio River Valley area. Later he headed a team that developed new techniques for system planning by digital simulation. Since then these methods have been applied by Westinghouse to the planning problems of utilities representing 40 percent of the installed kilowatt capacity in the United States. In 1961 he was chosen as the outstanding young electrical engineer in the nation by Eta Kappa Nu. At Westinghouse he is manager of development, advanced systems technology, and in this capacity he directs consulting work for utility customers and development projects in generation, transmission, and distribution system engineering.

N. H. Woodley (SM) received the B.S. and M.S. degrees in electrical engineering from Iowa State University, where he also taught courses in circuits and machines. He also taught electronics for two years at the U.S. Army Defense School. As development engineer, advanced systems technology, at Westinghouse, his responsibilities include the development of digital computer techniques for application to electric utility long-range generation planning. He is also active in developing digital simulation methods for applications related to long-range distribution system planning and reliability analysis.
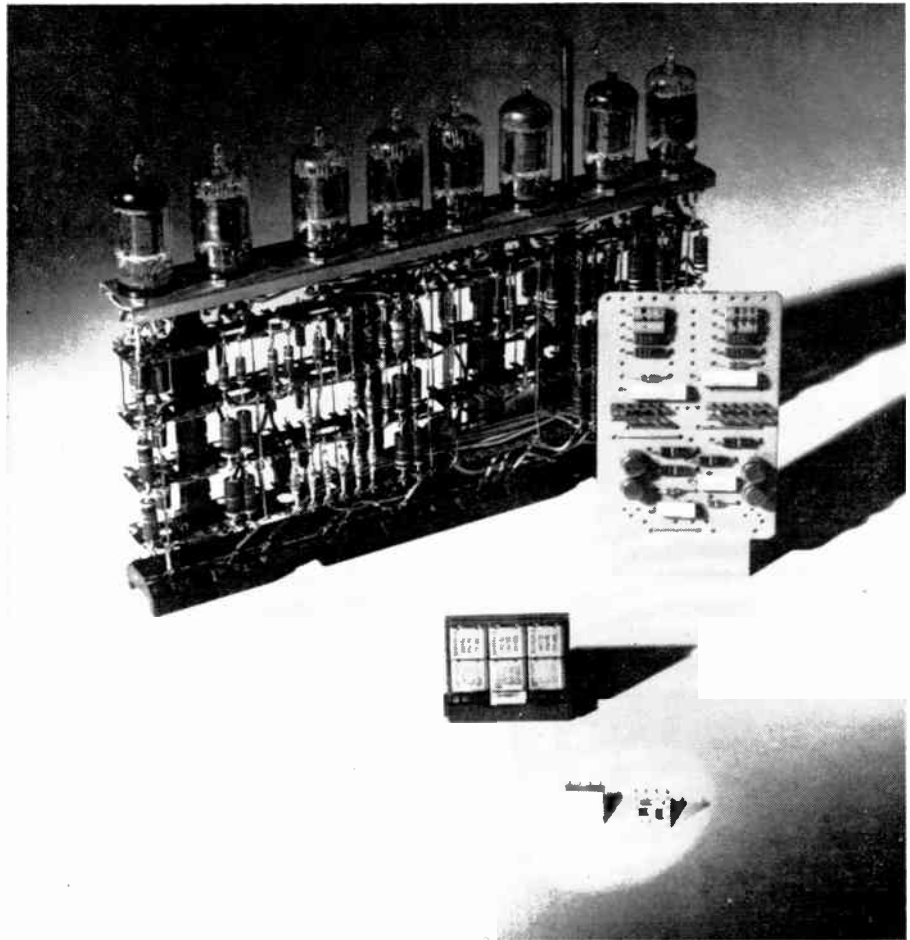
FIGURE 1. Illustration of the miniaturization in computer components and circuitry over the past 15 years.

FIGURE 2. The superposition of paramecia, one of nature's smallest "animals," shows the small size of the newest circuits.

25 μm

Christ, Ramsey—Analysis tools for microminiaturized circuits
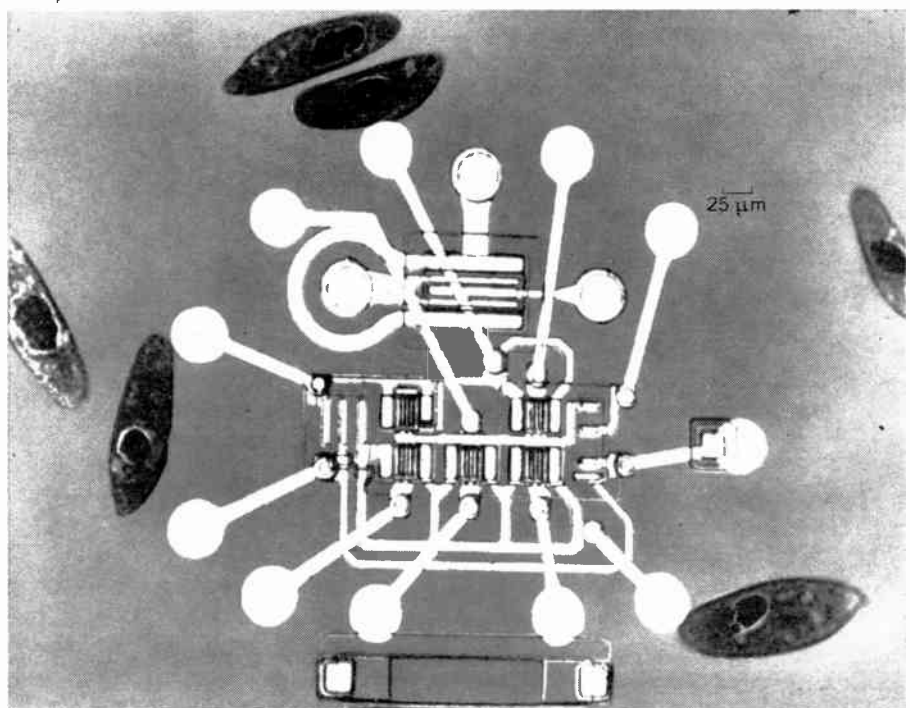
Analysis tools for microminiaturized circuits

Advanced techniques of X-ray and electron optics are proving to be among the most useful of the new analytical methods developed to meet the stringent design requirements of microminiature assemblies

J. G. Christ, J. N. Ramsey *International Business Machines Corporation*

This article points out the need for new instrumental methods to cope with the present requirements of material and structure analysis and characterization of microminiaturized circuits. Primarily, it describes briefly a few principal instruments and techniques utilized in such analysis and characterization, and it discusses some materials used in microminiaturized semiconductor assemblies, especially silicon and the contact metallurgy, and methods for obtaining information concerning its structure and chemistry. Since the entire gamut of metallographic and chemical techniques cannot be covered here, the article is limited to the X-ray and electron optics methods used in semiconductor and interconnection studies.

We probably know more about silicon than about any other material. This is the prerequisite upon which the new semiconductor industry is built. Dr. Vannevar Bush is quoted as saying that the electron tube was discovered by tinkerers whereas the transistor is the direct result of modern science.[1] By a lucky accident Faraday or Crookes could have deduced the principle of the electron tube while working on electric discharges in a vacuum, but the transistor is the direct offspring of 20th century solid-state physics and quantum mechanics.

Silicon for modern electronic uses must be as structurally stress-free and as chemically pure as we can make it, or must have a well-controlled doping level. Much progress has been made toward attaining these goals. And there has been equivalent success in the achievement of sophisticated scientific methods for the measurement of materials improvement.

The computers on the market today are essentially third generation. Their switching time has decreased from microseconds in the 1950s to nanoseconds in the 1960s as the result of the development of higher-frequency devices and of packaging techniques with lower losses at higher frequencies, which allow the effective use of the newer devices. The limiting factor has become the delay and losses in lead lengths. Figure 1 illustrates this progression from vacuum tube to transistors and other circuit components on printed circuit boards or cards, to individual circuits of transistors and circuit components on individual modules mounted on printed circuit boards or cards.

The next logical step was to put an entire circuit on a silicon chip, which was followed by multiple circuits, and then families of circuits. This utilization of the "real estate" on the silicon chip, with its shallower transistors and short lengths allowing higher switching speeds, is illustrated in Fig. 2. The five transistors in the lower center have five interdigited fingers, each 2 μm in width and spaced 2 μm apart, and the transistor at top center is essentially of present SLT size. The dark objects are paramecia, which are among the smallest forms of animal life.[2]

The form factors of today's and tomorrow's devices —high doping levels, shallow junctions, thin insulating films, multilayer circuitry, narrow bands and spacings, high packing densities, and the need for high yields and near-"infinite" reliability—put great demands on the materials and their processing. The current densities, the potential gradients, the low leakage current, and the high-frequency loss tolerances in smaller and smaller regions of material have led to the need for a degree of homogeneity, uniformity, and freedom from defects that has not been encountered previously. In fact, in spite of its extensive improvement during the last decade or so, the present material is not as satisfactory for today's microcircuit requirements as the material of the '50s was for the discrete devices of that day. The semiconductor industry, particularly the computer segment, is demanding more of materials than anyone else except for the rocket-engine technologists who require such high strength at high temperatures. This, in turn, puts great demands on the materials analyst, who must provide full and precise characterizations of composition, structure, and properties of micrometer-sized regions, regions that may be very thin, and even buried. The solution requires extensive concept and technique development, since yesterday's tools will not do tomorrow's jobs.

Some useful techniques

The electron microscope has been used effectively to probe the structure, and indirectly the chemistry, of silicon crystals. There is a strong correspondence between light optics and electron optics in microscopy but, instead of a light source, there is an electron source (electron gun) to provide both the electrons and the energy (40–100 keV, usually). Magnetic condensers and objective and projector lens provide the

effective optics for the electrons. The visible-light-wave range is roughly 4000–7000 Å, with a limiting resolution of less than 10^{-4} cm. The wavelength of electrons of 100 kV is about 0.037 Å, giving a theoretical limiting resolution of about 2 Å.

Figure 3 shows two variations of the nondestructive replication technique utilizing carbon films. In each case, the specimen surface to be examined is coated with a thin film of highly diluted organic, such as collodion or Formvar. This liquid must have a low enough surface tension to enable it to flow into every nook and cranny to replicate faithfully every topographic feature, and yet the material must have sufficient strength when dry to prevent stretching and tearing as

the replica is carefully stripped off the specimen. To provide support during the stripping, subsequent processing, and examination by electron microscope, a metal grid is preplaced on the specimen and becomes embedded in the plastic, the surface of which has replicated the specimen. This first-stage replica could be examined by electron microscope, but it might deform upon being heated; thus a second-stage replica is made by evaporating a 200–400 Å layer of carbon directly onto the first-stage replica. The plastic is then dissolved, allowing the carbon replica to attach itself to the metal grid. However, the small difference in replica thickness allows for practically no contrast and so a thin film of "heavy" metal, such as chromium, germanium, or platinum, is deposited from a shallow angle that will highlight one side of the hills. The principal contrast will be between the opaque areas of the "heavy" metal, and, with experience, even complex electron micrographs can be interpreted.

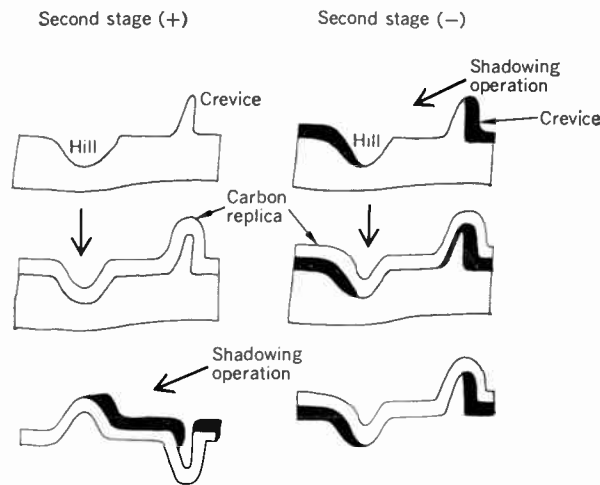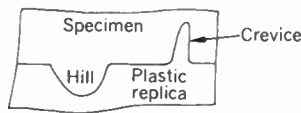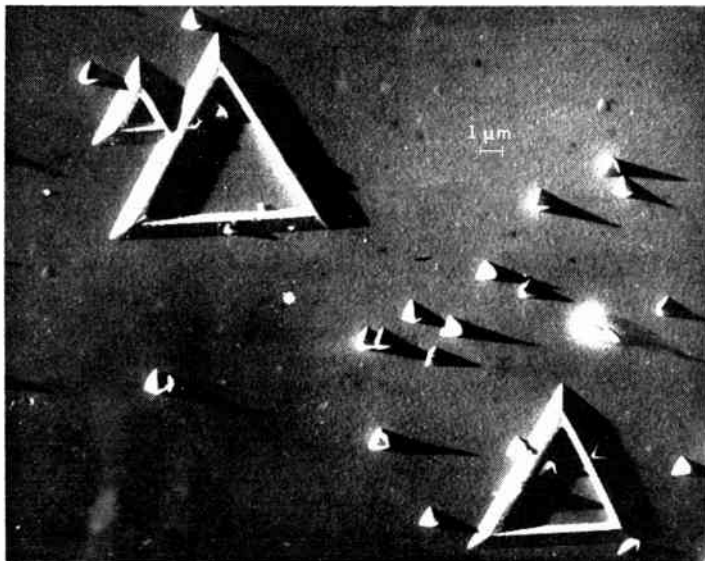By varying the sequence, contrast of different struc-

FIGURE 3. Steps in replication technique as samples for electron microscopy examination.

FIGURE 4. Example of stalking faults on an etched silicon surface.

FIGURE 5. Example of good and bad sputtered SiO$_2$, as shown by negative replication before and after progressively longer etch times.
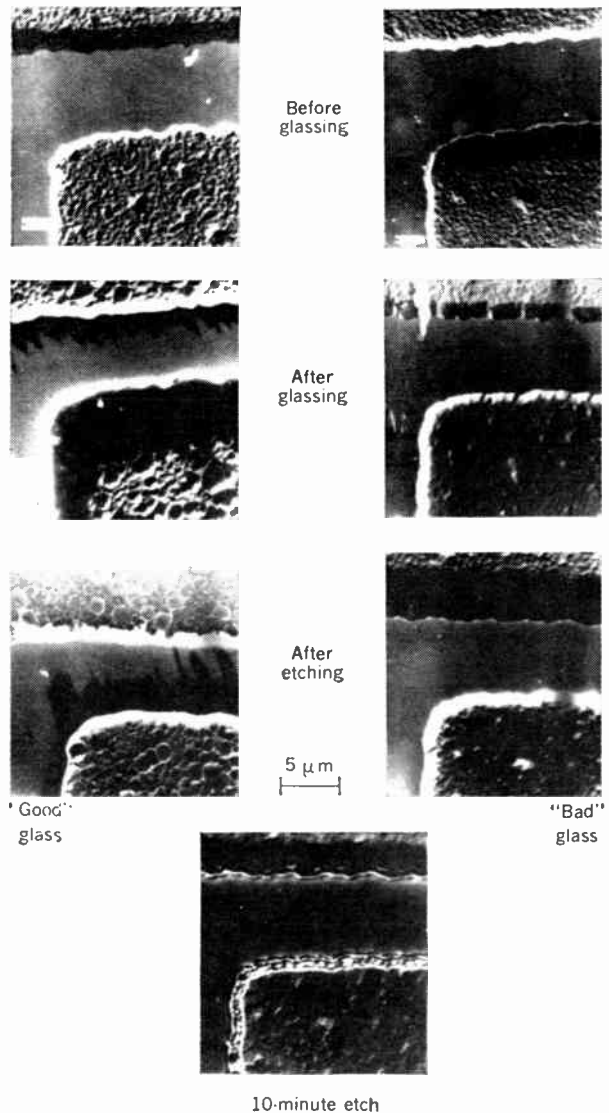
tural features can be enhanced. The "positive" replica, with the carbon film made prior to shadowing, enhances hills but may miss crevices, as shown in Fig. 3. (This replica is called positive because, on the micrographs, hills look like hills and valleys look like valleys; i.e., there is a one-to-one correspondence.) If the shadowing is done prior to the carbon film, the crevices are enhanced markedly. (This is called negative because hills look like valleys and valleys like hills.) These techniques provide resolutions to about 35–50 Å, when the "structure" of the carbon film becomes "visible." Figure 4 is a negative replica of an etched silicon epitaxial film that was grown over a mechanically polished silicon wafer. This was part of a study of the origin of defects in epitaxial films. The small triangles are etch pits and the larger open triangles are stacking faults. The varying size of the stacking faults implies that they were nucleated at different levels in the epitaxy film because they would all be the same size if they had grown from the original silicon surface.

In studying changes that occur during processing, one can obtain much more information by microanalysis if he examines the same area successively. An example of this is seen in Fig. 5, in which the RF sputtered glass produced under "bad" conditions (left) is compared with that from "good" conditions (center and right).[3] The top row shows negative replicas of the surfaces of the devices prior to glassing; the next row shows the same regions after glassing. The bad glass has a crevice at the step over the stripe and the replicating plastic therefore has spikes that, when shadowed, produce excellent resolution of the crevices. The "good" glass on the right has none. The bottom row shows the glass after 15 seconds of etch in 7:1 buffered high frequency and the crevices in the "bad" glass are seen to be deeper. Note that the shadow direction was altered and the shadows are well-defined only on the smooth surface between the lands, even though the crevices evident after the first etch are still there after the second etch. The "good" glass did not develop crevices even after ten minutes in the etch, as

seen in the single frame on the far right.

An interesting adjunct to this technique, called extraction replication,[4] has been adapted to semiconductor devices.[5] As indicated by Fig. 3, anything removable from the original specimen surface would be pulled off with the plastic replica (in fact, one way of getting a clean surface for laboratory uses is to strip it with a collodion film). Hopefully, this material will survive through processing and end up in the carbon replica. The material may be a relatively loose corrosion product, but often it is adherent, or an inclusion, or a second phase whose identity is required. In these latter cases we must use micro "earth-moving" techniques under the microscope—scraping or crushing with a microhardness indentor or ultrasonic hammering with needles or single crystals of micrometer dimensions.

Figure 6 shows a relatively loose corrosion product on a transistor and the replica (on the grid) with the corrosion product carried over. The topography of the transistor provides location identification. Electron diffraction was done in the electron microscope for identification of the corrosion product, and the microprobe analysis was done on the replica for corroboration.
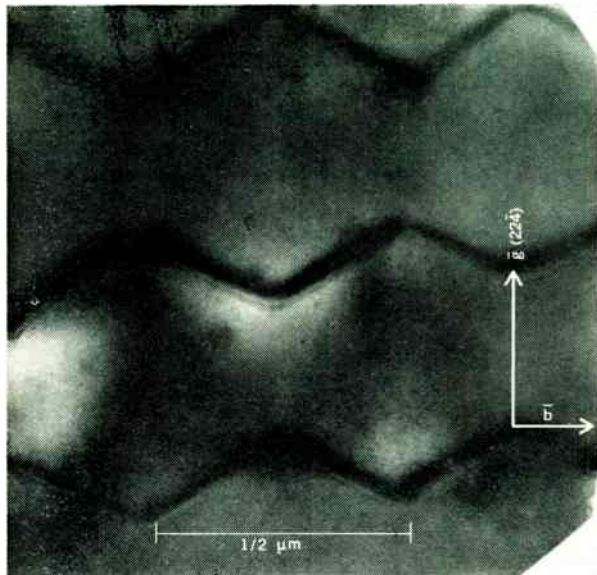
Much more information can be obtained if the silicon or other materials are examined directly. This is accomplished by first etching the silicon wafer to thin down its cross section to approximately 6000–8000 Å. Known as transmission electron microscopy, this technique has been useful in metallurgical studies such as crystal growing, diffusion, oxidation, and contact metallurgy. Whereas the replica electron microscope pictures are really shadow graphs, the transmission electron microscope pictures are electron diffraction pictures of the traversed silicon cross section, as illustrated in the phosphorus-doped section shown in Fig. 7. Four sides of the hexagonal-shaped dislocation network are shown, the other two parallel sides being incorrectly aligned for diffraction contrast. If the orientation of the sample is changed properly, the two missing lines can be seen and another two will be missing.[6]

FIGURE 6. At right is a relatively loose corrosion product extracted by the replica extraction method. At left is the transistor from which it was extracted.

├──┤
30 µm

Use of X rays

X rays are used in structure and chemical analysis in three ways. The oldest application is radiography, dating back some 75 years to just after the discovery of X rays, when Becquerel found shadows on a film fogged by uranium potassium sulfate. A refinement of the technique is X-ray microradiography, which is now being applied to reveal minute solder voids, discontinuities, and cracks in hybrid circuit assemblies.[7] A second, extensive use is based on the secondary X-ray emission by all materials upon bombardment by X rays with greater energy than that of their characteristic X rays. The third method, X-ray diffraction, has been widely used for structure analysis. This technique has probably added the most experimental information to our understanding of the way nature uses its atomic blocks in the building of the material universe.

In X-ray diffraction the X rays impinging upon a material excite the atomic electrons and cause radiation of the same wavelength as the X rays from all of the uniformly located atoms composing the material structure. According to Bragg's law, the resultant waves are either enhanced or canceled, depending upon the geometry. This results in definite patterns from which much can be determined, for example, lattice parameters, presence of strains, degree of alloying, and so on.

Dr. G. H. Schwuttke recently extended the Berg–Barrett method so that X-ray diffraction topographs can be made of whole wafers.[8] His technique is shown in Fig. 8. The monochromatic X-ray source is at left. Next is a series of slits for collimating the beam, followed by the crystal, an aperture, and the photographic film, the last of which is oscillating with the crystal as the center point. Also, the crystal and film are simultaneously moving past the stationary X-ray beam and screen. In this way, the X-ray slit or line scans and the film simultaneously record the crystal-diffracted beam on the film. Schwuttke's method is the first to show successfully the X-ray diffraction structure of the
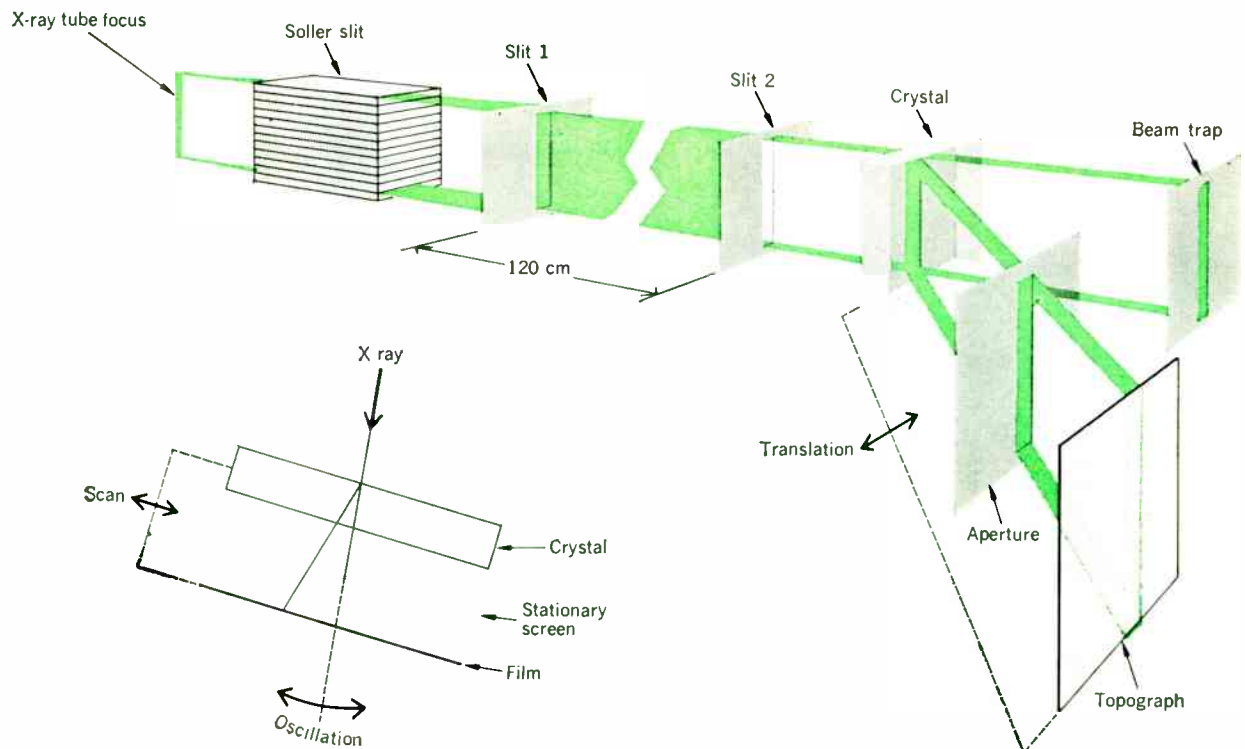

FIGURE 7. Phosphorous-doped silicon section. Note the dislocations that are formed and the absence, because of diffraction, of the completion of the hexagonal. Proper adjustment will bring the two missing lines in and another two out.

FIGURE 8. Schwuttke's X-ray diffraction technique, which enables examination of a whole wafer

entire wafer. Figure 9 presents a Schwuttke oscillating topograph of a nearly perfect wafer after the initial oxidation.[9] Unfortunately, the markings on the back of the wafer have caused considerable damage. Figure 10 shows a topograph of the same wafer after the subcollector reoxidation. Note the extension of the damage area.

Figure 11 is the same wafer after emitter diffusion. Damage area continues to increase. Note also the new area of damage around the periphery, especially at the location marker. Figure 12 shows the yield map superimposed on the previous illustration. Most of the bad devices coincide with the damaged areas in the wafer. This dramatically points up the need for care in handling the wafer during the entire processing cycle.

Scanning electron microscope and microprobe

One of the most versatile modern tools for the micro study of materials is the electron microprobe, as first reported by Castaing and Guinier in 1949.[10,11] A more recent offshoot is the scanning electron microscope (SEM). As in the electron microscope, an electron gun provides both the electrons and the needed acceleration potential for the electrons. In both instruments, there are magnetic lenses to reduce the beam size to a fraction of a micrometer for the microprobe and as low as 200 A for the SEM.

There are also two sets of deflecting plates or coils that are synchronized with the deflection plates or coils of the oscilloscope. The signals from the various pickups can be either plotted or used to modulate the grid
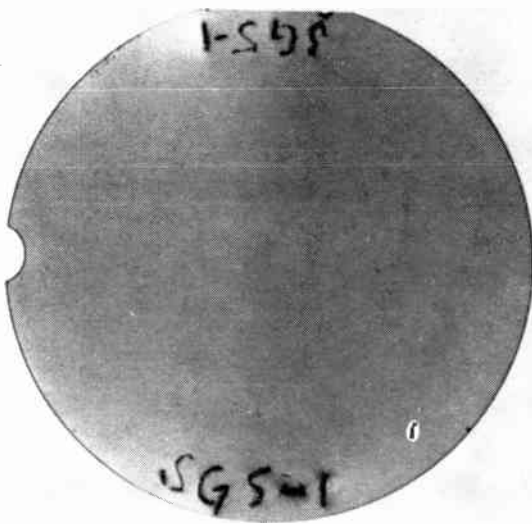

FIGURE 9. Oscillating topograph of zero dislocation silicon wafer (except for markings) after initial oxidation.
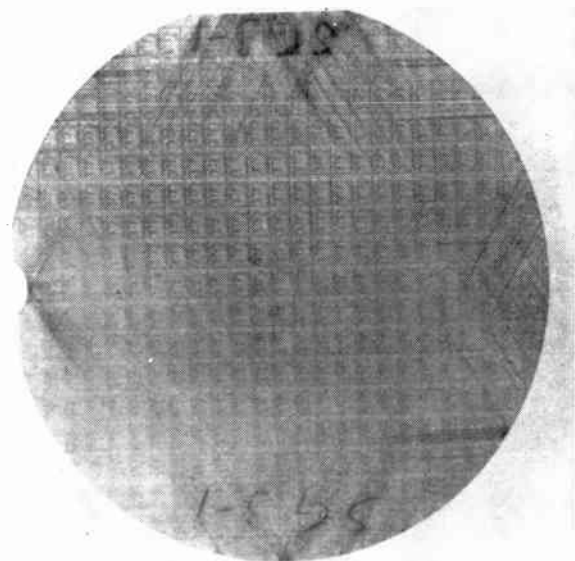
FIGURE 10. Oscillating topograph of the wafer shown in Fig. 9 after subcollector reoxidation.

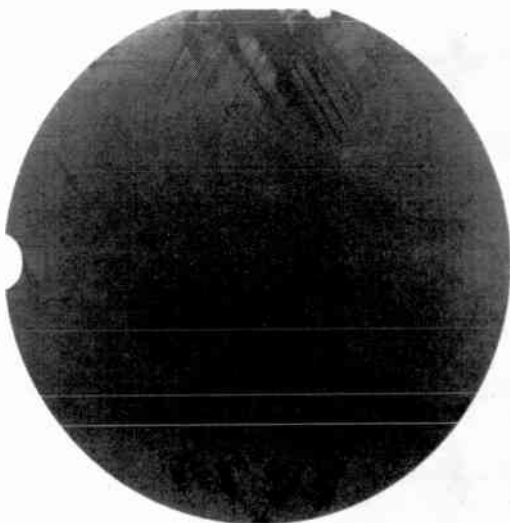FIGURE 11. Oscillating topograph of same wafer after emitter diffusion.

FIGURE 12. Oscillating topograph of Fig. 11 with yield map superimposed.

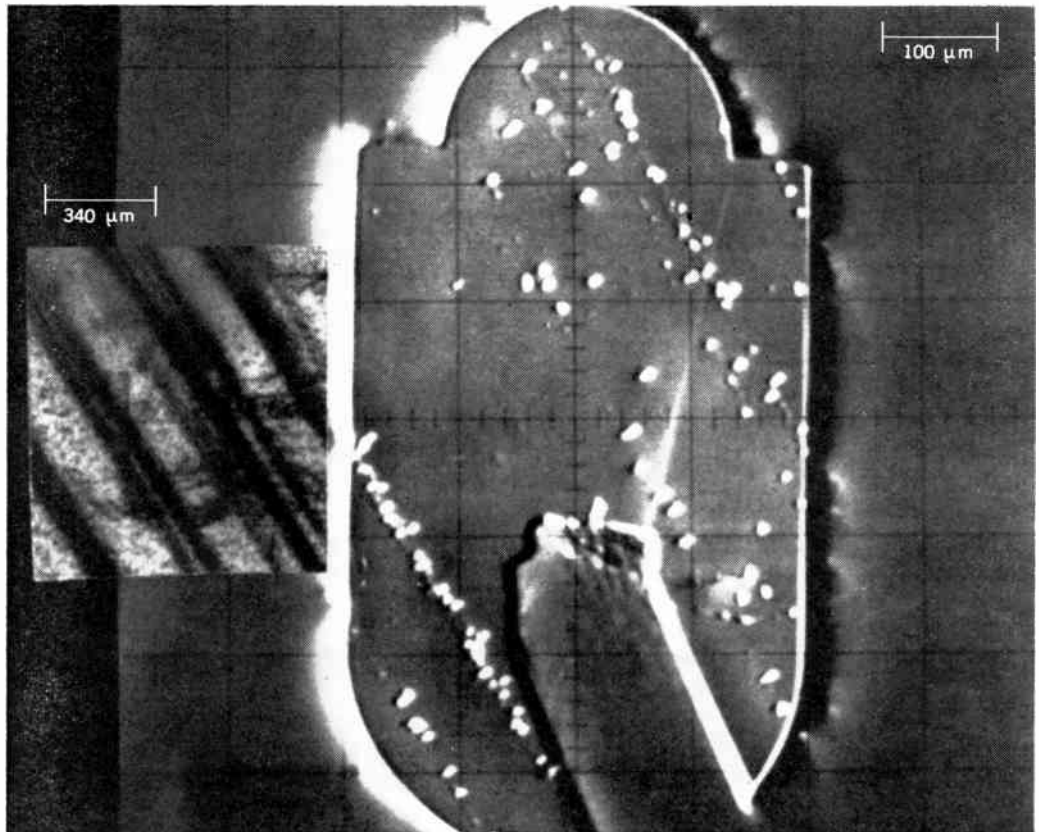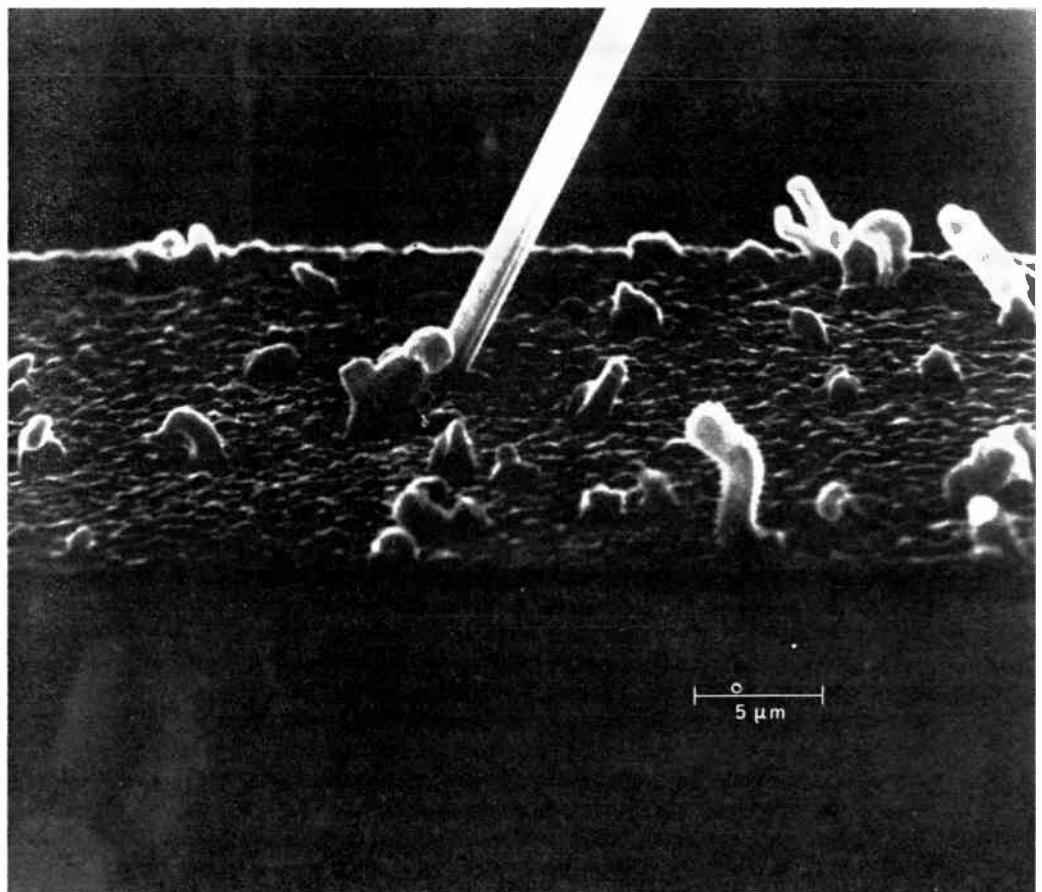Christ, Ramsey—Analysis tools for microminiaturized circuits

113
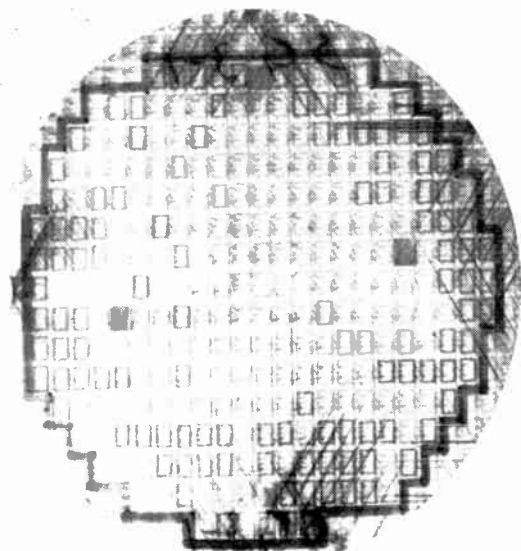
FIGURE 13. Comparison of enlargement of the wafer shown in Fig. 11 (left) and SEM current mode picture of a similar area (right).

FIGURE 14. SEM growth of spike in aluminum under high-current stress testing.
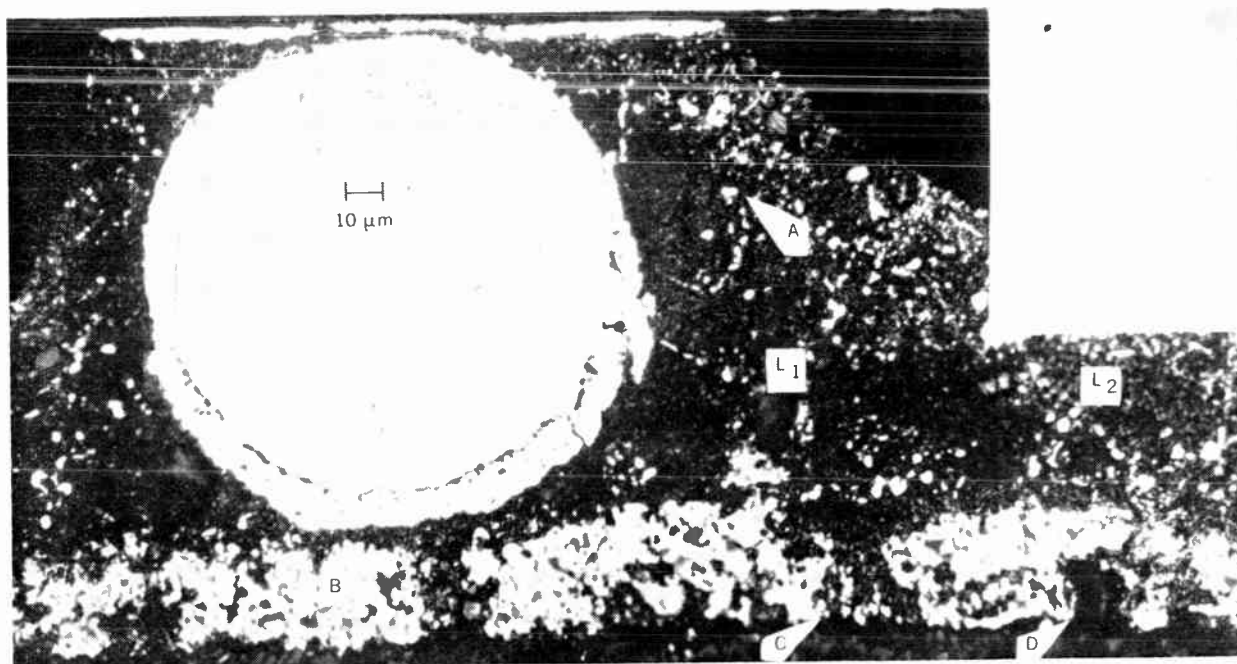
FIGURE 15. Micrograph of a cross section of the solder joint between a silicon chip (top) and alumina substrate (bottom).

of the cathode-ray tube in the oscilloscope.

One of the effects of the electron beam in semiconductors is the formation of electron–hole pairs that can be swept to a junction if they are formed within a diffusion length of it, and measured as beam-induced current (BIC). Anything affecting the formation or collection of the new carriers formed by the beam will give variations in BIC and may be interpreted. A good example is a follow-up study of the series of X-ray topographs of Figs. 9–12. The left side of Fig. 13, an enlargement of a portion of Fig. 11, indicates lines of dislocations crossing a diffused area but no resolution of individual dislocations. The right side of Fig. 13 shows the video scan on the face of the oscilloscope (note the graticule lines) using the BIC mode of pickup. The rows of individual dislocations correspond to the lines by X-ray topography inside the diffused region. Nothing is seen outside the diffused region because no junction exists. This is also a good example of the application of complementary techniques providing more than just the summation of the individual parts, because transmission electron microscopy also provides valuable information on the nature and growth of the dislocations.

Another pickup mode of scanning electron microscopy is that of secondary electrons. The number of secondaries produced as the beam impinges is a function of the local angle of impingement of the beam. Thus the secondary electron readout mode shows the topography of the specimen.

A dramatic example of the three-dimensional character possible with secondary electrons is shown in Fig. 14, which illustrates the growth figures sometimes formed by migration in thin films under current densities of several million amperes per square centimeter.

Another electron-beam material interaction is the Rutherford scattering of electrons by the nuclei of the atoms. The higher the atomic number, the higher the probability of such scattering backout of the specimen, its pickup by a backscatter detector, and its brightening on the screen of the cathode-ray tube. However, topographical factors can affect the number of backscattered electrons also, because, for example, holes in the specimen will act like Faraday cages and trap electrons to decrease the intensity on the cathode-ray tube. Thus interpretation is required to separate the atomic number and topography effects, but the backscattered electrons are useful for locating particular regions of interest within the specimen, especially small regions.[12]

The electrons in the beam, if of sufficient energy, can also knock out inner electrons from the atoms in the specimen, and as electrons from outer shells cascade down the "energy ladder" to produce X rays characteristic of the atoms. If X-ray analyzers are used, the elements can be identified, measured, and plotted in video scans as seen with electrons. An electron probe microanalyzer, commonly called a microprobe, can provide a chemical analysis, as in X-ray spectroscopy, on regions a micrometer or smaller in size, as discussed by Birks.[13]

Structure and chemical analyses

The microprobe is invaluable in solving materials problems in microminiaturization. Figure 15 shows a light micrograph of a cross section of an interconnection system for microelectronics. Just off the top of the illustration is the silicon chip with multilayer thin-film metallurgy to which a gold-plated copper ball is soldered. This has been joined by soldering to a pretinned metallic paste, bonded to an alumina module, and has
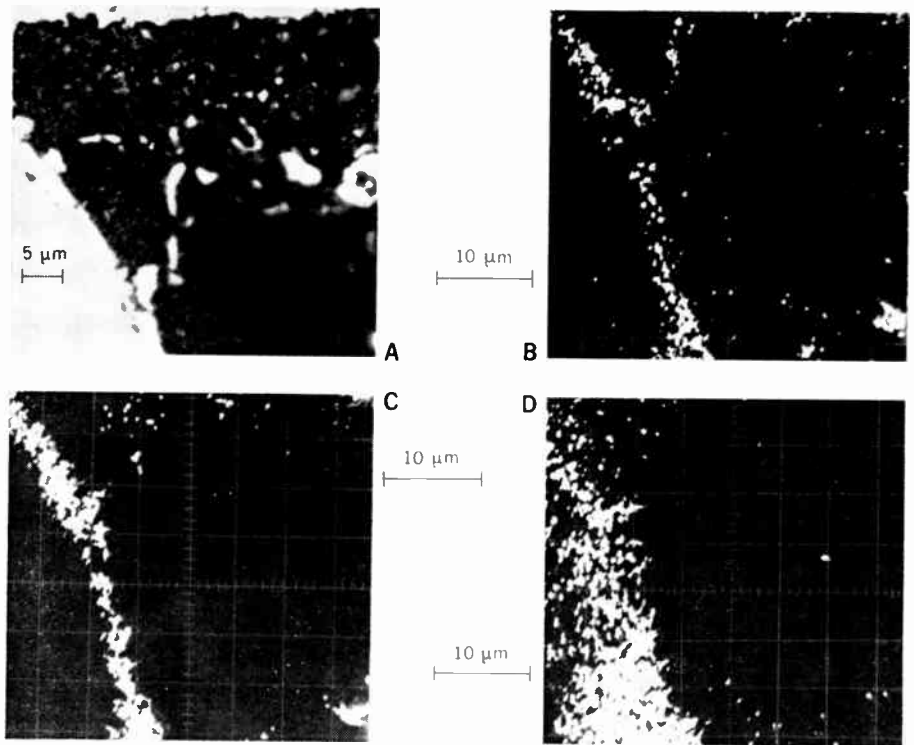
FIGURE 16. Enlargement of Fig. 15. A—Light micrograph of upper-right-hand section of Fig. 15. B, C, D—Au, Sn. and Cu, respectively, X-ray maps of same section.

FIGURE 17. Enlargement of Fig. 15. A—Light micrograph of (B) of Fig. 15. B—Back-scattered electron micrograph of same area. C–H—X-ray maps of Cu, Au, Sn, Pb, Pt, and Bi, respectively, of same area.
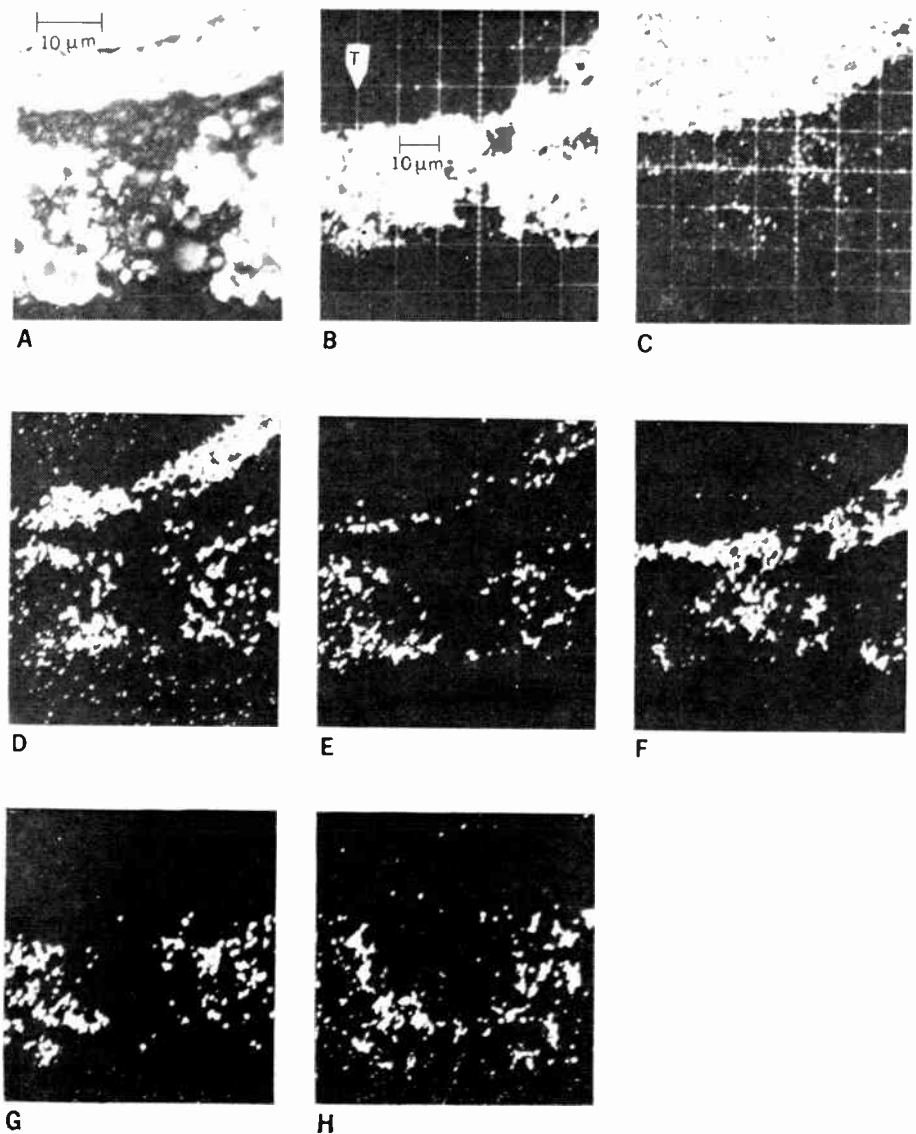
pins to attach it to printed circuit boards. It will be noted that the solder contains considerable intermetallic (A) after the particularly severe tinning and joining procedure this specimen underwent. It is desirable to know what intermetallics are formed and to see if there is a relationship to the marked inhomogeneities in the paste (B, C, D). These questions would be difficult to answer through the use of other techniques but are valid when the microprobe is employed.

Figure 16(A) is an enlargement of the upper-right-hand side of the gold-plated copper ball of Fig. 15. The primary question was whether the intermetallic in the solder was Cu-Sn spalling from the ball. Figures 16(B), (C), and (D) are video scans of the area, made by adjusting the spectrometers successively for gold, tin, and copper radiation, and putting the signals through preamplifiers, amplifiers, and a pulse height analyzer, and onto the grid of a storage oscilloscope to modulate the intensity.[14] The presence of an element is indicated by a white region. The set of intermetallics in the center and right of Fig. 16 is seen by correspondence in (B) and (C) to be gold and tin, without copper; thus, even though the intermetallic on the ball is Cu-Au-Sn, the intermetallic in the solder is independent of it.

Figure 17 shows an enlargement of region B in the paste in Fig. 15 together with video scans of back-scattered electrons, copper, gold, tin, lead, platinum, and bismuth. The discontinuity, as suspected metallographically, is seen in Fig. 17(F) to be lead from the solder but is essentially tin-free. It appears that the tin is alloyed with the Cu-Au-Sn on the ball and the platinum and gold in the paste. A direct correspondence is difficult at this magnification and so a traverse was run along the "T" arrow in Fig. 17(B) (by moving the stage under the beam). In this case, the several traverses were keyed laterally by repeating the tin signal each time. Of primary interest here is that six elements can be examined and their curves superimposed by location so that alloying and non-alloying can be seen; for example, the tin is alloyed

with the gold and platinum. The Bi_2O_3 glassy phase in the paste, used for bonding to the alumina, does not enter into the alloying, for, where the bismuth is rich, there is no tin (and hence no gold or palladium). This information is important in process optimization and control required for maximizing product performance and reliability.

Further data can be obtained with a new technique,[15] which is illustrated in Figs. 18–20.

Figure 18 shows the increase in phosphorous X rays resulting from a thin phosphosilicate glass (PSG) layer as the accelerating voltage of the electron beam is increased. Below about 2 kV, no $PK\alpha$ X rays are seen, because this is below the critical excitation potential mentioned earlier. But as the voltage is increased, the counts increase and the penetration increases to a maximum at V_3, beyond which more electrons are
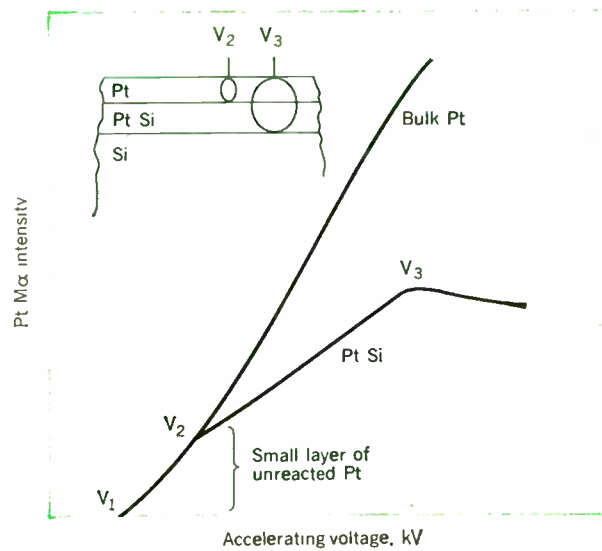
FIGURE 19. Graph showing change in slope with change from free Pt to PtSi intermetallic compound with accelerating electron beam voltage.

FIGURE 18. Graph of increasing electron beam voltage vs. $K\alpha$ X-ray intensities for phosphorus.
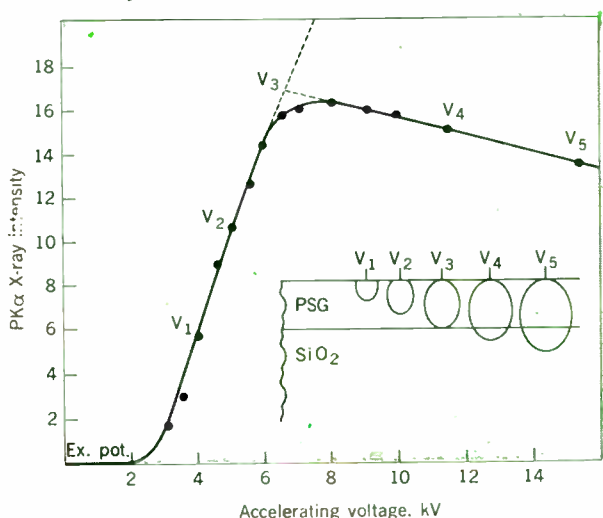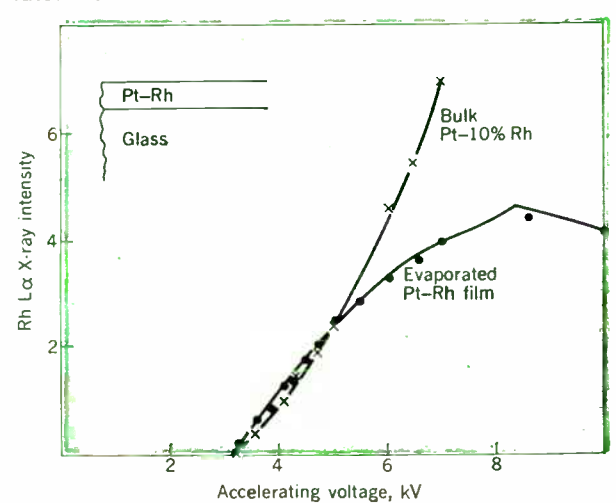
FIGURE 20. Graph of increasing electron beam voltage vs. $M\alpha$ X-ray lines for bulk Pt-10 percent Rh and evaporated Pt-Rh film.

Christ, Ramsey—Analysis tools for microminiaturized circuits

"missing" the PSG layer by going through the SiO_2. Curves such as this give two pieces of information, both of which can be calibrated with standards: (1) The slope of the curve is a function of the composition of the glass. (2) The voltage at the breakpoint V_2 is a function of the thickness of the glass.

A practical illustration of the first statement follows. A 400 Å layer of platinum was evaporated onto a silicon surface and heated to a high temperature for reaction. Was the temperature–time combination sufficient, i.e., did any unreacted platinum remain? Figure 19 shows the platinum X-ray buildup on a bulk platinum sample, and the buildup on the platinum silicon sample. Clearly, the break at V_2 giving two distinct slopes indicates a thin layer of unreacted platinum left on top of the reaction zone.

This technique is powerful enough to show changes in composition even in 1000 Å films. For example, high-temperature thin-film thermocouples are of interest, and should be calibrated, and it is desirable to use them as evaporated. In practice, large deviations from bulk were noted and the question arose as to whether these were thin-film effects or composition effects. X-ray spectrography indicated that the films were platinum–10 percent rhodium, as expected. However, the variable accelerating potential technique yielded the results shown in Fig. 20, in which the evaporated Pt-Rh film is seen to be richer in rhodium than standard at the surface (low voltage, small penetration) and poorer in rhodium at the glass substrate. This result should be expected from vapor pressure arguments, but how else could it be verified so easily?

This technique is also useful in analyzing imbedded PSG layers. In fact, it was developed for the analysis of the composition and thickness of the thin layer of PSG used to stabilize high-frequency transistors.[16] This PSG layer is under a layer of SiO_2. There are no phosphorous X rays until the electrons reach the PSG layer with the critical excitation potential. This shift is a measure of the SiO_2 overlay thickness and can be calibrated. The analysis of the PSG layer has been discussed; it gives composition and thickness data.

Conclusion

The high design and performance requirements of computer-grade circuitry and microminiaturized packaging concepts give rise to many materials problems. These can be attacked successfully only with advanced, and constantly refined, microanalytical methods. The necessary instrumentation is expensive and sophisticated and generally is utilized much less than 100 percent of the time. In general the techniques are complementary and it is seldom that one will provide a complete answer to a problem. However, we have made significant progress in the successful analysis of very small regions, although much information still eludes us.

REFERENCES

1. Bush, V., *Science Not Enough.* New York: Morrow, 1967.
2. Dhaka, V. A., 'Subnanosecond monolithic current switch and design of high-frequency transistors," presented at Internat'l Elektronic Arbeilskreis Er. (Conf.), Munich, Germany, Oct. 24–28, 1966.

3. Davidse, P. D., and Maissel, L. I., *J. Appl. Phys.,* vol. 37, p. 574, 1966.
4. Fisher, R. M., ASTM TP 155, Symp. Techniques for Electron Metallography, 1954, p. 83.
5. Cameron, D. P., and Ramsey, J. N., Private communications.
6. Joshi, M. L., and Dash, S., *IBM J. Res. Develop.,* p. 271, May 1967.
7. Lawhorne, S., and Ramsey, J. N., "Simplified X-ray examination of solid-state devices," *Solid State Technol.,* pp. 37–39, Nov. 1968.
8. Schwuttke, G. H., *J. Appl. Phys.,* vol. 36, p. 2712, 1965.
9. Schwuttke, G. H., *Proc. 1967 Annual Symp. Reliability Physics,* pp. 80–94.
10. Castaing, R., and Guinier, A., "Electron microscope," *Proc. Delft Conf.,* p. 60, 1949.
11. Castaing, R., Thesis, University of Paris, 1951.
12. Ramsey, J. N., and Weinstein, P., *The Electron Microscope.* New York: Wiley, 1966, p. 715.
13. Birks, L. S., *Electron Probe Microanalysis.* New York: Interscience, 1963.
14. Weinstein, P., and Ramsey, J. N., "564 storage scope," *Rev. Sci. Instr.,* vol. 35, p. 1724, Dec. 1964.
15. Gniewek, J. J., and Koopman, N. G., presented at Third Ann. Microprobe Conf., Chicago, Ill., 1968.
16. Young, D. R., and Seraphim, D. P., *IBM J. Res. Develop.,* vol. 8, p. 366, 1964.

J. G. Christ was born on March 22, 1914, and received the B.A. degree in chemistry in 1939 from the University of Rochester. He was with Eastman Kodak from 1937 to 1941, followed by a year as research metallurgist at Battelle Memorial Institute. In 1942 he joined the Westinghouse Electric Corporation in East Pittsburgh, Pa., as materials engineer, becoming manager of the Westinghouse Nuttal Division metallurgical section in 1946. He left Westinghouse in 1951 to become manager of the Ferrotherm Heat Treating Company in Pittsburgh, rejoining the former company in 1952 in its Bettis Atomic Power Division where he was responsible for the technical aspects of materials specifications covering submarine and commercial power reactors. He joined IBM in Poughkeepsie in 1956 as manager of the Materials Laboratories and has been involved in all aspects of materials processing, characterization, and failure analysis of computer parts. He holds patents in the areas of brazing alloys, stainless steels, and NiFe film memories.

J. N. Ramsey was born in Independence, Mo. Following his service with the Air Force during World War II, he received the B.S. degree in physics in 1949, the M.S. degree in metallurgical engineering in 1951, and the Ph.D. degree in metallurgy in 1954, all from the Rensselaer Polytechnic Institute, Troy, N.Y. He first was employed by the Air Reduction Research Laboratory, leaving that organization to join the staff of the Massachusetts Institute of Technology. This was followed by positions with the Pratt and Whitney Aircraft Laboratory and the United Aircraft Research Laboratory, and during this time he also served as 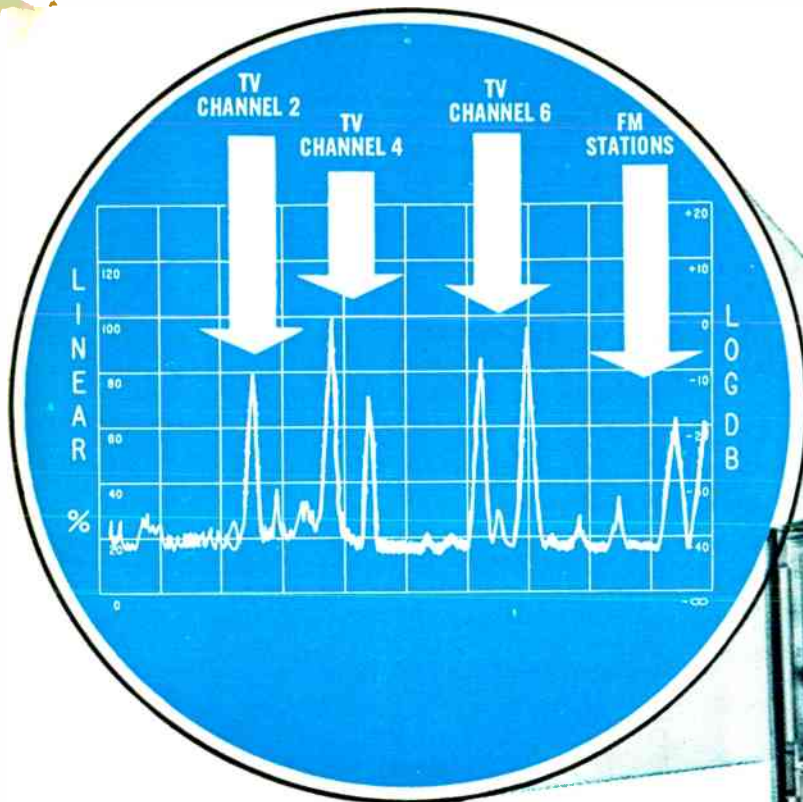adjunct assistant professor of metallurgy at Rensselaer Polytechnic Institute's Graduate Center in Hartford. Dr. Ramsey joined the International Business Machines Corporation in 1959. He has worked in the broad area of materials and the problems associated with microminiaturization, with particular emphasis on microanalysis and microdiffraction techniques.

Christ, Ramsey—Analysis tools for microminiaturized circuits

OCTAVE-BAND RF-SWEPT SPECTRUM DISPLAYS
## with Integral Preselection

Cover 14 kHz to 1 GHz

SWITCH-SELECT 15 CLEAN CRT DISPLAYS FOR FAST SIGNAL ANALYSIS WITH ANALYZER CSR-200

- **SURVEILLANCE**
- **COMMUNICATIONS**
- **RFI/EMC TESTS**
- **FIELD STRENGTH TESTS**
- **SPECTRUM ANALYSIS**
- **INTERFERENCE ANALYSIS**
- **DESIGN ANALYSIS**

50 MHz to 100 MHz, one of 15 octave displays Switchable from EMC-25 Receiver Front Panel. Display in *Spectrum* Position. Log response, Sweep rate @ 10 Sweeps/sec.
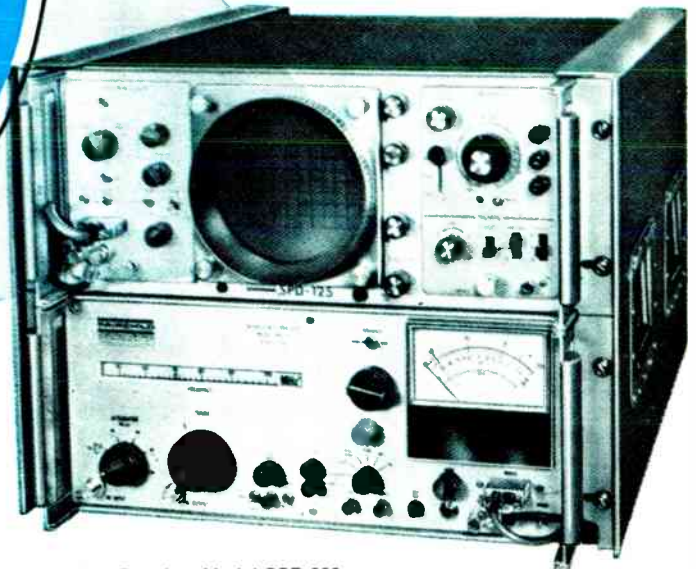
Callbrated Spectrum Analyzing Receiver Model CSR-200

The full story on your spectrum of interest can now be seen quickly, a whole octave at a time—with electronically-tracked RF amplification and preselection! The oscilloscope presentation of 14 kHz to 1 GHz, provided by the Calibrated Spectrum Analyzing Receiver* CSR-200 makes full use of the highly-sensitive, solid-state, Model EMC-25 swept receiver front-end circuitry to take the guesswork out of spectrum analysis.

With CSR-200, you switch-select your choice of 16 display formats for each of the 15 octave bands—*Spectrum,* for viewing the entire band; *Locator,* for determining frequency within the octave band; *Signature,* for close-up viewing of a specific frequency segment within the octave; and *Video,* for time-domain viewing of modulation on a chosen carrier—each in either linear or log response—and each

in either Wide or Narrow bandwidth of the receiver IF system!

All the basic EMC-25 receiver features are exploited, including RF selectivity, high sensitivity and shielding, varactor-controlled frequency scanning, dual bandwidths and wide dynamic range. And it's easy to pull the receiver out of the CSR-200 cabinet and make use of it alone, for RFI/EMC and other monitoring work—powering it from its own self-contained rechargeable internal battery.

The Display Module provides sweep voltage to scan the receiver electronically at rates of up to 10 sweeps per second.

Input to the system may be from a wide choice of available antennae, pick-up devices and other sources.

For full details or a demonstration, contact your local Fairchild/Electro-Metrics representative or the company directly.

---

*HOW THE CSR-200 DIFFERS FROM A STANDARD SPECTRUM ANALYZER

A Spectrum Analyzing Receiver incorporates integral tracked RF amplification and preselection, full receiver sensitivity, and calibrated log and linear displays of amplitude vs. frequency and time. It includes the full capability of an RFI/EMC meter, with choice of matching pick-up devices, circuitry designed for handling broadband, impulse-type signals, built-in broadband calibrator and all the special detector circuits needed for interference measurements.

FAIRCHILD
ELECTRO-METRICS
CORPORATION
A SUBSIDIARY OF FAIRCHILD CAMERA AND INSTRUMENT CORPORATION

100 CHURCH ST., AMSTERDAM, N. Y. 12010 • 518-843-2600

Circle No. 2 on Reader Card